LYOTROPIC LIQUID CRYSTAL TEMPLATED SYNTHESIS OF SINGLE-CRYSTALLINE GOLD MICROPLATES AND TRANSPARENT CONDUCTIVE REDUCED GRAPHENE OXIDE THIN FILMS

A Thesis Submitted to
the Graduate School of Engineering and Sciences of
İzmir Institute of Technology
in Partial Fulfillment of the Requirements for the Degree of

MASTER OF SCIENCE

in Chemistry

by
Betül AKKUŞ

July 2023
İZMİR

We approve the thesis of **Betül AKKUŞ**

Examining Committee Members:

Asst. Prof. Dr. Fadime MERT BALCI
Department of Chemistry, İzmir Institute of Technology

Assoc. Prof. Dr. Nermin Seda KEHR
Department of Chemistry, İzmir Institute of Technology

Asst. Prof. Dr. Muhammed ÜÇÜNCÜ
Department of Analytical Chemistry, İzmir Kâtip Çelebi University

14 July 2023

Asst. Prof. Dr. Fadime MERT BALCI
Supervisor, Department of Chemistry,
İzmir Institute of Technology

Prof. Dr. Gülşah ŞANLI MOHAMED
Head of the Department of Chemistry

Prof. Dr. Mehtap EANES
Dean of the Graduate School of
Engineering and Sciences

ACKNOWLEDGEMENTS

Foremost, I would like to express my sincere thanks to my advisor, Asst. Prof. Dr. Fadime MERT BALCI, for her guidance, support, and motivation throughout my MSc study. I will never forget her contributions and efforts throughout my academic life.

I would like to thank the thesis committee members, Assoc. Prof. Dr. Nermin Seda KEHR and Asst. Prof. Dr. Muhammed ÜÇÜNCÜ, for their valuable participation and feedback on my work.

I would like to thank Prof. Dr. Sinan BALCI who has always patiently supported and encouraged me during my graduate study.

I would also like to thank the lecturers at IZTECH Materials Research Center for their patience and help.

Most importantly, I would like to express my gratitude to my lovely family for always being with me and supporting me throughout my life. Their endless trust in me has helped me overcome many things in life. I would like to dedicate this thesis to my family for their eternal love, support, and encouragement.

ABSTRACT

LYOTROPIC LIQUID CRYSTAL TEMPLATED SYNTHESIS OF SINGLE-CRYSTALLINE GOLD MICROPLATES AND TRANSPARENT CONDUCTIVE REDUCED GRAPHENE OXIDE THIN FILMS

Surfactants organize to form various mesophases of lyotropic liquid crystal (LLC) in the presence of water. In the literature, some acids, salts, and ionic liquids have also been used to form ordered LLC mesophases. In this thesis, two dimensional (2D) single-crystalline gold (Au) nano- and microplates and reduced graphene oxide (RGO) thin films have been synthesized using LLC mesophases. Stable LLC mesophases have been formed using 10-lauryl ether ($C_{12}EO_{10}$), an oligo-type surfactant, and sulfuric acid (H_2SO_4), a strong acid. Au plates with various anisotropic structures, such as triangular, truncated triangular, hexagonal, and gear-like, have been synthesized by a photochemical method in the presence of LLC mesophase. Most importantly, Au plates up to 39 μm in width have been obtained in the confined space of the LLC medium. The thickness of the obtained Au plates varies from 50 nm to 150 nm. The size and/or morphology of Au products synthesized in LLC medium depends on the power of the light source, the irradiation time, the amount of Au precursor added, the addition of different capping agents, and various inorganic salts. Additionally, spin-coated RGO thin films have been synthesized using the LLC mesophase for use as a transparent and conductive electrode in various electrochemical devices. The LLC mesophase has improved the sheet resistance values of RGO thin films. RGO thin films with a sheet resistance of 31 kΩ/sq and an optical transmittance of 92% at 550 nm have been achieved at the high thermal annealing temperature under an inert atmosphere.

ÖZET

TEK KRİSTALLİ ALTIN MİKROPLAKALARIN VE ŞEFFAF İLETKEN İNDİRGENMİŞ GRAFEN OKSİT İNCE FİLMLERİN LİYOTROPİK SIVI KRİSTAL ŞABLONLU SENTEZİ

Yüzey aktif maddeler, su varlığında liyotropik sıvı kristalin (LSK) çeşitli mezofazlarını oluşturmak üzere organize olurlar. Literatürde, bazı asitler, tuzlar ve iyonik sıvılar da düzenli LSK mezofazları oluşturmak için kullanılmıştır. Bu tezde, LSK mezofazları kullanılarak iki boyutlu (2D) tek kristalli altın (Au) nano- ve mikroplakalar ve indirgenmiş grafen oksit (RGO) ince filmler sentezlendi. Kararlı LSK mezofazları, oligo tipi bir yüzey aktif madde olan 10-lauril eter ($C_{12}EO_{10}$) ve güçlü bir asit olan sülfürik asit (H_2SO_4) kullanılarak oluşturuldu. Üçgen, kesik üçgen, altıgen ve dişli benzeri gibi çeşitli anizotropik yapılara sahip Au plakaları, LSK mezofazının varlığında fotokimyasal bir yöntemle sentezlenmiştir. En önemlisi, genişliği 39 μm'ye kadar olan Au plakaları, LSK ortamının sınırlı alanında elde edildi. Elde edilen Au plakalarının kalınlığı 50 nm ile 150 nm arasında değişmektedir. LSK ortamında sentezlenen Au ürünlerinin boyutu ve/veya morfolojisi, ışık kaynağının gücüne, ışınlama süresine, eklenen Au öncülünün miktarına, farklı kaplama ajanlarının ve çeşitli inorganik tuzların eklenmesine bağlıdır. Ayrıca, spin kaplamalı RGO ince filmler, çeşitli elektrokimyasal cihazlarda şeffaf ve iletken bir elektrot olarak kullanılmak üzere LSK mezofazı kullanılarak sentezlendi. LSK mezofazı, RGO ince filmlerin tabaka direnç değerlerini iyileştirmiştir. 31 kΩ/sq tabaka direncine ve 550 nm'de %92 optik geçirgenliğe sahip RGO ince filmleri, inert bir atmosfer altında yüksek ısıl tavlama sıcaklığında elde edilmiştir.

TABLE OF CONTENTS

LIST OF FIGURES

Figure **Page**

Figure **Page**

Figure **Page**

Figure **Page**

Figure **Page**

LIST OF TABLES

LIST OF ABBREVIATIONS

Abbreviation	Explanation
AFM	Atomic Force Microscopy
ATR	Attenuated Total Reflectance
CMC	Critical Micelle Concentration
CPP	Critical Packing Parameter
CVD	Chemical Vapor Deposition
EO	Ethylene Oxide
FT-IR	Fourier Transform Infrared Spectroscopy
GO	Graphene Oxide
LC	Liquid Crystal
LLC	Lyotropic Liquid Crystal
POM	Polarized Optical Microscopy
RGO	Reduced Graphene Oxide
SA	Sulfuric Acid
SEM	Scanning Electron Microscopy
STEM	Scanning Transmission Electron Microscopy
TLCT	True Liquid Crystal Templating
UV-Vis	Ultraviolet-Visible
XRD	X-Ray Diffraction

CHAPTER 1

INTRODUCTION

1.1. Liquid Crystals

Liquid crystals (LCs) are mesophases between liquid and solid, known as the fourth state of matter, and consist of organic substances. The crystalline solid phase consists of a highly ordered crystal lattice and molecules cannot move freely in this highly ordered structure. Therefore, molecules in a crystalline solid phase exhibit both positional and orientational order (anisotropic). However, liquids do not have positional or orientational order (isotropic) because the intermolecular forces in liquids are weaker than in solids and the molecules move randomly in this highly disordered structure. The molecules of LCs have mobility like molecules in liquids, but they have orientational order and sometimes positional order, though not as much as solids, as shown in Figure 1.1.[1] Because of this orientational order of molecules in the LC phase, these materials are optically birefringent, meaning that they have two different indices of refraction. Therefore, different LC phases give different textures under the polarizing optical microscope.

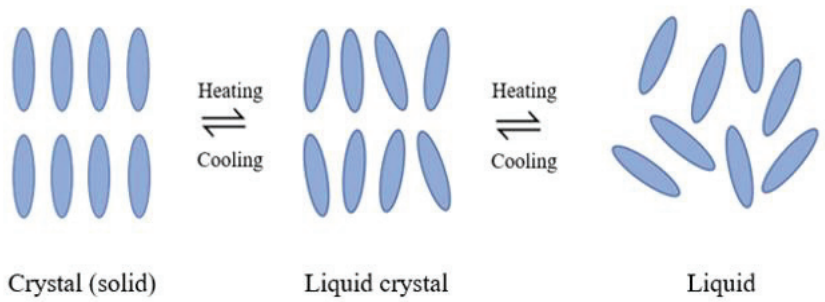

Figure 1.1. A schematic representation showing the phase transition from solid to liquid and the difference in orientational and positional order in crystal, liquid crystal, and liquid phases of matter.

Liquid crystal materials have been studied for over a century, but in 1888, the first documented example of an LC was reported by Austrian botanist Friedrich Reinitzer.[2] In

fact, he noticed that cholesteryl benzoate has two different melting points. When Reinitzer melted the white solid, he observed that a turbid liquid was formed at 145°C and a clear, transparent liquid was formed at 179°C. In 1889, Otto Lehmann also made a significant contribution to this work.[3] He investigated the phase transitions of cholesteryl benzoate with the heating stage polarizing microscope.

There are two main types of LCs: thermotropic and lyotropic. Thermotropic LCs are single-component systems and temperature changes affect the phase transition of these LCs. Calamitic (rod-like) and discotic (disc-like) organic molecules can form thermotropic mesophases.

Unlike thermotropics, in lyotropic liquid crystals (LLCs), phase behavior is affected by both temperature and solute concentration. At least two components are required to form the LLC phase: the amphiphilic molecule (surfactant) and the solvent (usually water). Amphiphilic molecules consist of a hydrophilic polar head and a hydrophobic non-polar tail. The dissolution of amphiphilic compounds in a suitable solvent leads to the formation of LLC phases.

1.1.1. Surfactants and Formation of Micelle

Surfactants are surface-active agents and they reduce the surface tension of the dissolved medium by adsorbing at surfaces and interfaces. Adding low concentrations (usually less than 1%) of a surfactant to water significantly lowers the surface tension of the solvent.[4] Surfactants can be classified as cationic, anionic, nonionic, and zwitterionic according to the type of charge(s) on their hydrophilic parts**.** If the charge on the head of an ionic surfactant is negative such as carboxyl ($RCOO^- M^+$), sulfonate ($RSO_3^- M^+$), sulfate ($ROSO_3^- M^+$), or phosphate ($ROPO_3^- M^+$), the surfactant is called anionic; If the charge is positive such as quaternary ammonium halides ($R_4N^+ X^-$), it is said to be cationic. Zwitterionic or amphoteric surfactants consist of both positive and negative hydrophilic parts attached to the same molecule, for example, glycine (NH_2CH_2COOH) or alkylsulfobetaines $RN^+(CH_3)_2CH_2CH_2SO_3^-$. However, nonionic surfactants have no charge on the hydrophilic head group such as polyoxyethylene ($R–OCH_2CH_2O–$) or R–polyol groups. Examples of these surfactants are given in Figure 1.2.

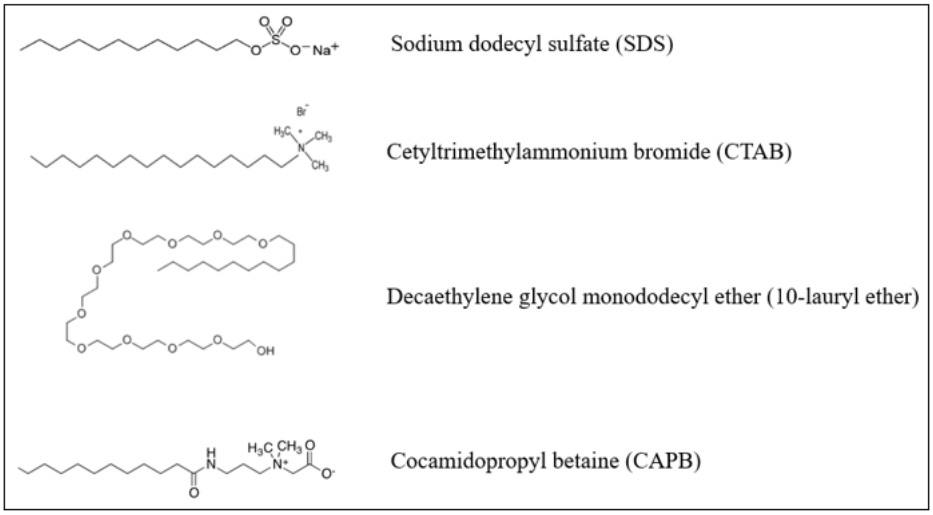

Figure 1.2. Molecular structures of anionic, cationic, nonionic, and zwitterionic surfactants from top to bottom, respectively.

The most common surfactant is sodium dodecyl sulfate (SDS), an anionic surfactant. Cetyltrimethylammonium bromide (CTAB) is a cationic, decaethylene glycol monododecyl ether (10-lauryl ether) is a nonionic, and cocamidopropyl betaine (CAPB) is a zwitterionic type surfactant. In this study, decaethylene glycol monododecyl ether ($C_{12}EO_{10}$, 10-lauryl ether) has been mainly used as an oligo(ethylene oxide)-type nonionic surfactant. It contains a hydrophobic alkane C_nH_{2n+1} tail and a hydrophilic oligo(ethylene oxide) $(–CH_2CH_2O–)_n$ head group.

The hydrophobic region of surfactants tends to avoid contact with water (solvent) due to the hydrophobic effect. Owing to the hydrophobic effect, surfactant monomers tend to aggregate in solution spontaneously and hence micelles are formed. On the other hand, the hydrophilic units of the micelles form hydrogen bonds with water molecules. In an aqueous solution, hydrophobic chains (usually alkyl chains) form the core of the micelle and hydrophilic units form a shell in contact with the water. For example, in the decaethylene glycol monododecyl ether molecule, the ethoxy groups form hydrogen bonds with water molecules and the hydrophobic alkyl tails do not interact with water molecules. In micelle formation, the driving force is the hydrophobic effect acting on the hydrocarbon chains and the repulsive force must come mainly from the head groups of the surfactant molecules.[5–7]

Micelles have different shapes, such as spherical, cylindrical, or bilayer, but thermodynamically spherical shapes are preferred.[8] Tanford introduced the standard free energy change related to aggregation to calculate micelle size and explain other micelle

properties.[5,6] Using Tanford's free energy expression, the theory of molecular packing parameters was developed by Israelachvili et al.[8] They explained that the micelle size and shape depend on the packing of the molecules. The molecular packing parameter is defined as $v / l_c a_o$, where a_o is the optimal head group area, l_c is the critical length of the hydrophobic tail, and v is the volume of the hydrophobic portion of the molecule. Three factors that define the molecular packing parameter in a spherical micelle are shown in Figure 1.3.

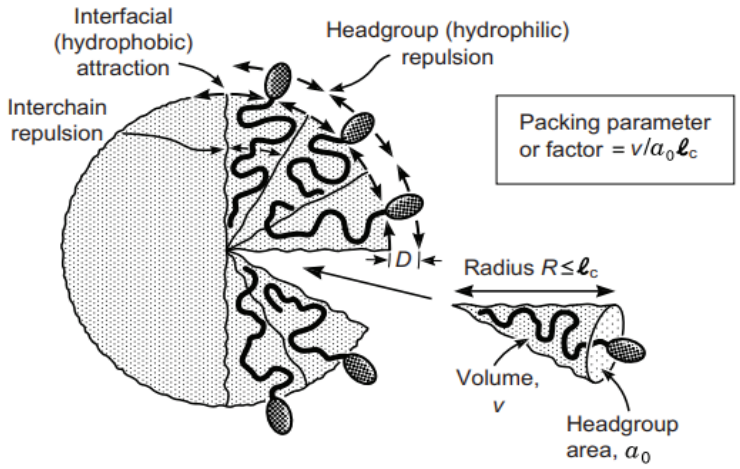

Figure 1.3. Schematic representation of the three molecular packing parameters (v, l_c, and a_o) for surfactant molecules. (Source: Israelachvili, 2011)[9]

At critical micelle concentration (CMC), surfactant monomers aggregate to form spherical micelles. Below the CMC, the surfactant molecules exist as monomers in solution and a monolayer of surfactant molecules forms at the air-water interface, in other words, micellization cannot be observed. The CMC value is commonly determined by measuring the surface tension of a solution containing different surfactant concentrations (see Figure 1.4). However, surface tension measurement is time-consuming compared to spectroscopic methods and gives reliable results at higher CMCs.[10] CMC in a given medium depends on the nature of the surfactant (size and structure of the hydrophobic group and the head group of the hydrophilic chain), the nature of counterions, the addition of electrolytes, temperature, etc.[11]

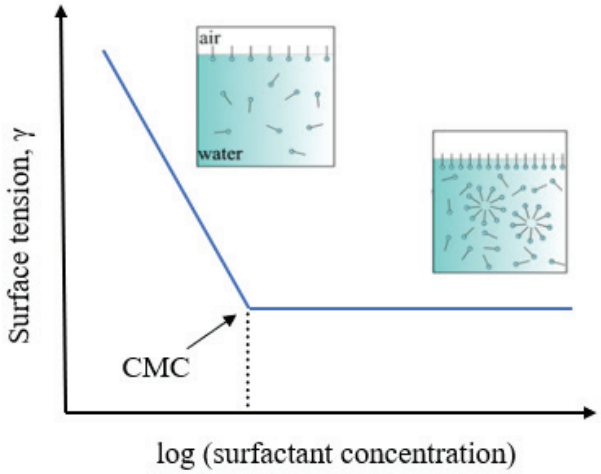

Figure 1.4. Surface tension of surfactant solution as a function of surfactant concentration on a logarithmic scale. (Source: Hamberger and Landfester, 2011)[12]

1.1.2 Lyotropic Liquid Crystalline Mesophases

Further increase of surfactant molecules in the medium above the CMC results in the formation of different lyotropic liquid crystal (LLC) phases, such as simple cubic (I_1), 2D hexagonal (H_1), lamellar (L_α), and bicontinuous cubic (V_1) phases (see Figure 1.5). There are some essential chemical characterization methods to identify these LLC phases such as polarized optical microscopy (POM), X-ray diffraction (XRD), differential scanning calorimetry (DSC), transmission electron microscopy (TEM), and nuclear magnetic resonance (NMR) spectroscopy.[13,14]

The lamellar (L_α) LLC phase contains bilayers separated by aqueous domains. While the polar head groups of surfactant molecules are in contact with the aqueous medium, the hydrophobic tails face the center of the layer. The subscript α denotes the fused chains in this mesophase.[15] This mesophase, despite its high surfactant content, is less viscous than the hexagonal LLC phase because the bilayers can easily slide over each other. It has characteristic scattering Bragg peaks in the ratio 1: 2: 3, etc., obtained from the Small Angle X-Ray Scattering (SAXS).[15,16] Lamellar LLC phases show distinct optical textures under the POM investigations and the texture is streaky or mosaic-like.[15–17]

The hexagonal LLC phase (H_1) consists of elongated (rod-shaped) or infinite cylindrical micelles organized in a two dimensional (2D) hexagonal lattice. There are two distinct types of the hexagonal phase depending on the solvent polarity: the normal

hexagonal phase (H_1), known as the "middle phase", and the reversed hexagonal phase (H_2). Hexagonal mesophases are identified by their characteristic fan-like texture under the POM.[15,17,18] The small angle X-ray spectrum shows Bragg peaks in the ratio 1: √3: √4, etc.[15,19]

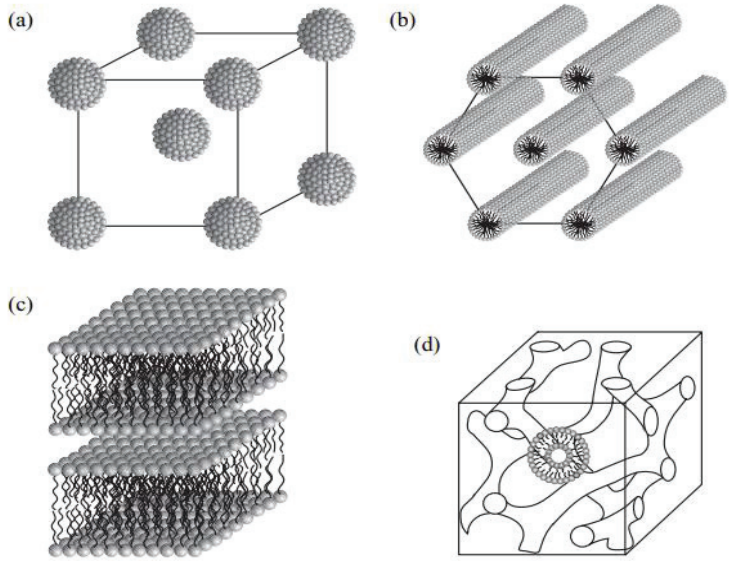

Figure 1.5. Schematic illustration of (a) simple cubic (I_1), (b) hexagonal (H_1), (c) lamellar (L_α), and (d) bicontinuous cubic (V_1) mesophases. (Source: Hamley, 2007)[20]

Unlike lamellar and hexagonal LLC phases, cubic LLC phases are optically isotropic and do not show any texture under the POM measurements. Normal micellar cubic (I_1) and reversed micellar cubic (I_2) phases have globular micelles formed in a cubic arrangement. These mesophases are less viscous than others due to their globular structure. Spherical micelles are mostly arranged in body-centered cubic structure (bcc, Im3m) and others include face-centered cubic (fcc, Fm3m) or clathrate (type 1, Pm3n and type 2, Fd3m) packings.[15] Furthermore, bicontinuous cubic LLC phases (V_1 or V_2 according to normal or reverse structure) are more viscous than the other phases.

For a given concentration, the LC phase behavior of amphiphilic molecules depends on the structure of surfactant, temperature, ionic strength of the medium, and the addition of solutes.[11] As the surfactant concentration increases in a binary amphiphile – solvent system, a phase transition from L_1 (micellar solution) to H_1 to L_α is expected; between these phases, intermediate I_1 (L_1 and H_1) and V_1 (H_1 and L_α) phases can be observed.[20] Reverse structures such as V_2, H_2, and I_2 can be seen in the system as the surfactant concentration increases further (low solvent content).[20]

As mentioned before, the critical packing parameter (CPP), defined as $v / l_c a_o$, is a useful equation for understanding the morphology of aggregates in a surfactant–water system. When the CPP is about 1, the lamellar LLC phase is formed. Normal micelles are formed when <1 and reverse micelles are formed when >1.[21] Table 1.1 shows some structures formed according to the value of the packing parameter.

Table 1.1. Expected self-assembled aggregates in relation to critical packing parameters (CPP). (Source: Myers, 2006)[11]

Critical Packing Parameter	General Surfactant Type	Expected Aggregate Structure
<0.33	Simple surfactants with single chains and relatively large head groups	Spherical or ellipsoidal micelles
0.33–0.5	Simple surfactants with relatively small head groups, or ionic surfactants in the presence of large amounts of electrolyte	Relatively large cylindrical or rod-shaped micelles
0.5–1.0	Double-chain surfactants with large head groups and flexible chains	Vesicles and flexible bilayer structures
1.0	Double-chain surfactants with small head groups or rigid, immobile chains	Planar extended bilayer structures
>1.0	Double-chain surfactants with small head groups, very large, bulky hydrophobic groups	Reversed or inverted micelles

1.1.3. C_nEO_m + H_2O Binary Systems

Poly(ethylene oxide) monoalkyl ether (C_nEO_m) type molecules are nonionic surfactants. Their molecular structures consist of a hydrophobic tail and an ethylene oxide (EO) hydrophilic head group. It should be noted here that n represents the length of the carbons and m represents the length of the EO units in the surfactant molecule. The advantage of using such nonionic surfactants in research is that they are commercially available with different hydrophobic chains and hydrophilic head group units. In addition to the nonionic surfactant and water binary systems[22–24], the phase behavior of nonionic surfactants has been studied with different solvents, such as organic solvents[25], ionic liquids[26], supercritical CO_2[27], salts[28,29], and acids[18,30].

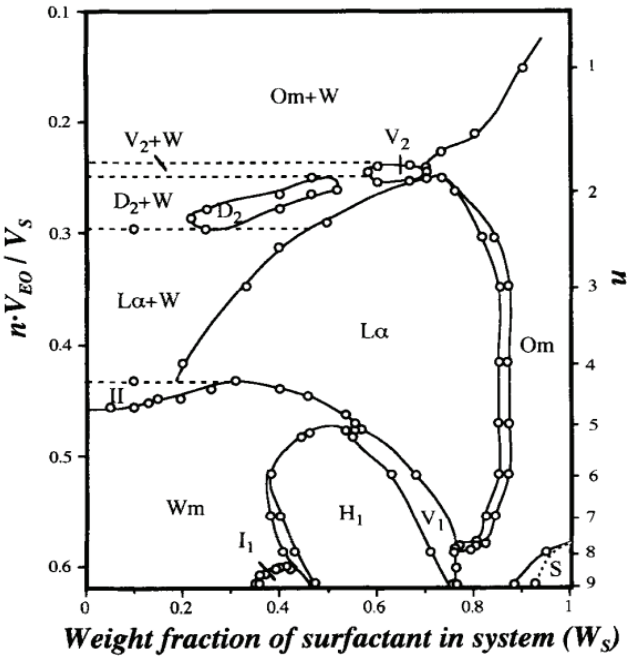

Figure 1.6. Phase diagram of $C_{12}EO_m$ – H_2O with the variation of EO head group length at 25 °C. (Source: Huang et al., 1998)[23]

Tiddy et al. studied the phase diagrams of various C_nEO_m nonionic type surfactants in water with an optical microscope.[22] They reported that cubic and hexagonal LLC phases are observed in surfactant molecules for long EO chains (m>8) and at low temperatures. On the other hand, lamellar and reverse LLC phases tend to form in surfactant molecules with short EO chains (m<5) and at higher temperatures. The phase diagram of the $C_{12}EO_9$ – H_2O was investigated at 25 °C.[23] As seen in Figure 1.6, the phase transition of $I_1 \rightarrow H_1 \rightarrow V_1$ is observed with increasing surfactant concentration. If the EO chain length (m) decreases, the cross-sectional area of the surfactant decreases and so does the curvature of the surfactant layer.[23] The same behavior is also observed in long hydrophilic chain poly(oxyethylene) oleyl ether (POlE) systems (m is greater than 7).[24] Furthermore, the same sequences of phase transition are observed as the temperature increases because decreased dehydration in the head groups leads to a decrease in the cross-sectional area of the surfactant.[31]

The presence of salt affects the phase behavior of the C_nEO_m – H_2O binary system. Hofmeister[32] anion and cation series can be arranged as in Figure 1.7. The ions on the left are called kosmotropes, meaning they strengthen the hydrogen bond in water. On the other hand, the ions on the right side are called chaotropes, which means breaking the

structure of water. The cations on the left are weakly hydrated and called as chaotropes, while the divalent cations on the right called as kosmotropes.[33]

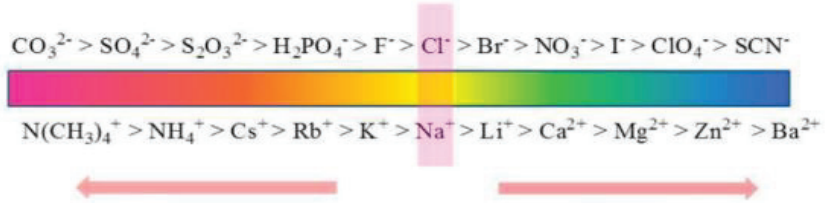

Figure 1.7. Hofmeister series (HS).
(Source: Kang et al., 2020)[33]

Inoue and coworkers investigated the effect of Cl^-, I^-, and ClO^{-4} anions on the aqueous phase of $C_{12}EO_7$. They found that the field of the lamellar phase shrinks according to the NaCl > none > NaI > $NaClO_4$. On the other hand, the field of the hexagonal phase expands according to the NaCl < none < NaI ≈ $NaClO_4$. As shown in the Hofmeister series, ClO^{-4} has a stronger chaotropic effect than I^-, so the EO chain hydration is further enhanced with $NaClO_4$. The optimal head group area (a_o) increases with the hydration of the EO chain. This leads to the formation of the hexagonal phase and is unfavorable for the lamellar phase.[34]

Zheng and coworkers investigated the effect of cations on the aqueous phase of $C_{12}EO_7$. The increase of the lamellar phase region was observed in the order of CsCl < NaCl < LiCl. This is due to the dehydration of the EO chain as a result of the strong hydration ability of Li^+ ions. The areas of the hexagonal phase and bicontinuous cubic phase decrease in the order of LiCl > CsCl ≥ NaCl instead of CsCl > NaCl > LiCl. Other than the EO chain dehydration, some other factor(s) also determine the salt effect on the aqueous phase behavior of the $C_{12}EO_7$ mixture.[35]

Other ingredients can be used primarily as a solvent instead of water to form the LLC mesophases with the surfactant. Unlike the water-surfactant system, certain salts or acids form LLC mesophases with nonionic surfactants and these mesophases are stable under atmospheric conditions. In LLC mesophase formation, transition metal salt complexes such as $[Co(H_2O)_6](NO_3)_2$, $[Ni(H_2O)_6](NO_3)_2$, $[Zn(H_2O)_6](NO_3)_2$, and $[Cd(H_2O)_4](NO_3)_2$ can act as a secondary component and form stable mesophases with the nonionic oligo(ethylene oxide)-type surfactants ($C_{12}EO_{10}$) in the presence or absence of a small amount of water.[29] Coordinated water molecules in transition metal complexes and EO chains of nonionic surfactant form hydrogen bonds, which play a significant role

in LLC mesophase formation. The phase diagram of the $[Zn(H_2O)_6](NO_3)_2$ – $C_{12}EO_{10}$ was also investigated.[28] In this LLC system, salt materials are in the molten state in hydrophilic regions and they act as a solvent to form LLC mesophases. Like the phase diagram of a particular water – surfactant system, the phase diagram of this system has V_1, H_1, I, and L_1 phases with increasing solvent of the medium.[28] The salt content in the medium can be increased by adding a charged surfactant such as CTAB or SDS.[36] Furthermore, non-transition metal salts such as $LiNO_3$, LiCl, and $LiClO_4$ can form LLC mesophases with $C_{12}EO_{10}$ in small amounts of water.[37] These alkali metal – salt LLC mesophases can serve as gel electrolytes for electrochemical applications due to their high ionic conductivity.[37] Apart from salts, sulfuric acid (H_2SO_4)[18] or phosphoric acid (H_3PO_4)[30] can be used as a solvent for the self-assembly of nonionic surfactant ($C_{12}EO_{10}$) into LLC mesophases. These proton-conducting mesophases are significant for porous nanomaterial synthesis or renewable energy devices. LLC mesophases of H_2SO_4 – $C_{12}EO_{10}$ will be described in the next section due to the scope of this thesis.

1.1.4. H_2SO_4 – $C_{12}EO_{10}$ Lyotropic Liquid Crystalline Mesophases

In 2015, Olutaş and coworkers published a paper on a novel acidic LLC mesophase consisting of a strong acid (sulfuric acid, SA) as a solvent for the self-assembly of nonionic surfactant (10-lauryl ether, $C_{12}EO_{10}$) into different LLC mesophases in a small amount of water.[18] They used these acidic mesophases as a medium to synthesize photoluminescent carbon quantum dots and mesostructured silica films and monoliths.[18] These SA/$C_{12}EO_{10}$ LLC mesophases were also studied in the electrochemical activity of lead acid batteries (LABs).[38]

If the SA/$C_{12}EO_{10}$ mole ratio increases, V_1, H_1, and I_1 mesophases are obtained. The homogenous mixture is prepared under ambient conditions with different mole ratios of SA/$C_{12}EO_{10}$ and excess solvents such as water or alcohol. Excess water or alcohol in the composition is then equilibrated with the atmosphere to form stable LLC mesophases. Secondly, gels can be formed by mixing these components (SA and $C_{12}EO_{10}$) in an appropriate mole ratio and exposing them to the atmosphere to absorb the required water. Additionally, it can be prepared by adding water to the composition (2.3-4.3 H_2O/SA).[18]

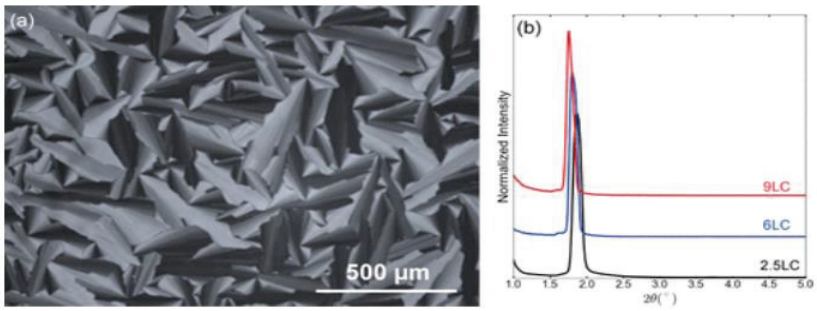

Figure 1.8. POM images of the fan-like texture of the SA/$C_{12}EO_{10}$ hexagonal mesophase (a) and small angle XRD diffraction of the LLC mesophases (b). (Source: Uzundal et al., 2017)[38]

The acidic LLC system is stable in the range of 1-11 SA/$C_{12}EO_{10}$ mole ratio. If the SA/$C_{12}EO_{10}$ mole ratio is between 2 and 3, the LLC mesophase is a 2D hexagonal. A micellar cubic structure is formed until the SA/$C_{12}EO_{10}$ mole ratio is 11. Moreover, the lowest SA/$C_{12}EO_{10}$ mole ratio of 1 corresponds to a bicontinuous cubic phase.[18]

The 2D hexagonal LLC mesophase shows a focal conical fan texture, as seen in Figure 1.8a. The highest conductivity of this sulfuric acid – nonionic system was measured as 19 mS/cm at the stable 11 SA/$C_{12}EO_{10}$ mole ratio.[18] The SA/$C_{12}EO_{10}$ mesophase with a mole ratio of 2.5 diffracts at small angles at around 2˚, 2θ. However, the XRD peak shifts to slightly lower angles with increasing acidic component in the LLC system (see Figure 1.8b).[38]

1.2. Synthesis of Nanomaterials Using Lyotropic Liquid Crystals

Kresge and co-workers described the liquid crystal templating mechanism in 1992.[39,40] They discovered the synthesis of ordered mesoporous silica materials with ionic surfactants as template molecules. With their findings, a breakthrough was made in the synthesis of mesoporous material using the soft template method. In the liquid crystal templating method, diluted surfactant solutions are used and an actual LLC phase is not included in the synthesis. In 1995, Attard et al. reported the true liquid crystal templating (TLCT) method (see Figure 1.9).[41] To produce mesoporous silica with a pore diameter of about 3 nm, they used LLC phase compositions of nonionic surfactants as a template and tetramethyl orthosilicate (TMOS) as a silica precursor in mildly acidic conditions. In the TLCT method, the hydrolysis and condensation of the silica precursor occur at suitable

temperature parameters and then the organic matter is removed by calcination, leaving ordered mesoporous structures. Since hydrolysis and condensation processes are faster in transition metal oxides than in silica materials, the rates of these processes are essential in controlling the formation of non-siliceous mesoporous structures.[42]

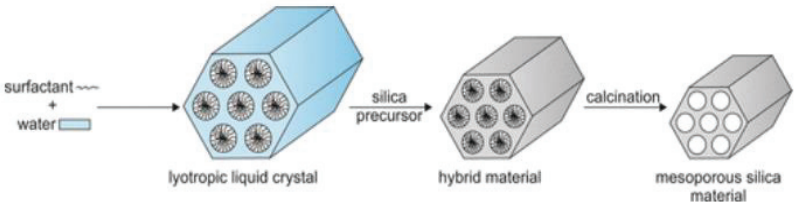

Figure 1.9. Schematic illustration of the TLCT method.
(Source: Bruckner et al., 2021)[43]

Non-siliceous mesoporous and/or mesostructured materials such as metals[44] and alloys[45,46] are synthesized using LLC mesophases. Attard et al. demonstrated, for the first time, the formation of nanostructured mesoporous platinum from the nonionic LLC mesophase.[44] This process was performed by reducing the platinum source dissolved in the hydrophilic areas of the hexagonal LLC phase. Later, Attard et al. produced metallic mesoporous platinum films by electrodeposition method from the aqueous hexagonal phase of LLC for use in electrochemical and sensor applications.[47] Various electrodeposited films produced from the LLC templating technique have also been reported, such as rhodium[48], nickel oxide[49], selenium[50], and polymer[51], as electrode materials. In this method, the surfactant is generally removed by washing the films with water after deposition, resulting in a hexagonal arrangement of uniform pores.

0-D, 1-D, and 2-D nanostructures have been synthesized using LLCs. These nanostructures are promising for electronics, optics, and sensor applications.[52–55] Different LLC mesophases can control the size and shape of inorganic materials.[56] Metal nanoparticles such as Ag[57,58], Pd[59], and Bi[60] and semiconducting nanoparticles such as PbS[60], ZnO[61], ZnS[62], and CuS[63] were synthesized using different LLC phases. Nanowires[64,65], nanorods[66], and nanotubes[67] were synthesized in the medium of LLCs. More importantly, 2-D structures of single-crystalline Au nano- and microplates[68,69] and Pt nanosheets[70,71] were obtained from LLCs.

1.3. 2D Single-Crystalline Gold (Au) Nano- and Microplates

The synthesis of 2D single-crystalline gold (Au) nano- and microplates has received great attention due to its applications in electronics, catalysis, optics, plasmonics, and biomedicine.[54,55,72–75] Single-crystalline Au plates of different shapes, such as triangular, hexagonal, and truncated triangular, can be formed by reducing Au^{+3} to Au^{0} using various approaches (see Figure 1.10). In general, plate-like Au materials have been prepared with spherical nanoparticles as a by-product at the end of the reaction.

2D single-crystalline Au nano- and microplate synthesis can be achieved by templates, surfactants, or polymers that act as capping agents, stabilizers, or reducing agents to control the morphology (shape) and size (edge length and thickness) of the plates. In the reaction mechanism, preferential adsorption of capping agents or surfactants takes place on the specific {111} facets of gold nuclei, resulting in crystal growth along the other direction to form distinct Au nanostructures.

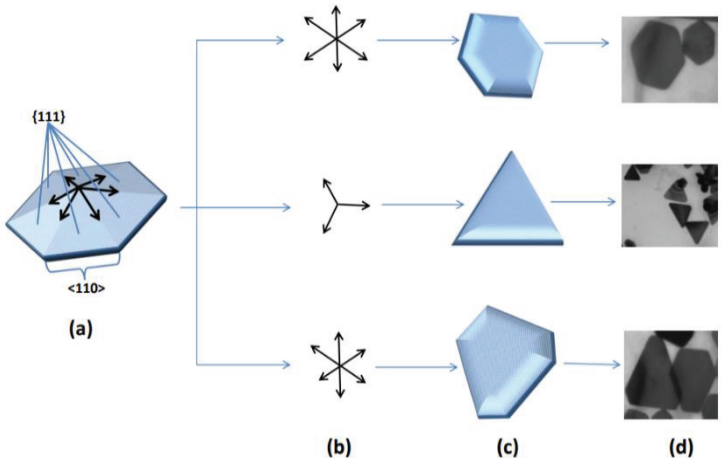

Figure 1.10. Suggested growth mechanism for Au nanoplates. (a) {111} basal plane and <110> side facet corresponding to the crystallographic facets, (b) the formation of different plate-like shapes along the <110> directions, (c) shapes of particles to be formed, and (d) representative TEM images of the resulting nanoplates. (Source: Kaur and Chudasama, 2014)[76]

Au plates with a size of several microns have been obtained using different methods. A microwave-polyol method was applied to prepare 30–90 nm diameter Au nanoplates.[77] Hexagonal-shaped and micrometer-sized Au nanoplates were synthesized by reduction of chloroauric acid ($HAuCl_4$) solution with ortho-phenylenediamine.[78] A

polyamine method was introduced for the highly efficient synthesis of several 10 μm-sized Au nanoplates.[79] In situ generation of polygonal Au nanoplates in thin poly(vinyl alcohol) (PVA) film by thermal treatment was reported.[80] The preferential orientation of Au plates was established with PVA film, a reducing agent, and a stabilizer. [80] Anisotropic Au nanostructures with various shapes were synthesized by reduction of $HAuCl_4$ in the aqueous medium of poly(vinyl pyrrolidone) (PVP), which acts as a reducing agent due to the hydroxyl (– OH) terminal groups in its structure.[81] In this method, the reaction mixture was heated to 100°C without any other reducing agents. Different Au nanostructures, such as nanotadpols, nanokits, and microplates, were obtained by varying the concentration of the aqueous $HAuCl_4$ solution in the reaction medium.[81] Using PVP, star-shaped Au nanoplates were also prepared by reduction of $HAuCl_4$ with L-ascorbic acid at RT.[82] In fact, the morphology of the Au nanoplates depends on both the amount of PVP and the reducing agent and pH of the solution.[82] Size- and shape-controlled Au nanoplates with high yield and purity were synthesized using reduced amounts of sodium citrate as a reducing agent in the presence of PVP.[83] Here, the size and shape of the Au nanoplates were controlled in a narrow size distribution by changing the amount of reducing agent and surfactant.[83]

Another synthesis procedure for Au nanoplates was performed in just 5−40 min using the thermal reduction method in the presence of cetyltrimethylammonium bromide (CTAB), a cationic surfactant.[84] There are other studies in the literature to prepare Au nanoplates based on the use of CTAB as a surfactant with reducing agents.[75,85] In the liquid-thermal method, various Au nanoparticle morphologies were controlled by a polyol method using preheated ethylene glycol, which acts as both a solvent and a reducing agent, in the presence of PVP.[86] Another polymer poly(diallyldimethylammonium chloride) (PDDA) was also used to prepare large-scale Au nanoplates with a size of several micrometers by thermal method.[87] Au nanoplates with various shapes were obtained using ionic liquid (C_{16}mimBr) that act as a shape control template through the reduction of $HAuCl_4$ with formaldehyde gas at the air-water interface.[88] Moreover, 2D single-crystalline Au nanoplate synthesis can be performed using environmentally friendly reducing and capping agents such as serum albumin protein[89], tannic acid (TA)[90], Shewanella algae cell extract[91], yeast extract[92], amyloid fibrils[93], etc.

In the seed-mediated growth method, Au nanoplates with tunable thickness and edge length in nanometer size can be achieved.[94,95] Other methods such as electrochemical, photocatalytic, photochemical reduction, and photoreduction have also

been applied to synthesize Au nanoplates.[96–100] Top-down techniques such as lithographic methods can rarely be used with a combination of bottom-up techniques to obtain single-crystalline Au nanoplates.[101]

In 2004, Wang and coworkers reported a new method involving the preparation of 2D single-crystalline Au nano- and microplates in an LLC medium with the addition of small amounts of the capping agent.[68] Triangular or hexagonal Au nano- and microplates with edge lengths longer than 10 μm were achieved by reduction of $HAuCl_4$ in the hexagonal LLC phase of the block copolymers (P123, $EO_{20}PO_{70}EO_{20}$).[68] In another of their work, the effect of capping agents was investigated to obtain controllable morphology and size of Au nano- and microplates in LLC medium.[69] Variation in product morphology tends to occur in the presence of tetrabutylammonium bromide (TBAB) rather than cetyltrimethylammonium bromide (CTAB) due to the shorter, less hydrophobic alkyl chains in its structure.[69]

There are two possible steps for the growth of Au crystals, see Figure 1.11.[69,102] The first step is nucleation, where the EO unit of the nonionic surfactant reduces the Au^{III} ions to Au atoms and/or clusters in the hydrophilic LLC domain. These formed Au atoms and/or clusters are nascent crystal nuclei in the reaction. The second step is the anisotropic growth of these Au nuclei into Au nano- and microplates in the LLC domain.[69,102]

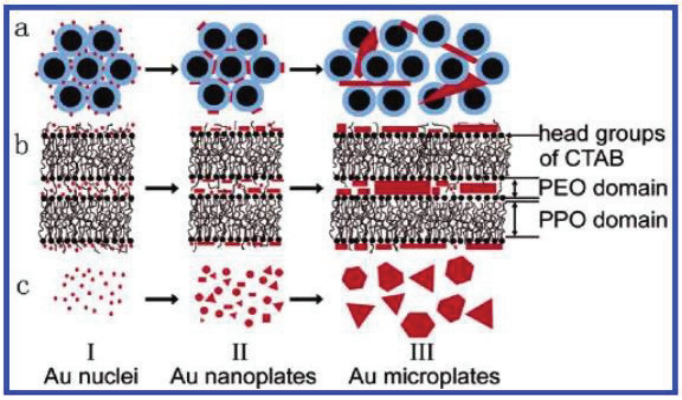

Figure 1.11. Growth mechanism of Au nano- and microplates.
(Source: Wang et al., 2005)[69]

The growth of Au plates is achieved by selective adsorption of the head group of the CTAB molecule on the (111) facet of the Au seed. Then, Au atoms are deposited in another direction of the Au surface. If the optimum concentration of the capping agent is exceeded, various morphologies, such as nanoplates, aggregates, or monodisperse

nanoparticles, are formed.[69] Moreover, a reduction in product size is obtained at the end of the reaction. The same effect has also been observed in the case of decreasing $HAuCl_4$ concentration.[69]

There are also studies based on the preparation of single-crystalline planar Au nanogears[103] and concave Au nanoplates[104] from the hexagonal LLC medium. Besides the hexagonal LLC phase, Au nanoplate synthesis was carried out in the lamellar LLC phase. Large-scale Au nanoplate synthesis was prepared from a nonionic lamellar LLC consisting of $C_{12}EO_4$ (tetraethylene glycol monododecyl ether) and $HAuCl_4$ solution.[102] According to their results, the Au nanoplate size decreased from 1 μm to several hundred nanometers with the increase of repeating PVP units. Therefore, adding a capping agent to the reaction can cause an increase in the reduction rate during plate formation.[102] Ionic liquids were used as additives to synthesize large-scale Au nanoplates and nanobelts with sizes longer than 20 μm from the hexagonal or lamellar LLC phases of P123.[105] Furthermore, Au nanoplates were formed in LLCs consisting of the zwitterionic surfactant C_{14}DMAO (tetradecyldimethylamineoxide) – H_2O binary system using CTAB and ionic liquid additives.[106]

Single-crystalline Au plates with various morphologies can be synthesized by photochemical reduction approaches with or without the LLC phase. Ding and colleagues synthesized micrometer-sized and thickness-tuned Au nanosheets through photochemical reduction from the lamellar LLC system.[107] It was noted that diffuse sunlight (natural sunlight) is the optimum condition for the growth of Au nanosheets rather than direct sunlight and UV light.[107] A starch-mediated photochemical reduction method was proposed for the tip-enhanced Raman scattering application.[98] Here, the reaction solution was exposed to sunlight for 5 days to obtain micrometer-sized Au nanoplates. In another study, with a strategy of sunlight irradiation, Varshney and coworkers synthesized concave Au nanoplates in the presence of PDDA acting as a capping agent.[108] After the reaction solution was exposed to sunlight for 6 hours, concave Au nanoplates with an edge length of about 15 μm and a center thickness of about 10 nm were obtained.[108] UV irradiation method was used to produce novel porous structures of single-crystal Au nanonetworks and nanoplates.[109] This irradiation process was carried out in aqueous $HAuCl_4$ and citric acid solution for 48 minutes without any surfactant. The citric acid concentration is an important factor in controlling the structures of porous Au nanonetworks and nanoplates.[109] UV irradiation time also has a significant effect on the

morphology of the final product.[110] A glow lamp (tungsten filament incandescent lamp, 200 W) was applied to synthesize micrometer-sized Au nanosheets with an average width of nearly 8 μm from $HAuCl_4$ and block copolymer mixtures.[97]

The effects of inorganic species such as NaCl, NaI, and NaBr on the anisotropic crystal growth of Au plate structures were investigated. NaCl promotes Au nanoplate growth perpendicular to the <111> direction, which is essential for flat anisotropic structure formation.[111] With the addition of chloride ions, oxidative etching and dissolution of less stable crystal nuclei (twinned seeds) takes place and more single-crystal seeds are converted into large particles compared to twinned crystals. When other chloride salts such as LiCl and KCl were investigated, the results were almost identical to NaCl. However, the addition of NaBr and NaI causes the formation of irregular shapes of Au nanoparticles.[111]

1.4. Reduced Graphene Oxide Thin Films

Graphene is a promising material for energy storage[112], optoelectronic[113], and biomedicine applications[114] because of its distinctive electronic, mechanical, and thermal properties. Graphene is a two-dimensional (2D) material and consists of sp^2 hybridized carbon (C) atoms organized in a honeycomb structure. In 2004, Novoselov and coworkers discovered graphene by continually peeling graphite with a scotch tape (mechanical exfoliation method).[115]

Various approaches are used to obtain graphene: top-down methods such as exfoliation and chemical oxidation-reduction; and bottom-up methods such as epitaxial growth and chemical vapor deposition (CVD).[116] Top-down approaches allow the synthesis of chemically derived graphene from the graphite raw material to be low-cost and highly efficient (see Figure 1.12). However, structural defects occur on the reduced graphene oxide (RGO) sheets during the chemical oxidation-reduction and these defects affect the efficiency of the material in applications.[117]

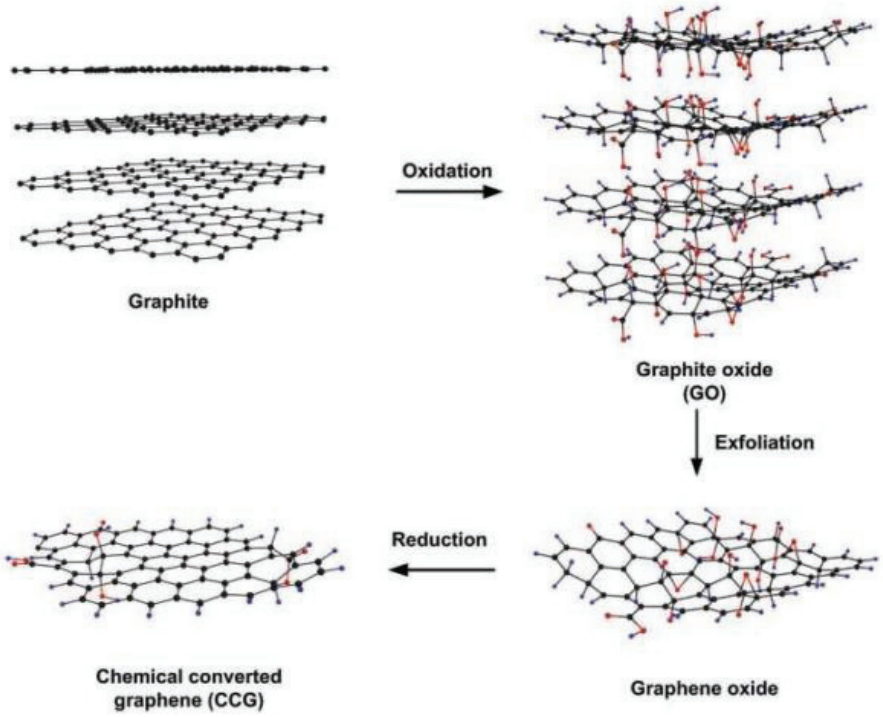

Figure 1.12. Synthesis of chemically derived graphene.
(Source: Bai et al., 2011)[118]

Graphene oxide (GO) has a hydrophilic 2D structure containing sp^2 and sp^3 hybridized carbon atoms with oxygen-containing functional groups such as hydroxyl, epoxide, carbonyl, and carboxyl groups. Considering the commonly accepted Lerf-Klinowski structural model, carboxylic acid groups are found at the edges of GO platelets, while basal planes are composed of epoxy and hydroxyl groups.[119] The oxidation of graphite was introduced by Brodie in 1859.[120] Graphite was oxidized with potassium chlorate ($KClO_3$) and fuming nitric acid (HNO_3) in the Brodie method. Staudenmaier improved this oxidation method by adding a mixture of fuming HNO_3 and sulfuric acid (H_2SO_4) and then adding small portions of $KClO_3$ throughout the reaction.[121] However, these methods require the oxidation step to be completed for up to a week and dangerous gases are released during the reaction. Hummers and Offeman then demonstrated an alternative oxidation method using potassium permanganate ($KMnO_4$) and sodium nitrate ($NaNO_3$) as oxidizing agents in the presence of concentrated H_2SO_4 (Hummers method).[122]

Studies based on the improved Hummers method showing GO synthesis without $NaNO_3$ have also been carried out.[123–128] In the Hummers method, the reaction can take several hours to complete thanks to the strong oxidant $KMnO_4$. However, toxic gas(es)

NO_2 and N_2O_4 are still formed due to the use of $NaNO_3$. In 2010, Tour and coworkers demonstrated an improved method for the synthesis of GO.[126] Compared to other methods, the Tour method does not emit toxic gases during the reaction. A concentrated mixture of H_2SO_4/H_3PO_4 is added to the graphite flakes in a ratio of 9:1. An increased amount of $KMnO_4$ is then added slowly to the reaction instead of $NaNO_3$. Finally, GO synthesis is achieved with a more oxidized form of hydrophilic carbon compared to the Hummers method. Moreover, Tour's method allows GO to have a more organized framework structure than Hummers' method because the resulting GO consists of a more intact basal plane.[126]

Several modifications have been achieved to the Tour's method to increase GO yield, reduce reaction time and temperature, and prevent explosion risk. For example, Ranjan et al. proposed an inexpensive, non-explosive process for synthesizing GO.[129] In addition to changing reaction temperature and time, they performed a pre-cooling protocol (PCP) for the reaction mixtures individually to avoid the risk of explosion during synthesis. Compared to Tour's method, expensive filtration membranes are not required because GO synthesis is achieved without metallic residue.[129] Benzait et al. reported a pretreatment step using piranha solution to improve GO synthesis.[130] The GO synthesis was achieved with a high degree of oxidation, larger plates, and fewer defects in its structure.[130] Panwar et al. tried a new route by using a mixture of H_2SO_4–HNO_3–H_3PO_4 as an intercalating agent.[131] As a result, relatively higher efficiency GO synthesis was achieved in a short time.[131]

Tour and Dimiev proposed the formation mechanism of GO in three different independent stages. In the first step, graphite raw material is turned into a sulfuric acid-graphite intercalation product (H_2SO_4-GIC). In the second step, the H_2SO_4-GIC compound becomes pristine graphite oxide (PGO) with the addition of the oxidizing agent ($KMnO_4$). Here, the oxidizing agent diffuses into the graphite layers (rate-determining step). In the last step, exfoliation of PGO into single layer graphene oxide (GO) takes place after adding water. This process is achieved by overcoming the electrostatic attraction in the intercalation compound.[132]

Kang et al. proposed two oxidation stages in the GO formation mechanism. The conventional oxidation step involves the oxidation of graphite by the dimanganese heptoxide (Mn_2O_7) and permanganyl cation (MnO_3^+), formed in the reaction of $KMnO_4$ and concentrated H_2SO_4. The second oxidation occurs in the acidic solution by MnO_4^- after adding water and before adding the hydrogen peroxide (H_2O_2). The second step was

found to affect the chemical properties of GO, such as size, defects on sheets, and functional groups in its structure.[133]

Graphene oxide (GO) can be converted to reduced graphene oxide (RGO) by removing oxygen functional groups. Since GO has oxygen functional groups, it is an insulator, but RGO is an electrically conductive material. The reduction of GO is accomplished by different methods, such as chemical, thermal, and electrochemical reduction processes. Hydrazine monohydrate ($N_2H_4 \cdot H_2O$) has mostly been used as a powerful reducing agent for RGO production, but it is a hazardous chemical. L-Ascorbic acid, known as vitamin C, is an environmentally friendly reducing agent that has proven to be an outstanding alternative to hydrazine in RGO synthesis.[134] Other reducing agents are used for the reduction process of GO such as sodium borohydride ($NaBH_4$), aluminum and zinc catalysts, plant extracts, polysaccharides, natural proteins, microorganisms, etc.[134,135] Thermal reduction approaches have been carried out by high-temperature annealing, microwave irradiation, and photoreduction methods.[136] Effective thermal heating enables RGO to achieve the high degree of graphitization and low oxygen concentration required for energy storage devices.[137] RGO has also been prepared by the electrochemical reduction method in two different approaches: coating-reducing and electrochemical deposition.[138]

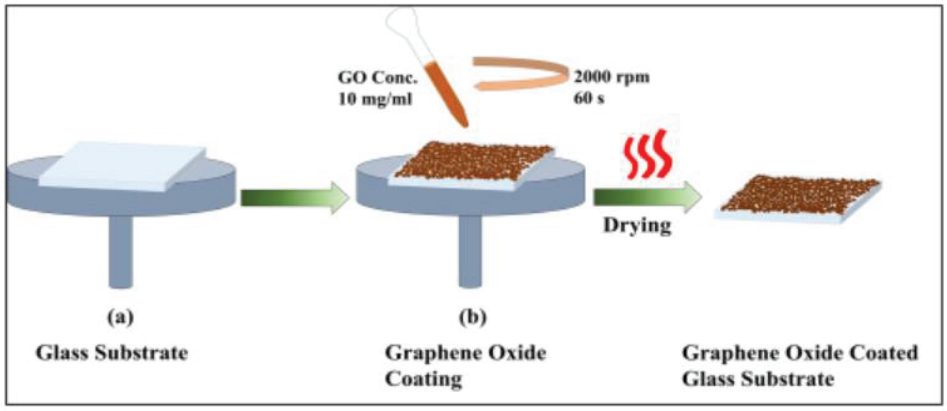

Figure 1.13. Schematic illustration of RGO thin film preparation by spin-coating. (Source: Tas et al., 2019)[139]

Electrically conductive RGO materials have been used as electrodes in various applications, such as optoelectronic devices, sensor applications, thin-film transistors, field emitters, photovoltaics, supercapacitors, batteries, etc.[140,141] RGO thin films have been deposited into the rigid substrate using different techniques, such as drop-casting[142],

spin-coating[139,143], spray pyrolysis[144], dip-coating[145], or vacuum filtration[146]. The spin-coating usually provides highly continuous uniform film deposition without GO aggregation (see Figure 1.13). Different reducing agents have also been used to remove the oxygen functional groups in GO during RGO film production.[147] However, after chemical reduction, the thin films are washed with alcohol and distilled water to remove the reducing agent residues.[139] The colloidal suspension of GO has been deposited on hydrophilic surfaces such as glass, silicon, quartz, or poly-(ethylene terephthalate) (PET) substrates.[139,148–150] Before spin-coating, these substrates are treated with piranha solution or (aminopropyl)triethoxysilane (APTES) to make the surface hydrophilic and increase the adsorption of the GO layers on the surface. Becerril et al. reported the effect of GO concentration on GO film thickness.[148] GO suspensions with low concentration (<2 mg mL^{-1}) resulted in a film thickness of about 3 nm, and concentrations in the range of 4–8 mg mL^{-1} resulted in a thickness between 6 and 15 nm. GO solutions with high concentrations between 12 and 15 mg mL^{-1} were found to be nearly 20 nm.[148] Chang et al. demonstrated that GO concentration and spin coating times affect the properties of conductive and transparent graphene films.[151] As the concentration and spin coating time increase, the transmittance value of thin films decreases.[151] In the thermal annealing step, GO films are exposed to higher temperatures under an inert atmosphere such as N_2, Ar, or vacuum to improve the reduction of GO. Wang et al. presented the production of graphene films with a sheet resistance of 1.8 ± 0.08 kΩ/sq and a transparency of over 70% at 1000−3000 nm by dip-coating method.[145] According to the results obtained, thermal annealing temperature and film thickness affect the electrical conductivity of the films.[145] Becerril et al. used the spin-coating method to produce thin films and demonstrated the formation of highly reduced GO thin films at 1100°C for 3 h in a vacuum.[148] They obtained thin films with sheet resistances in the range of $10^2 - 10^3$ Ω/square and 80% transmittance at 550 nm. Sa and Mahanandia performed thermal annealing of spin-coated RGO film at 400°C for 3 h under an inert atmosphere (Ar), resulting in a sheet resistance of 1.63 kΩ/sq with an optical transmittance of 92.63%.[143] Tas et al. performed a progressive thermal annealing process (at 70°C, 120°C, and 300°C) for spin-coated GO thin films without an inert atmosphere after chemical reduction.[139] According to the results, RGO thin films with 13.2 kΩ/sq surface resistivity and 45% transmittance were obtained.

CHAPTER 2

EXPERIMENTAL

2.1. Experimental Methodology

2.1.1. Synthesis and Characterization of Gold Nano- and Microplates Using Lyotropic Liquid Crystal

All chemicals used during the synthesis were obtained commercially and used without purification. Hydrogen tetrachloroaurate(III) trihydrate ($HAuCl_4 \cdot 3H_2O$, ≥99.9% purity), decaethylene glycol monododecyl ether (10-lauryl ether, $C_{12}EO_{10}$), sulfuric acid or SA (H_2SO_4, 95–97%), hexadecyltrimethylammonium bromide (CTAB, ≥99% purity), polyvinylpyrrolidone (PVP, Mw = 40000), lithium bromide (LiBr, ≥99% purity), sodium bromide (NaBr, ≥99% purity), potassium iodide (KI, 99-100.5% purity), and hydrogen peroxide (H_2O_2, 35%) were purchased from Sigma Aldrich. Potassium chloride (KCl, ≥99.5% purity) was obtained from Merck. Sodium chloride (NaCl, 99-100.5% purity) was obtained from Riedel-de Haen. Isopropyl alcohol (IPA, 99.5% purity) was purchased from Tekkim. All glassware was washed with piranha solution (H_2SO_4: H_2O_2 in 3:1 ratio by volume) and rinsed with alcohol, followed by Milli-Q water before use. Milli-Q water (18.2 MΩ cm resistivity at 25°C) was used in all of the experiments. The $HAuCl_4 \cdot 3H_2O$ stock solution was used within one week and stored at 5°C. All solutions used were freshly prepared.

The lyotropic liquid crystalline (LLC) mesophase of SA/$C_{12}EO_{10}$ was used to synthesize the gold (Au) nano- and microplates. The hexagonal mesophase of SA/$C_{12}EO_{10}$ with a 2.5 mole ratio was used throughout the synthesis. 62.6 mg of nonionic surfactant (10-lauryl ether, $C_{12}EO_{10}$) was weighed in a glass vial and dissolved in 100 µL of IPA. The solution was homogenized using a vortex mixer and a small magnetic stirrer. For the synthesis of Au plates, different aqueous concentrations of $HAuCl_4$ (5, 10, 20, 40, 50, and 55 µL, 0.97 M) were added to this homogeneous mixture with stirring at 300 rpm. The color of the solution changed from colorless to yellow immediately. To prevent surfactant carbonization, 13.9 µL of H_2SO_4 was added to the reaction medium at the last

step. The reaction was stirred at 22°C for 5-10 min. 15 µL of the solution was then drop-cast onto an alcohol-treated glass substrate (1 × 1 cm^2). The gel-like sample on the glass substrate was exposed to white light irradiation for different durations. A white light LED (MCWHL7-6500 K, 930 mW (Min), 1300 mA; Thorlabs) was used as the light source. The distance between the sample and the light source was 11 inches. Table 2.1 shows the different powers of white light (MCWHL7; Thorlabs) corresponding to specific wavelengths at 11 inches. The gel-like sample consisting of 20 µL of 0.97 M $HAuCl_4$ aqueous solution was also exposed to ultraviolet (UV) light using a 365 nm UV LED (M365L2-C1; Thorlabs) at ambient conditions. The products were washed twice with IPA to remove excess surfactant molecules. Au nanomaterials were kept in alcohol at 22°C for further characterization.

To investigate the effect of capping agents on Au plate formation, 20 µL of various CTAB and PVP concentrations (1 × 10^{-1}, 1 × 10^{-2}, 1 × 10^{-3}, 1 × 10^{-4}, and 1 × 10^{-5} M) were added separately to the reaction medium. 20 µL of 1 × 10^{-3} M NaBr, KCl, LiBr, KI, and NaCl were also added separately to the reaction medium to investigate the ion effect on the formation of the Au plate. Each sample was then exposed to white light for 24 h.

Table 2.1. Low, middle, and high power data of white light (MCWHL7; Thorlabs) corresponding to specific wavelengths at a distance of 11 inches.

Wavelength (nm)	Low power (mW)	Middle power (mW)	High power (mW)
400	5.05	11.5	95
500	1.75	4.10	33
600	1.08	2.50	20
700	0.80	1.80	15
800	0.60	1.38	11.4

2.1.2. Synthesis and Characterization of Reduced Graphene Oxide Thin Films Using Lyotropic Liquid Crystal

2.1.2.1. Synthesis of Graphene Oxide

All chemicals used during the synthesis were obtained commercially and used without purification. Graphite powder with a flake size of about 20 μm, sulfuric acid (H_2SO_4, 95–97%), and L-ascorbic acid ($C_6H_8O_6$) were purchased from Sigma Aldrich. Hydrochloric acid (HCl, 37%) was purchased from Carlo Erba. Hydrogen peroxide (H_2O_2, 35%) and ethanol (C_2H_5OH, 99.5% purity) were obtained from Tekkim. Milli-Q water (18.2 MΩ cm resistivity at 25°C) was used in all of the experiments. All glassware was washed with piranha solution (H_2SO_4: H_2O_2 in 3:1 ratio by volume) and then rinsed with alcohol and Milli-Q water before use. All solutions used were freshly prepared before synthesis.

Graphene oxide (GO) synthesis was a modified version of the works of Marcona et al.[126] and Ranjan et al.[129] A 9:1 ratio of H_2SO_4/H_3PO_4 (18:2 mL) was prepared separately. Each acid solution was cooled down to 5°C for 25 min to avoid a sudden rise in temperature during the reaction. These acid solutions were then transferred to the graphite powders (0.15 g, 1 weight equivalent) under stirring at room temperature (RT). The acid-graphite mixture was sonicated in ice water for 10 min to allow the acids to penetrate the graphite layers better and to reduce the size of the graphite flakes. Before adding $KMnO_4$ (0.90 g, 6 weight equivalents) to the reaction medium, it was ground in a mortar for several min to reduce particle size. Small portions of $KMnO_4$ were added to the constantly stirred reaction at RT. The reaction solution turned green with the addition of $KMnO_4$. The reaction mixture was then heated at 50°C for 24 h with continuous stirring at 300 rpm. After 24 h, a brown paste-like solution was obtained. The reaction solution was cooled to RT and deionized (DI) water ice (20 mL) was added. To decompose the insoluble metal salts, 35% H_2O_2 was added by stirring until the foaming stopped in the solution. The color of the solution then changed from brown to golden yellow. For purification of GO, the resulting solution was first washed by centrifugation at 9000 rpm for 10 min and the supernatant was discarded. The remaining precipitate was washed sequentially with 1M of HCl (x2) and DI water (x3) by centrifugation until the pH was 5-7. The final gel form was dried at RT to obtain powder GO.

2.1.2.2. Preparation of Hexagonal Phase of Lyotropic Liquid Crystal

The hexagonal mesophase of LLC was prepared with 10-lauryl ether ($C_{12}EO_{10}$), a nonionic surfactant, and sulfuric acid (H_2SO_4, SA), a strong acid. 2.4 SA/$C_{12}EO_{10}$ mole ratio was used to prepare the stable hexagonal mesophase of LLC under ambient conditions. 627 mg of $C_{12}EO_{10}$ was mixed with 134 µL of H_2SO_4 (as solvent) in a closed glass vial and then homogenized using a vortex, followed by a magnetic stirrer. This gel-like composition exhibits characteristic fan texture under a polarized optical microscope (POM).

2.1.2.3. Preparation of Reduced Graphene Oxide Thin Films Using a Lyotropic Liquid Crystal Template

An aqueous dispersion of GO at different concentrations (2.5 mg/mL, 5 mg/mL, 10 mg/mL, 15 mg/mL, and 20 mg/mL) was prepared by dissolving GO powder in 2 mL of DI water. Each composition in a sealed glass vial was subjected to an ultrasonic bath with ice water for homogenization. The reason for using ice water during homogenization is to prevent the reduction of GO before film fabrication. In the next step, the GO solution was added to the LLC gel and mixed overnight (at 350 rpm) until thoroughly homogenized under ambient conditions. Then, 240 µL of 0.68 M L-ascorbic acid was then added to this solution for the chemical reduction process. For film fabrication, the surface of the glass (2.5 × 1.6 cm^2) and quartz substrates were treated with piranha solution before spin-coating to make the surface hydrophilic. 100 µL of homogenized solution was spin-coated onto these glass or quartz substrates. Spin parameters were set at 1000, 1500, 2000, 2500, 3000, and 3500 rpm for 1 min. each. After the spin coating process, it was waited for about 15 min for the solution to gel on the substrates. The thin films were transparent, colorless, and gel-like. These thin films were kept in a furnace at 80°C for 1 h to chemically reduce GO in the presence of LLC. The thin films were then kept in ethanol for 16 h to remove surfactant and acid residues. As a final step, thermal annealing of the films was carried out under an inert atmosphere (in vacuum and Argon) by increasing the temperature from ambient temperature to 300°C within 1 h and keeping these films at this temperature for 2 h. In another thermal annealing parameter, the temperature was rapidly increased from ambient temperature to 1000°C and the films

were held at this temperature for 30 min under an inert atmosphere (Ar and H_2 flow). Finally, black-colored reduced GO (RGO) thin films were obtained. These steps were also applied to RGO thin film fabrication without using the LLC mesophase.

2.2. Instrumentation

2.2.1. Polarized Optical Microscopy

A polarizing optical microscope (POM) was used to characterize LLC mesophases. POM images were obtained with 10X and 20X optical lenses using a Meiji Techno ML9400 series Polarizing Microscope and a Leica DM1750 M Reflected Light Polarized Metallurgical Microscope. To determine the phase behavior of gel samples, the samples were coated on microscope slides by drop-cast or spin-coating processes and characterized by POM after evaporation of the excess solvent.

2.2.2. Scanning Electron Microscopy

A scanning electron microscope (SEM) was used to investigate the morphology of the products. SEM images were obtained using an FEI Quanta 250 FEG (Hillsboro, OR, USA) with an acceleration voltage of 15 kV. For the preparation of SEM samples, the products were dispersed in alcohol (isopropyl alcohol or ethanol) and a few drops of the sample were deposited on a freshly cleaned silicon wafer, followed by air-dried at RT. The graphite powder was analyzed by placing the material directly on a carbon adhesive tape. The same samples were also used for elemental analysis by energy-dispersive X-ray spectroscopy (EDX) under the same microscope.

2.2.3. Scanning Transmission Electron Microscopy

Scanning transmission electron microscope (STEM) images were recorded using an FEI Quanta 250 FEG (Hillsboro, OR, USA) at an accelerating voltage of 25 kV. For STEM analysis, nanomaterials were dispersed in alcohol and dropped onto 300-mesh carbon-coated copper grids (Agar Scientific Ltd).

2.2.4. X-Ray Diffraction

X-ray diffraction (XRD) analysis was performed for phase identification of synthesized materials and LLC samples. XRD patterns were collected using a Philips X'Pert Pro Diffractometer equipped with a Cu-Kα (λ=1.54056 Å) source and operating at 45 kV and 40 mA. Au plate samples for XRD analysis were prepared by spreading the materials on sample holders and dried at ambient temperature. The measurements were recorded over a 2θ range from 10° to 80° with a scan rate of 0.04°/sec at 0.02 data intervals. The LLC solution was spread over a substrate and excess solvent was evaporated under ambient conditions to form a gel phase. XRD analysis for LLC gel samples was performed between 1.5° and 5° 2θ range at a scan rate of 0.08°/sec. The measurement of graphite, GO, and RGO powders was performed in the 2θ range from 3° to 80° with a scan rate of 0.02°/sec at 0.02 data intervals.

2.2.5. Atomic Force Microscopy

An atomic force microscope (AFM) was used to investigate the thickness of Au plates and RGO thin films. The analysis was performed using a Multimode Nanoscope 8 scanning probe microscope (Bruker, USA) in ScanAsyst and contact modes. AFM images were obtained using triangular silicon nitride cantilever tips with a force constant of 0.4 N m^{-1}, a resonance vibration frequency of 70 kHz, and a tip radius <10 nm. Au samples were dispersed in alcohol and a few drops of this solution were spread on freshly cleaned silicon wafers, then evaporated at RT. The thickness of the RGO thin film was obtained by scratching the film without damaging the substrate.

2.2.6. Ultraviolet-Visible Spectroscopy

Ultraviolet-Visible (UV-Vis) analysis was performed to obtain the absorption and transmission spectra of the materials. The absorption spectrum of 0.05 mg/mL GO aqueous solution was obtained using a Shimadzu UV-2550 UV-Vis Spectrophotometer in the wavelength range of 200-800 nm. The optical transparency of RGO thin films was measured using a fiber-coupled spectrometer (USB4000, Ocean Optics) equipped with a

deuterium-tungsten halogen light source (DH2000-BAL, Ocean Optics) in the UV to NIR region (200-1100 nm).

2.2.7. Fourier Transform Infrared Spectroscopy

Fourier transform infrared spectroscopy (FT-IR) was used to investigate the functional groups of the synthesized materials. FT-IR analysis was carried out using PerkinElmer Spectrum UATR Two FT-IR Spectrometer with attenuated total reflectance (ATR) mode. GO and RGO powders were placed onto the surface of the ATR diamond and analyzed in the range of 4000-400 cm^{-1}.

CHAPTER 3

RESULTS AND DISCUSSION

3.1. Synthesis and Characterization of Gold Nano- and Microplates Using Lyotropic Liquid Crystal

The synthesis of 2D single crystalline gold (Au) nano- and microplates has been obtained from the acidic LLC mesophase consisting of sulfuric acid (H_2SO_4, SA) and oligo-type nonionic surfactant, 10-lauryl ether ($C_{12}EO_{10}$). Firstly, a 2.5 mole ratio of the SA/$C_{12}EO_{10}$ hexagonal LLC mesophase was prepared and mixed with a 20 µL of 0.97 M $HAuCl_4$ aqueous solution (gold precursor). Here, the mole ratio of $HAuCl_4/C_{12}EO_{10}$ is 1.94×10^{-1}. POM images of the characteristic focal conic fan textures of 2D hexagonal mesophases were observed before and after the addition of $HAuCl_4$ to the SA/$C_{12}EO_{10}$ system at ambient conditions (see Figure 3.1). However, the SA/$C_{12}EO_{10}$/$HAuCl_4$ system forms a stable hexagonal LLC mesophase until the mole ratio of $HAuCl_4/C_{12}EO_{10}$ is 5.34×10^{-1}. Moreover, a stable SA/$C_{12}EO_{10}$/$HAuCl_4$ system cannot be obtained under atmospheric conditions when the Au precursor is mixed with a 1.25 mole ratio (hexagonal) or 5 mole ratio (micelle cubic) of the SA/$C_{12}EO_{10}$ LLC mesophases.

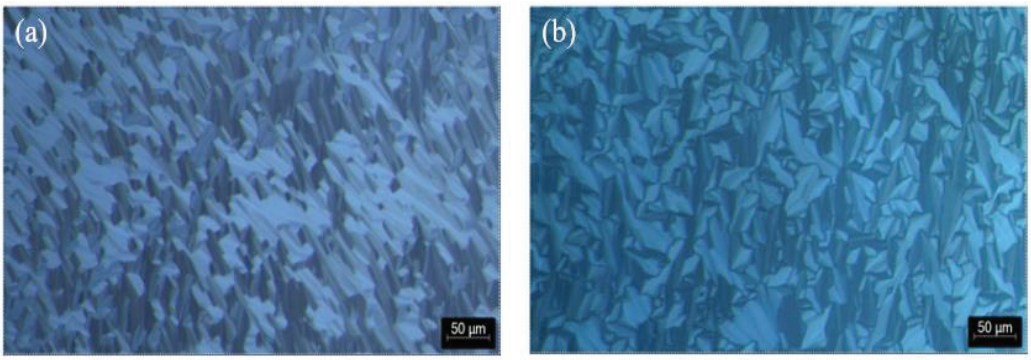

Figure 3.1. POM textures of (a) the 2.5 mole ratio of SA/$C_{12}EO_{10}$ and (b) the SA/$C_{12}EO_{10}$/$HAuCl_4$ hexagonal LLC mesophases.

A few drops of homogeneous SA/$C_{12}EO_{10}$/$HAuCl_4$ solution were dropped onto a glass substrate and exposed to white light for 13.5 h. The effects of three different white

light powers as low, middle, and high on Au plate formation were investigated. At a wavelength of 400 nm and at a distance of 11 inches, the value of low, middle, and high powers indicates 5.05, 11.5, and 95 mW, respectively. The products formed on the glass substrate by light irradiation were washed with isopropyl alcohol and sealed in a glass vial or glass test tube (see Figure 3.2). Over time, a bright golden glittering product precipitated at the bottom of the glass test tube and the supernatant became colorless. In medium power irradiation synthesis, it was observed that more Au material precipitated than the others. In high power irradiation synthesis, the dark color of the product precipitated at the bottom of the glass tube indicating nanoparticle formation instead of plate.

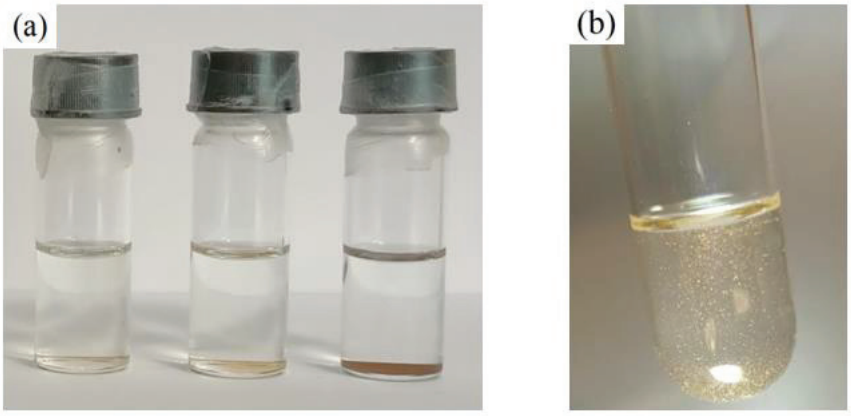

Figure 3.2. Au products formed (a) after low, middle, and high power white light irradiations (from left to right) and (b) with high efficiency as a result of middle power irradiation.

As can be seen from the SEM images in Figure 3.3(a-c), Au plates with triangular, truncated triangular, hexagonal, and gear-like disc and hexagonal plate structures were obtained by low and middle power light irradiation. The products obtained by low power irradiation have a large amount of truncated icosahedral Au nanostructures as well as different anisotropic Au plate shapes (see Figure 3.3(a,b)). On the other hand, Au plate structures are dominant in the products obtained by middle power irradiation (see Figure 3.2c). The morphology formed at the end of the reaction in high power light is mainly spherical Au nanoparticles (see Figure 3.3d). As shown in Figure 3.4(a-d), the addition of Au precursor ($HAuCl_4 \cdot 3H_2O$) to the $SA/C_{12}EO_{10}$ LLC mesophase, followed by light irradiation leads to the formation of Au plates with triangular, truncated triangular, hexagonal, and gear-like morphology.

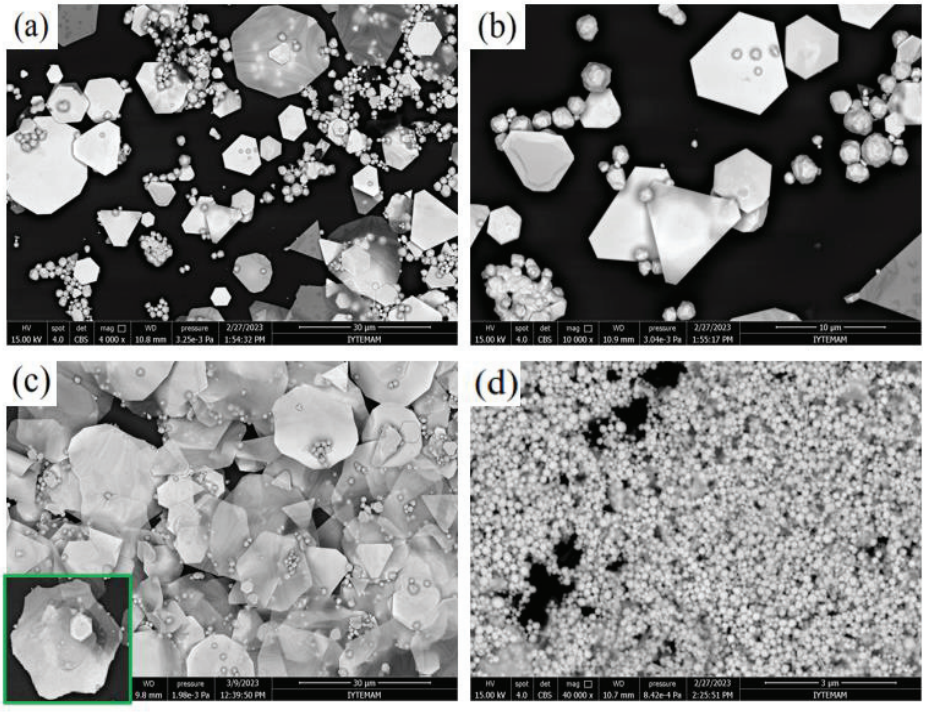

Figure 3.3. SEM images of Au materials resulting from 13.5 h irradiation of SA/$C_{12}EO_{10}$/$HAuCl_4$ LLC mesophase with (a) and (b) low power at low and high magnifications, respectively, (c) middle power, and (d) high power white light.

In Au plate synthesis of both low and middle power irradiation, truncated triangular, hexagonal, and gear-like shapes were obtained more than sharp-edged triangular shapes. Low power light irradiation products have large amounts of truncated icosahedrons instead of plates and some of these nanostructures are fused to form non-uniform aggregates. These truncated icosahedrons grow on anisotropic plates and distort their structures. On the other hand, Au plates are superior to icosahedrons in the reaction products obtained by middle power light irradiation. In this synthesis, the amount of material precipitated in the glass test tube is greater than in the low power irradiation synthesis.

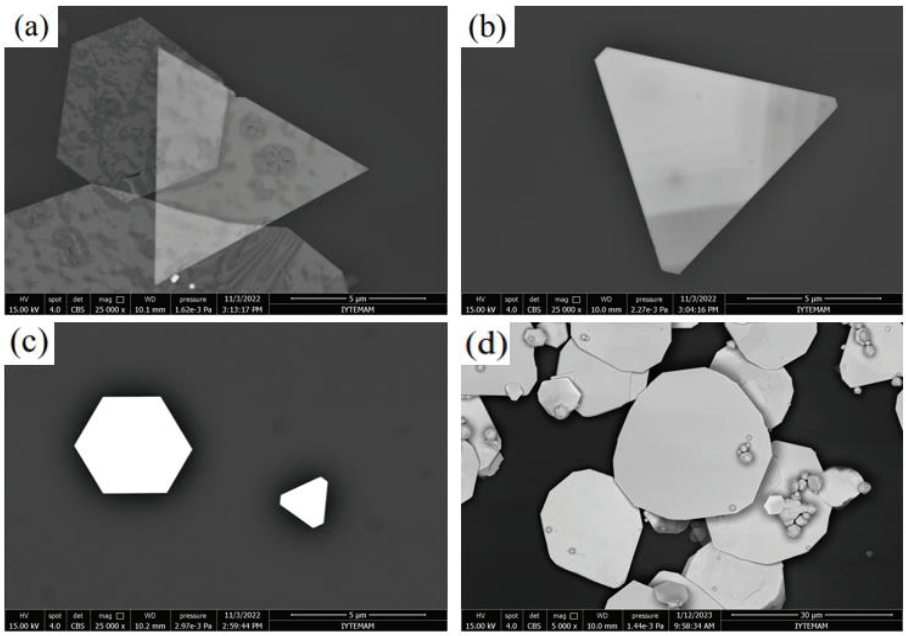

Figure 3.4. Different Au plate geometries formed in SA/$C_{12}EO_{10}$/$HAuCl_4$ mesophase by white light irradiation: (a) triangular, (b) truncated triangular, (c) hexagonal, and (d) gear-like.

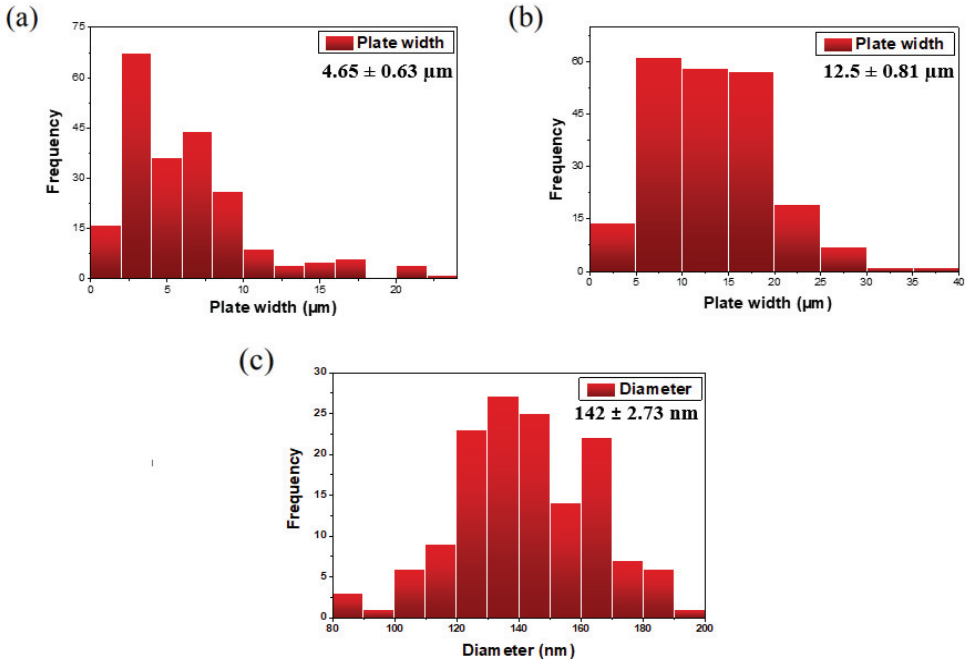

Figure 3.5. Histograms of the size distributions for Au products obtained by (a) low, (b) middle, and (c) high power white light irradiations.

The size distribution of the obtained Au materials are shown with the histograms in Figure 3.5. The size ranges of Au plates are about 1–22 μm in width by low power irradiation synthesis (see Figure 3.5a). Compared to low power irradiation, medium power irradiation synthesis yields larger sized Au plates up to about 39 μm in width (see Figure 3.5b). The average sizes of Au plates obtained from the low and middle power irradiation synthesis are 4.65 ± 0.63 μm and 12.5 ± 0.81 μm, respectively. Uniform spherical Au nanoparticles with a diameter of 142 ± 2.73 nm predominate in the morphology formed as a result of the reaction in the high power light irradiation (see Figure 3.5c).

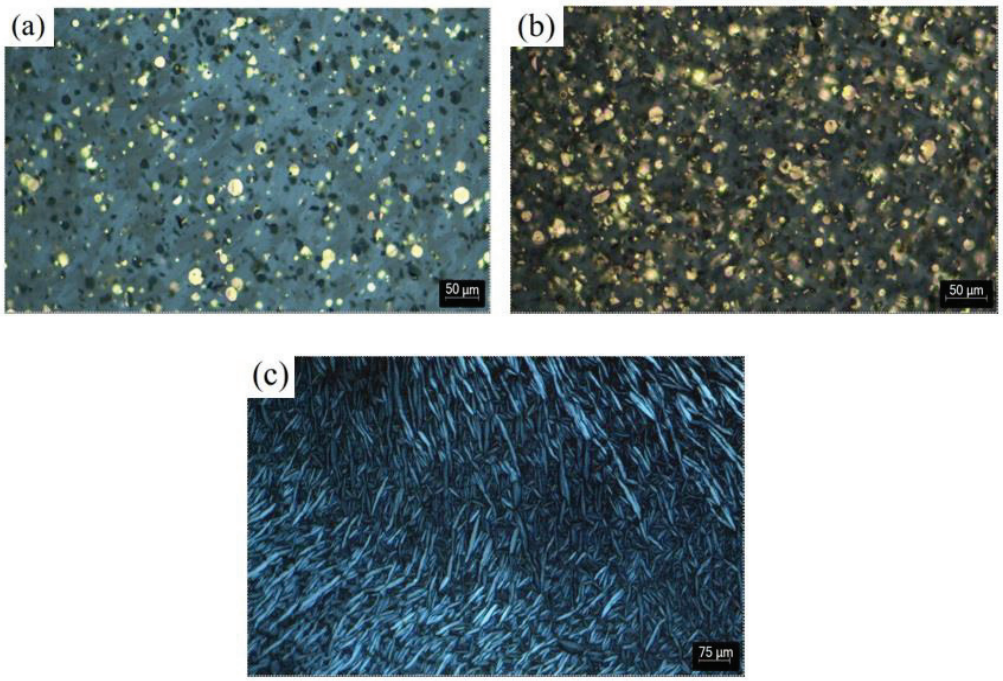

Figure 3.6. POM images of the SA/$C_{12}EO_{10}$/$HAuCl_4$ LLC mesophase after (a) low, (b) middle, and (c) high power white light irradiations.

The POM images after the Au material synthesis on the glass substrate are shown in Figure 3.6. After Au material synthesis, the LLC gel form was still present on the glass substrate and the hexagonal phase was stable under atmospheric conditions. In addition to the SEM image, the POM image of Au products synthesized by high power irradiation differs from other images due to the Au nanoparticle formation. It is understood from the POM images that large amounts of Au plates are formed in the middle power irradiation. The middle power irradiation synthesis of Au materials has been investigated for further characterization due to high-efficiency plate production.

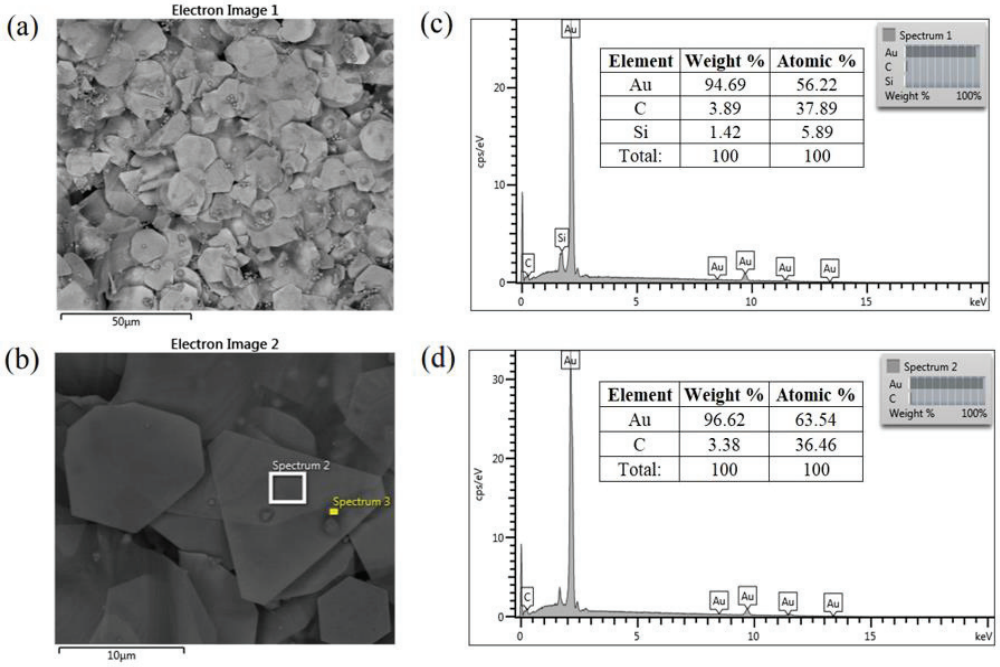

Figure 3.7. SEM images of the Au plates at (a) low and (b) high magnifications. (c,d) EDX spectra of Au plates.

EDX spectra of Au plates were obtained from both low and high magnification SEM images (see Figure 3.7). The strong Au peak appears in both EDX spectra since the pure single-crystalline Au plates are composed of elemental Au. Because the Au plates obtained in the synthesis were very thin, a weak substrate (silicon, Si) peak was detected in the EDX analysis. The other weak peak represents carbon (C) which appears in the spectra due to surfactant residues.

LLC mesophases result in a low-angle XRD pattern due to the large spacing between layers of atoms in the crystal lattice. The samples prepared from the mole ratio of 2.5 SA/$C_{12}EO_{10}$ give a diffraction pattern at around 2°, 2θ, as shown in Figure 3.8. However, the addition of aqueous $HAuCl_4$ solution to this LLC mesophase increases the d-spacing values and results in a diffraction pattern shifted to a smaller angle than 2°, 2θ (see Figure 3.8). Consequently, the SA/$C_{12}EO_{10}$ LLC mesophase with a certain amount of $HAuCl_4$ shows a 2D hexagonal phase (H_1) at ambient conditions.

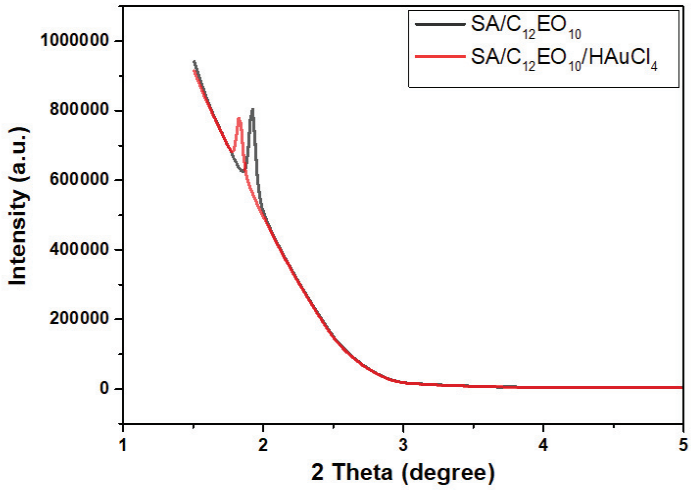

Figure 3.8. XRD pattern of $SA/C_{12}EO_{10}$ and $SA/C_{12}EO_{10}/HAuCl_4$ LLC mesophases.

The single crystallinity of the Au plates was demonstrated by XRD measurements. As shown in Figure 3.9, the XRD pattern has four diffraction peaks representing the characteristic diffraction of elemental Au^0 metal. It has a much stronger characteristic diffraction peak found at $2\theta = 38.2^\circ$ and represents the {111} facets of face-centered cubic (fcc) Au. This means that the Au plates are mainly oriented along the (111) plane. The other three diffraction peaks at $2\theta = 44.5^\circ$, 64.7°, and 77.6° are assigned to the {200}, {220}, and {311} lattice planes, respectively (JCPDS #04-0784).

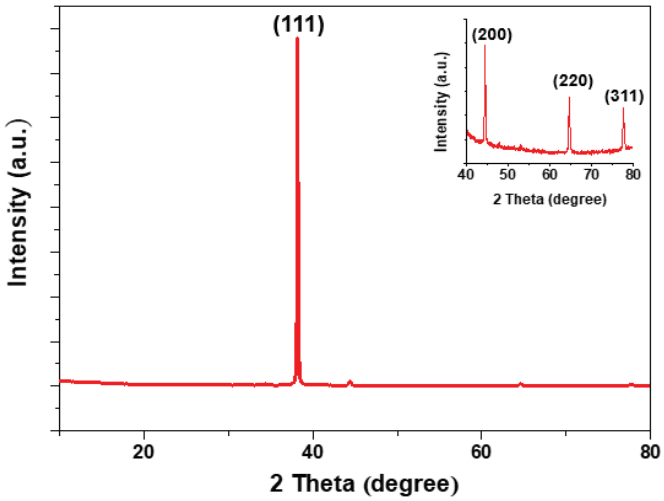

Figure 3.9. XRD pattern of Au plates synthesized by middle power light irradiation.

AFM images and surface height profiles of Au plates with different morphologies are shown in Figure 3.10. The synthesized Au nano- and microplates are almost flat and broad rather than bumpy. The surface of some plate structures is surrounded by Au nanoparticles or aggregates, which cause bumps in their height profiles (see Figure 3.10b). Some deformations may occur on the surface of the Au plates during the transfer of materials from the solution to the silicon substrate. To avoid these deformations, the samples were washed in alcohol for several days instead of centrifugation during purification. Some Au plates may also have concave centers rather than flat height profiles (see Figure 3.10d). The height profiles demonstrate that the Au microplate thickness varies in a wide range between 50 and 150 nm.

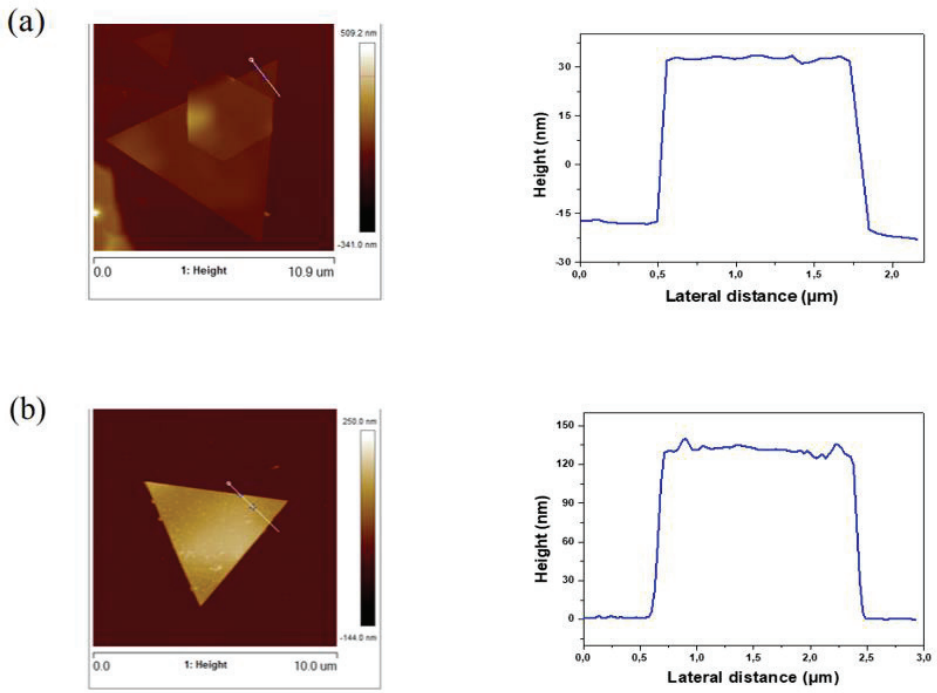

Figure 3.10. (a-e) AFM images and height profiles of the purified micrometer-sized Au plates.

(Figure cont. on next page)

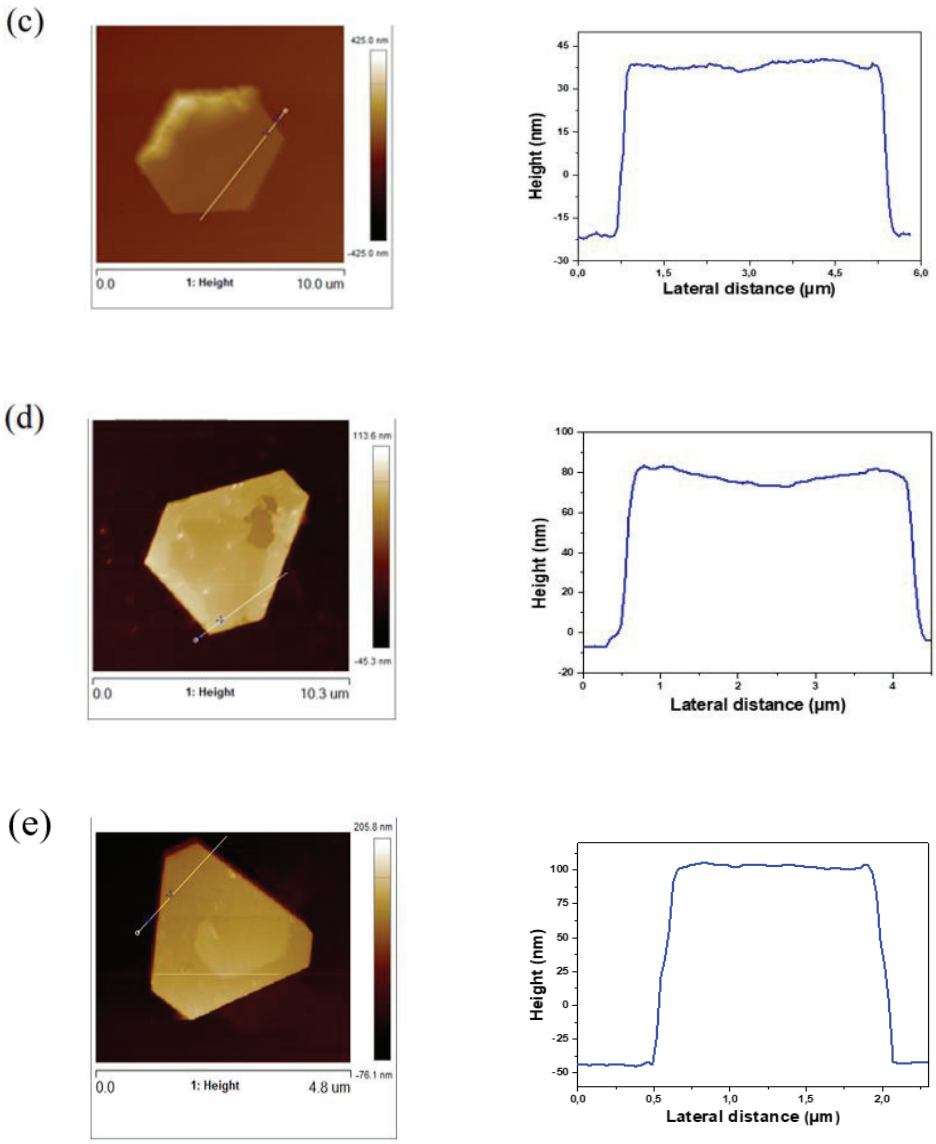

Figure 3.10 (cont.).

As shown in Figure 3.11, there are two steps in the Au plate formation mechanism: nucleation and growth. Firstly, Au^{+3} ions are reduced to Au^{0} atoms by the EO chains of the nonionic surfactant in the LLC confining space. Secondly, these gold nuclei grow anisotropically to form Au nano- and microplates of different shapes such as triangular, truncated triangular, hexagon, or gear-like. Due to the lowest surface energy of the {111} facets of the Au nuclei, preferential adsorption of surfactant molecules occurs along the (111) plane, as confirmed by XRD analysis.

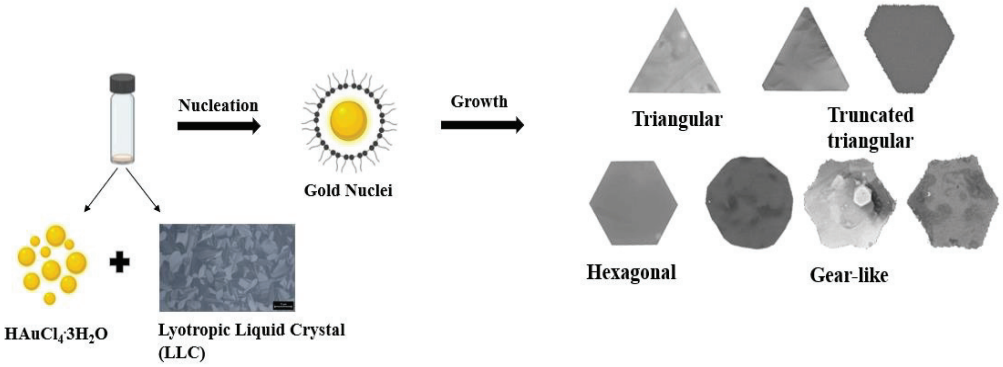

Figure 3.11. Schematic representation of Au plate formation.

Time-dependent experiments have been performed in order to understand the mechanism of Au plate formation in an LLC environment by a photochemical approach. Figure 3.12 shows STEM images of Au samples exposed to white light for different durations. After the homogeneous solution was formed and without exposure to white light, monodisperse coral-shaped nanoparticles were observed in the sample (see Figure 3.12a). These nanoparticles consist of distorted nanorods and spherical aggregates. When the sample was exposed to light for about 5 min, besides monodisperse coral-shaped nanoparticles, spherical nanoparticles, nanorods, and nanoprisms were seen (see Figure 3.12b). After 30 min of light irradiation, Au nanoparticles with highly efficient anisotropic shapes formed and hexagon-shaped nanoparticles began to appear (see Figure 3.12c). Spherical nanoparticles, anisotropic structures, and micrometer-sized plates were formed when the irradiation time was 2 h (see Figure 3.12d). As shown in Figure 3.12e, the growth in plate structures was achieved when the irradiation time was further increased.

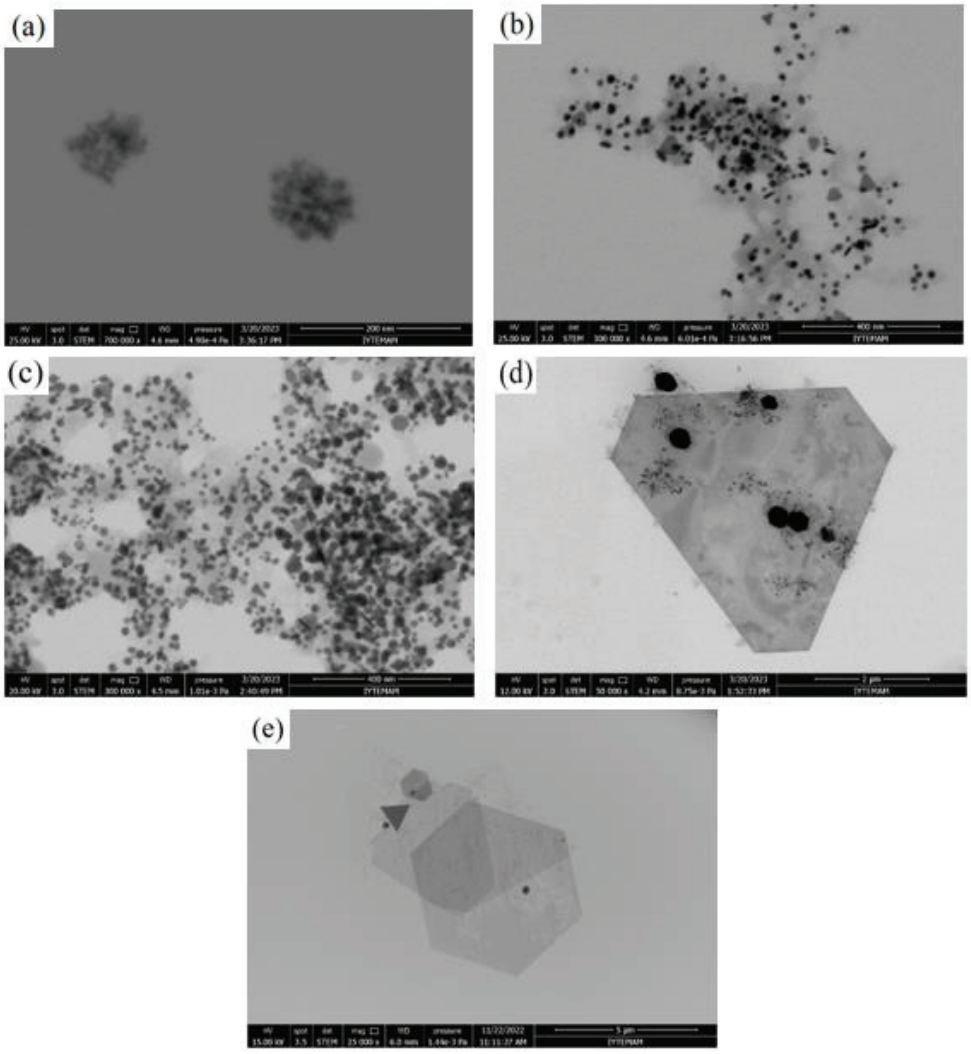

Figure 3.12. STEM images of Au materials obtained from the white light irradiation after (a) 0 min, (b) 5 min, (c) 30 min, (d) 2 h, and (e) 13.5 h.

LLC-mediated Au plate synthesis takes a long time without white light catalysis. SEM images of Au samples kept in light-free and laboratory conditions are shown in Figure 3.13. A small amount of plate formation was observed even if the samples were kept in a dark environment or laboratory conditions for approximately one week (see Figure 3.13(a,b)). As shown in Figure 3.13(c,d), highly efficient Au plate formation was detected in the sample left in laboratory conditions for about two weeks. The sample contains mainly triangular, truncated triangular, and hexagonal shapes with a few truncated icosahedral nanostructures. The average size of single-crystalline Au microplates is about 19.8 ± 0.63 μm. Gear-like Au plates are not commonly observed among the final products. If the sample is left in ambient laboratory conditions for a longer time, the edges of the large hexagonal structures may be truncated and turned into

the disc-like gear shapes. Au plates formed under laboratory conditions have sharper and smoother edges than Au plates formed under white light irradiation. In addition, fewer nanoparticles are formed on these anisotropic structures. As can be understood from the SEM images, the structures grow more regularly without using white light during the reaction. However, the reduction rate of Au^{+3} is extremely slow and it takes several weeks to form highly efficient Au plates in the absence of white light.

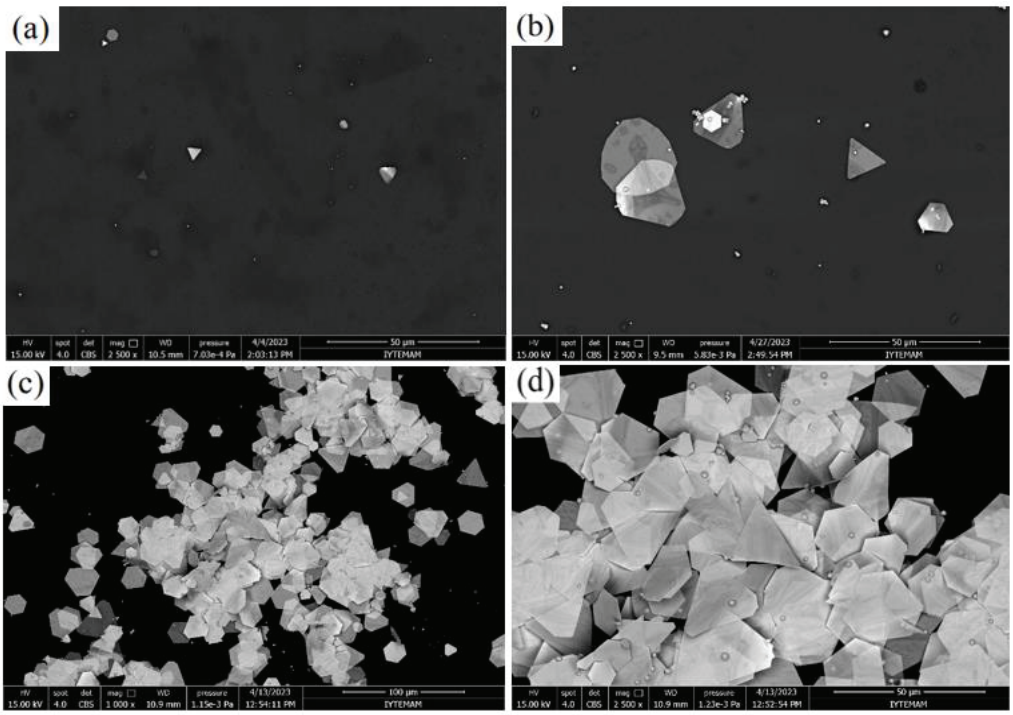

Figure 3.13. SEM images of Au plates formed in (a) light-free and (b) laboratory conditions after nearly one week. (c) and (d) Low and high magnification SEM images of Au plates formed under laboratory conditions after nearly two weeks.

In order to determine the effect of irradiation time on Au plate size, the sample was exposed to white light for certain periods. The product yield in the sample exposed to the white light for 6 h is relatively low when compared to the others. As can be seen from the SEM images in Figure 3.14a, some plates are in roll form as they are ultrathin. After 6 h of reaction, gear-like hexagonal plates are usually obtained instead of disc-shaped plates. Besides, the average size of the Au plates is 6.0 ± 0.73 μm in width. It has been determined that as the reaction time increases, micrometer-sized triangles lose their sharp edges and turn into truncated triangles. In general, the size of triangles with sharp edges usually varies between 1.5 and 8.6 μm. Also, large plate sizes up to 39 μm are

obtained from gear-like plates. As can be seen from the SEM images in Figure 3.14(b-d), the product morphology obtained in the samples exposed to white light for 13.5 h, 24 h, and 6 d is almost the same. Figure 3.15 shows the histograms for the size distribution of Au plates synthesized at different reaction times. After 13.5 h of reaction, more uniform-sized products are obtained with an average width of 12.5 ± 0.81 μm. When the reaction time is increased to 6 d, the average Au plate size decreases to 10.2 ± 0.64 μm. Although almost the same average plate size is obtained after 24 h and 6 d of reaction time, the size of the plates becomes more uniform after 24 h of reaction.

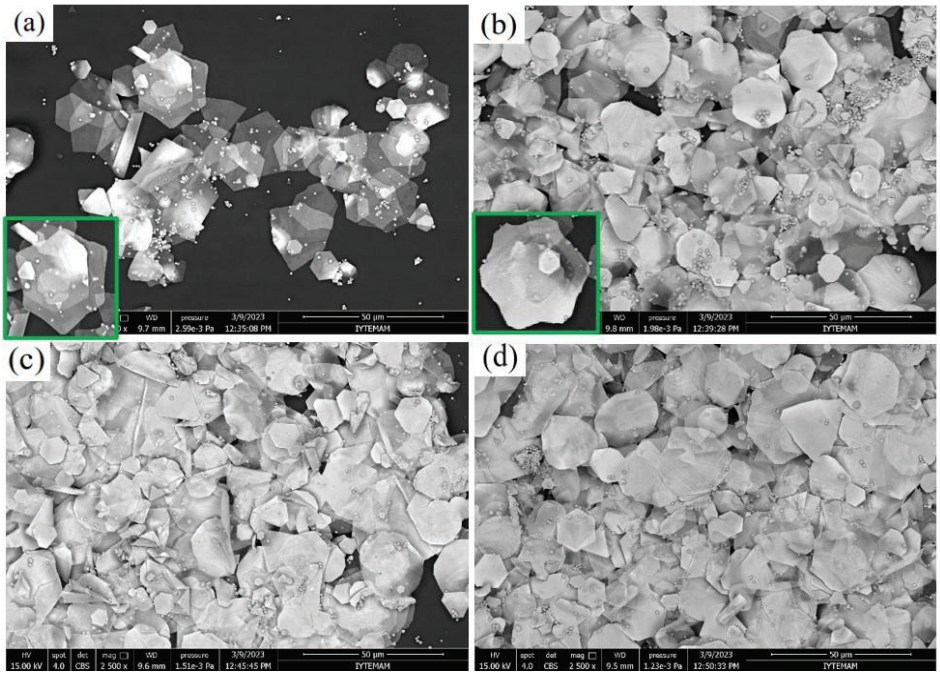

Figure 3.14. SEM images of Au samples exposed to the white light after (a) 6 h, (b) 13.5 h, (c) 24 h, and (d) 6 d.

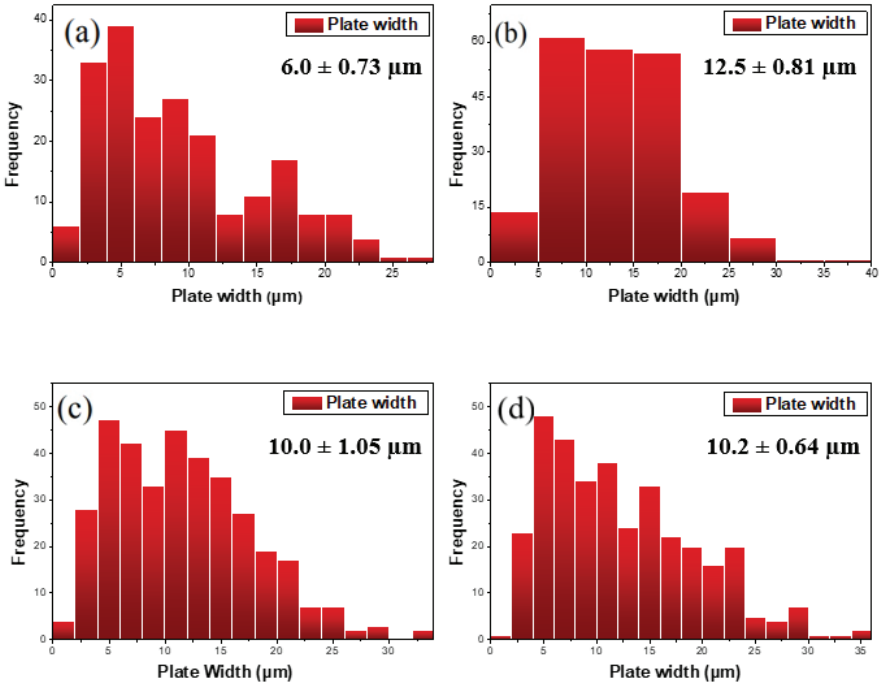

Figure 3.15. Histograms for the size distribution of Au plates synthesized after (a) 6 h, (b) 13.5 h, (c) 24 h, and (d) 6 d.

The effect of aqueous $HAuCl_4$ concentration on product morphology was investigated in $SA/C_{12}EO_{10}$ LLC medium. Figure 16 shows SEM images of Au products formed after adding different concentrations of $HAuCl_4$ solution to the LLC medium. The plates are embedded with spherical nanoparticles and truncated icosahedron structures at relatively low $HAuCl_4$ concentrations (see Figure 3.16(a,b)). At low $HAuCl_4$ concentrations, the Au plates generally tend to fold and roll due to their ultra-thin nature. At medium $HAuCl_4$ concentration, plate formation predominates in products rather than truncated icosahedrons (see Figure 3.16c). The average Au plate size for the 1.94×10^{-1} mole ratio of $HAuCl_4/C_{12}EO_{10}$ is 10.0 ± 1.05 µm (see Figure 3.15c). Further increase of $HAuCl_4$ concentration causes deformations on the plates due to the aggregation of icosahedrons (see Figure 3.16(d-f)). At relatively high $HAuCl_4$ concentrations, the Au icosahedron and plate structures compete with each other throughout the growth process.

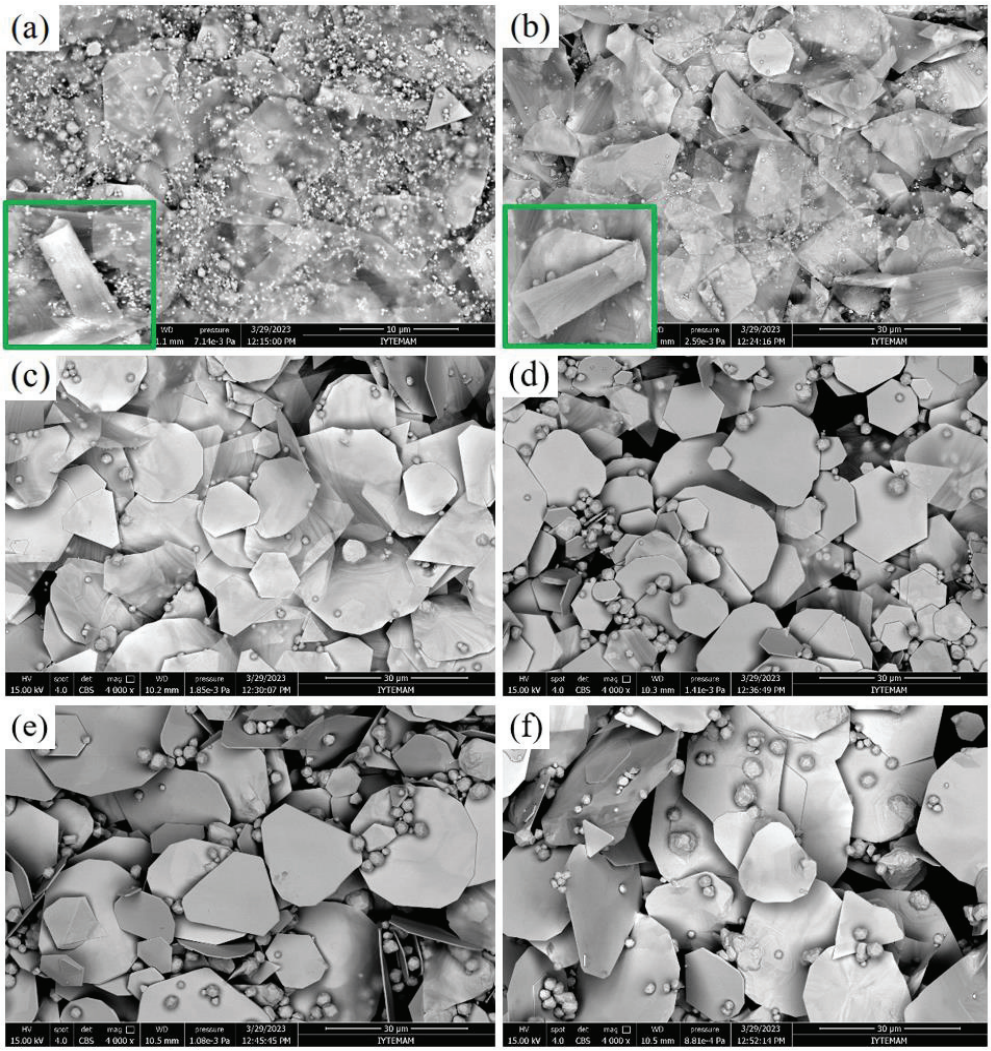

Figure 3.16. SEM images of Au products synthesized with different mole ratios of $HAuCl_4/C_{12}EO_{10}$. (a) 4.86×10^{-2}, (b) 9.71×10^{-2}, (c) 1.94×10^{-1}, (d) 3.89×10^{-1}, (e) 4.86×10^{-1}, and (f) 5.34×10^{-1}.

The thicknesses of Au plates synthesized with different $HAuCl_4$ concentrations were investigated using AFM. According to the AFM height profiles of the plates in Figure 3.17, increasing $HAuCl_4$ concentration causes an increase in plate thickness. However, the plates do not have a uniform thickness for each $HAuCl_4/C_{12}EO_{10}$ composition. The formation of Au nanostructures and/or deformations on the plates may have caused fluctuations in the thickness measurement. For a mole ratio of 4.86×10^{-2} $HAuCl_4/C_{12}EO_{10}$, the thickness of the Au plates is usually measured as 31 and 45 nm (see Figure 3.17a). When the $HAuCl_4/C_{12}EO_{10}$ mole ratio increases to 9.71×10^{-2}, the thickness of the plates varies between 51 and 60 nm (see Figure 3.17b). The plate thickness reaches 258 nm when the mole ratio of $HAuCl_4/C_{12}EO_{10}$ is 1.94×10^{-1} (see

Figure 3.17c). As the $HAuCl_4$ concentration increases further (3.89×10^{-1} mole ratio of $HAuCl_4/C_{12}EO_{10}$), the plate thickness reaches 420 nm (see Figure 3.17d).

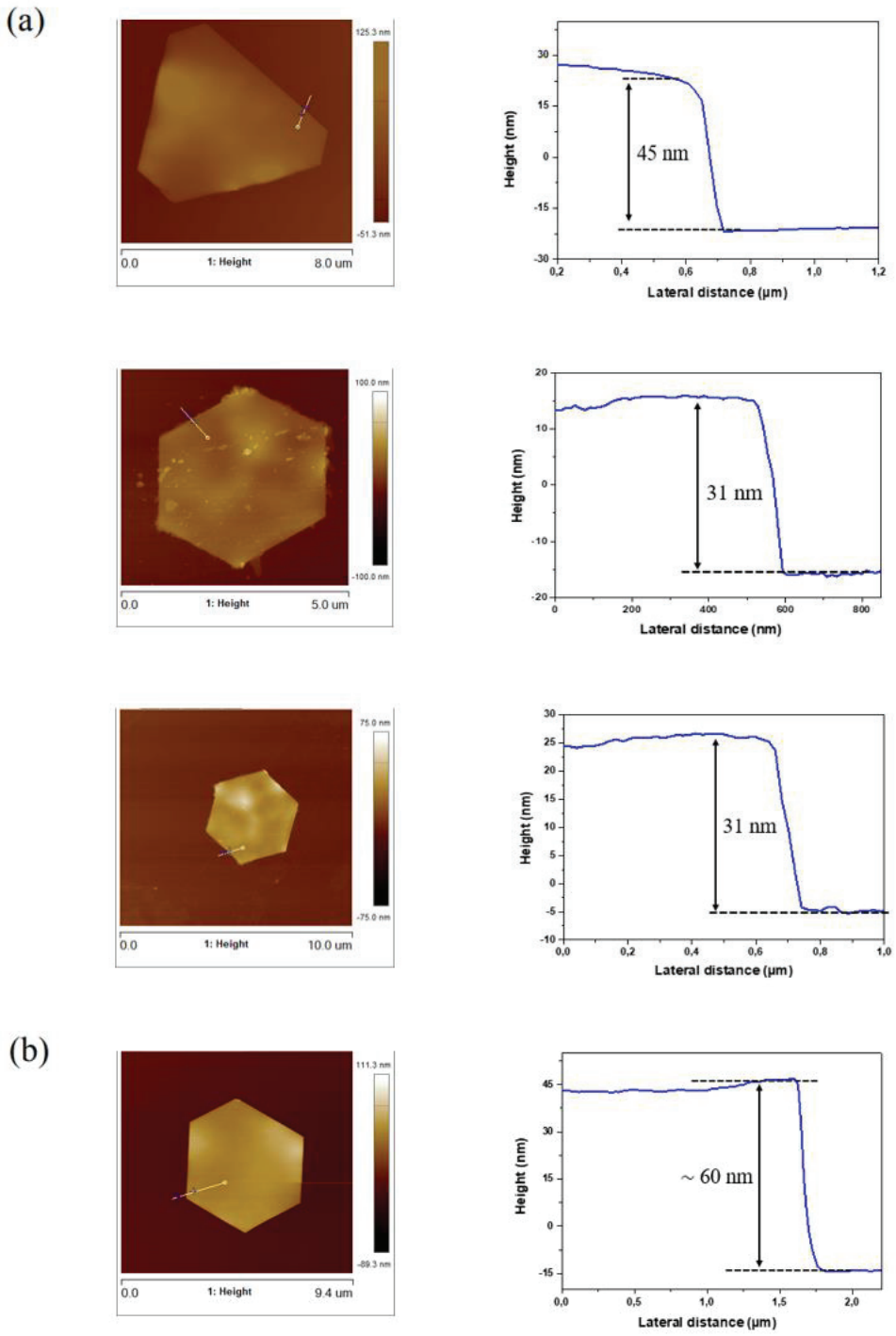

Figure 3.17. AFM images and height profiles of the purified Au plates obtained with different $HAuCl_4/C_{12}EO_{10}$ mole ratios. (a) 4.86×10^{-2}, (b) 9.71×10^{-2}, (c) 1.94×10^{-1}, and (d) 3.89×10^{-1}.

(Figure cont. on next page)

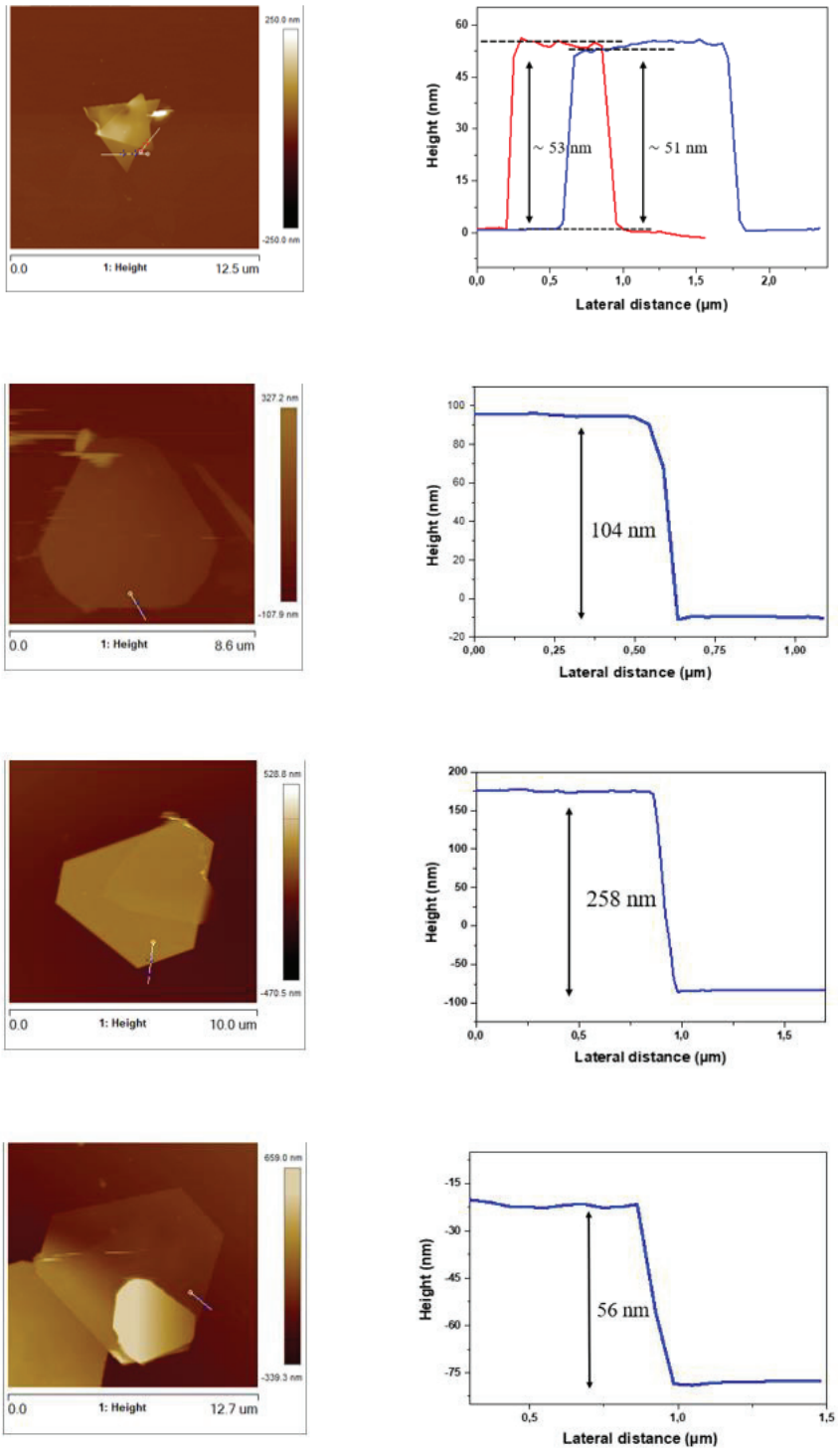

Figure 3.17 (cont.).

(Figure cont. on next page)

(d)

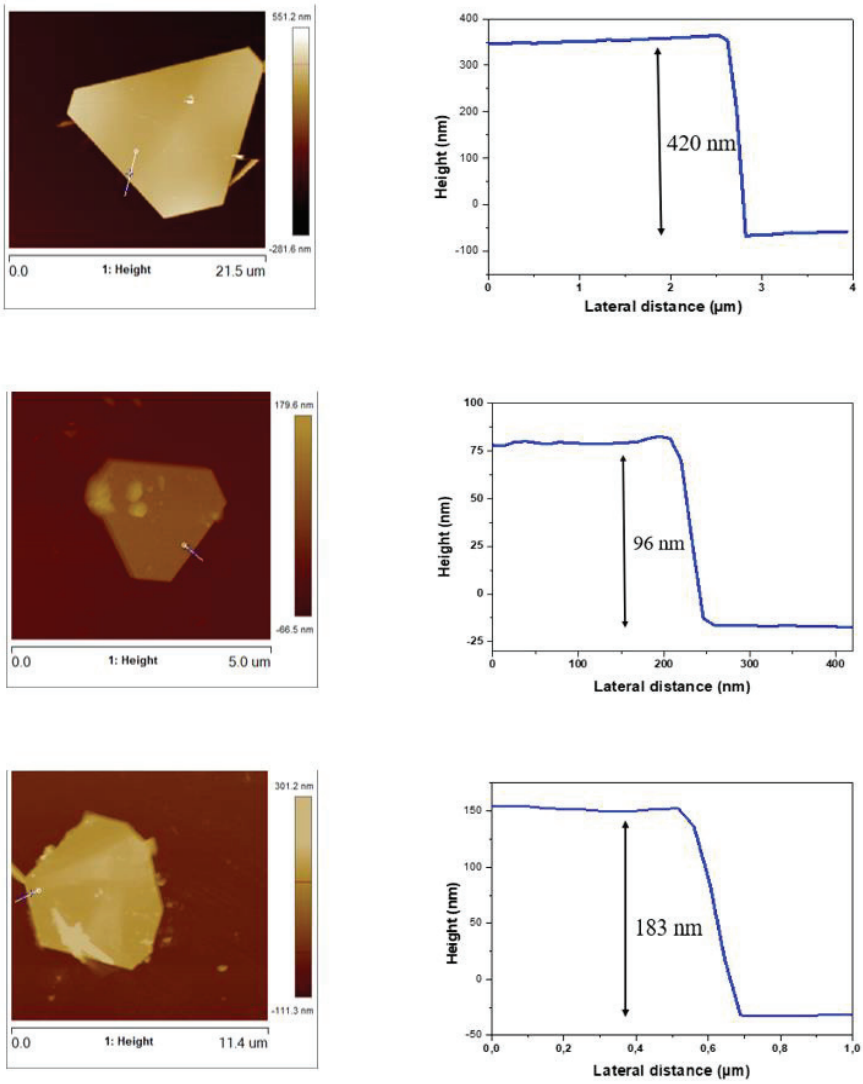

Figure 3.17 (cont.).

The capping agents CTAB and PVP were used to investigate their effects on the morphology and size of Au plates. Different concentrations of capping agents were added to the 1.94×10^{-1} mole ratio of $HAuCl_4/C_{12}EO_{10}$ medium. The sample was then exposed to white light for 24 h. SEM images of Au products prepared by using different molar ratios of capping agents to $HAuCl_4$ are given in Figure 3.18. At higher CTAB/$HAuCl_4$ or PVP/$HAuCl_4$ molar ratios, the plate structures grew on top of each other and thickened (see Figure 3.18(a,b,f,g)). Deformations and holes are formed on the products at higher concentrations of capping agents (up to 1×10^{-2} M). In addition to plates, Au nanostructures are formed in various shapes, such as rods, decahedrons, and truncated icosahedrons. At lower molar ratios, the products exhibit plate-like and truncated icosahedron morphology (see Figure 3.18(c-e,h-j)). When the capping agents CTAB and

PVP are added separately to the reaction medium, the highest average plate sizes are 16.5 ± 1.58 µm and 17.4 ± 0.64 µm, respectively (obtained at a 1 x 10^{-4} molar ratio of the capping agent to $HAuCl_4$). As a result, when PVP or CTAB is used as an additive in the reaction medium, the average size of the plates increases, which signifies the growth of the plates.

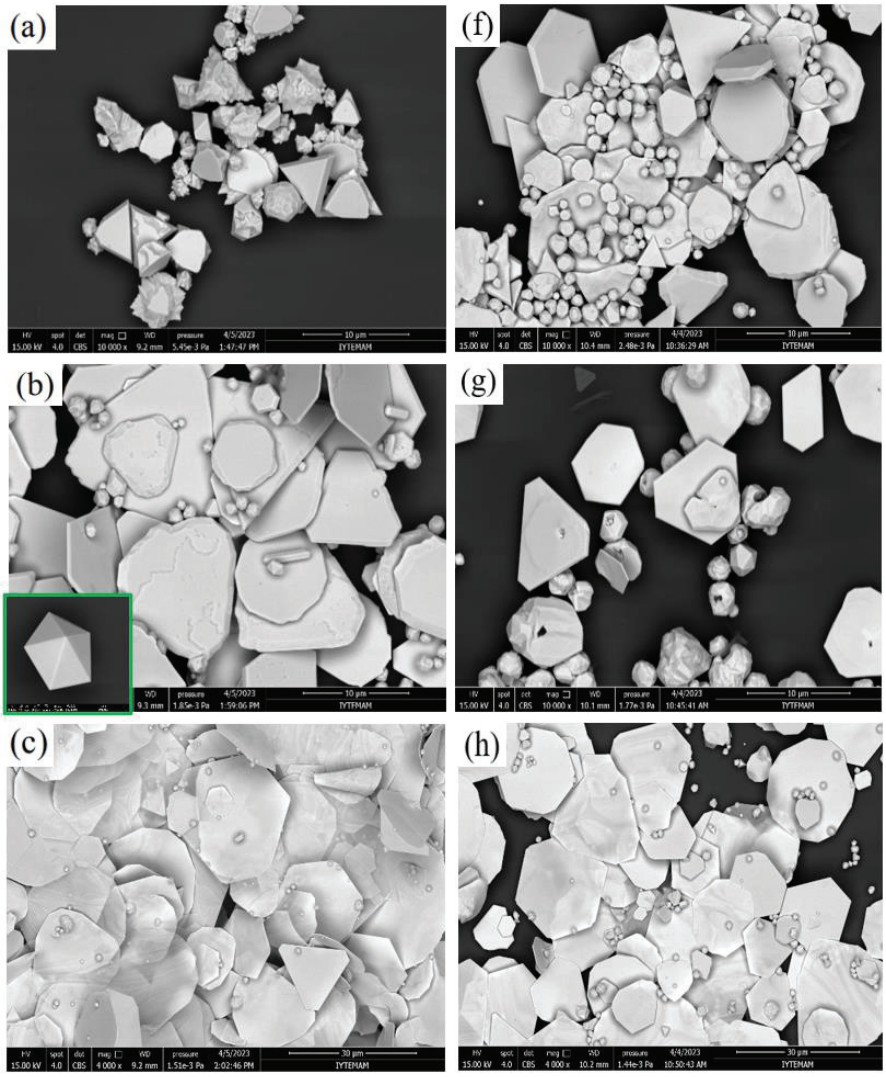

Figure 3.18. (a-e) SEM images of Au products obtained with different CTAB/$HAuCl_4$ molar ratios. (a) 1× 10^{-1}, (b) 1× 10^{-2}, (c) 1× 10^{-3}, (d) 1× 10^{-4}, and (e) 1× 10^{-5}. (f-j) SEM images of Au plates obtained with different PVP/$HAuCl_4$ molar ratios. (f) 1× 10^{-1}, (g) 1× 10^{-2}, (h) 1× 10^{-3}, (i) 1× 10^{-4}, and (j) 1× 10^{-5}.

(Figure cont. on next page)

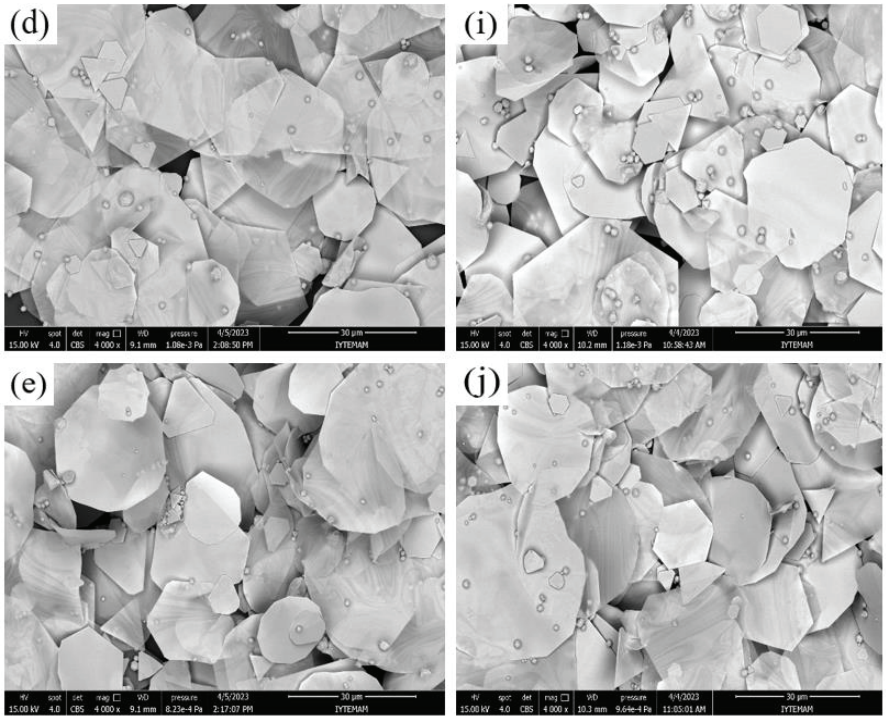

Figure 3.18 (cont.).

The effect of inorganic salts on Au plate formation was investigated by adding NaBr, KCl, NaCl, LiBr, and KI separately to the reaction medium. Here, the molar ratio of salt/$HAuCl_4$ is 1×10^{-3}. According to the SEM results shown in Figure 3.19, truncated icosahedron structures and anisotropic plate shapes are formed in the products. The addition of inorganic salts, especially NaBr and KCl, to the reaction medium promotes the growth of truncated icosahedron structures.

The gel-like sample was exposed to UV light instead of white light. The SEM image in Figure 3.20 shows the formation of reticulated Au products consisting of spherical and rod nanostructures by UV light photoreduction. Consequently, UV light irradiation (400 nm) favors the formation of spherical and rod nanostructures rather than 2D single-crystalline plates.

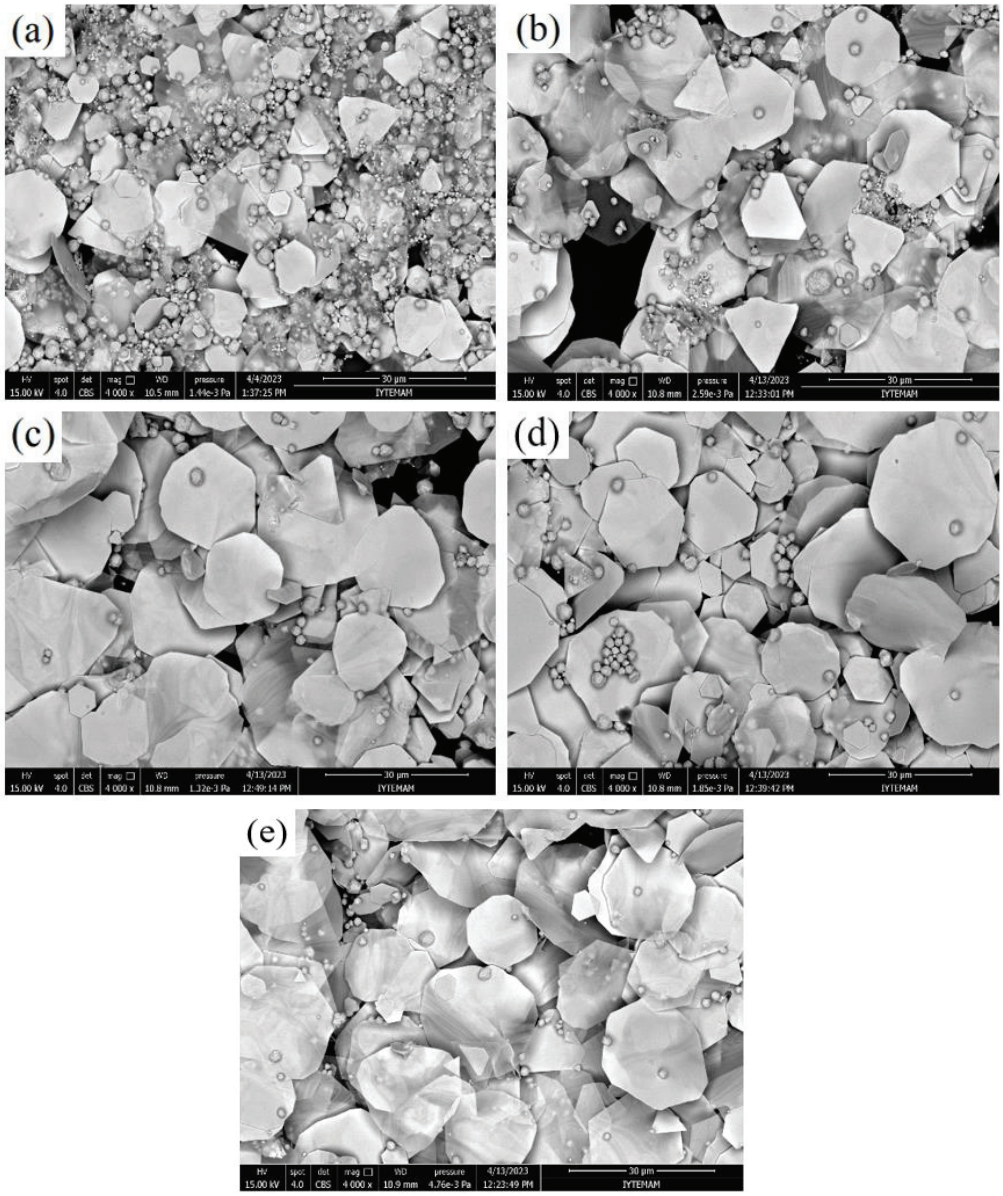

Figure 3.19. SEM images of Au products obtained with a 1×10^{-3} molar ratio of different inorganic salts to $HAuCl_4$. (a) NaBr, (b) KCl, (c) NaCl, (d) LiBr, and (e) KI.

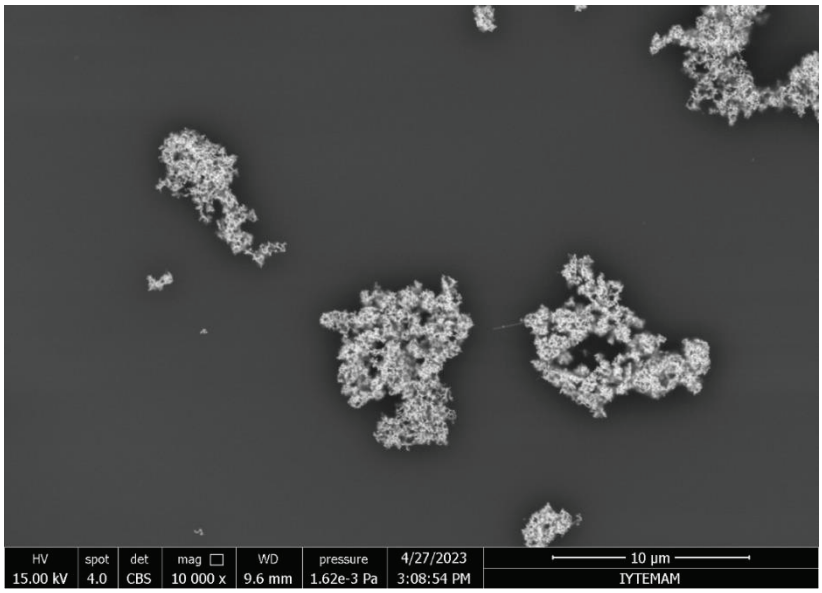

Figure 3.20. SEM images of Au products obtained by UV light irradiation.

3.2. Synthesis and Characterization of Reduced Graphene Oxide Thin Films Using Lyotropic Liquid Crystal

Graphene oxide (GO) was synthesized with 86% yield, as shown in Figure 3.21. In this GO synthesis, expensive membranes are not needed during purification, unlike Tour's method.[129] Cooling the acid solutions (H_2SO_4/H_3PO_4) at 5 °C before synthesis prevented the sudden increase in temperature during the exothermic reaction.[129] Particle aggregation on the thin film surface adversely affects the quality of the film. To prevent these particle aggregations on the surface of the films, attention was paid to homogeneously mixing the precursors added during the GO synthesis. The graphite-acid mixture was further homogenized in an ultrasonic bath and the particle size of $KMnO_4$ was reduced by grinding the solid in a mortar. At the end of the synthesis, a bright yellow solution was obtained as evidence of GO formation.

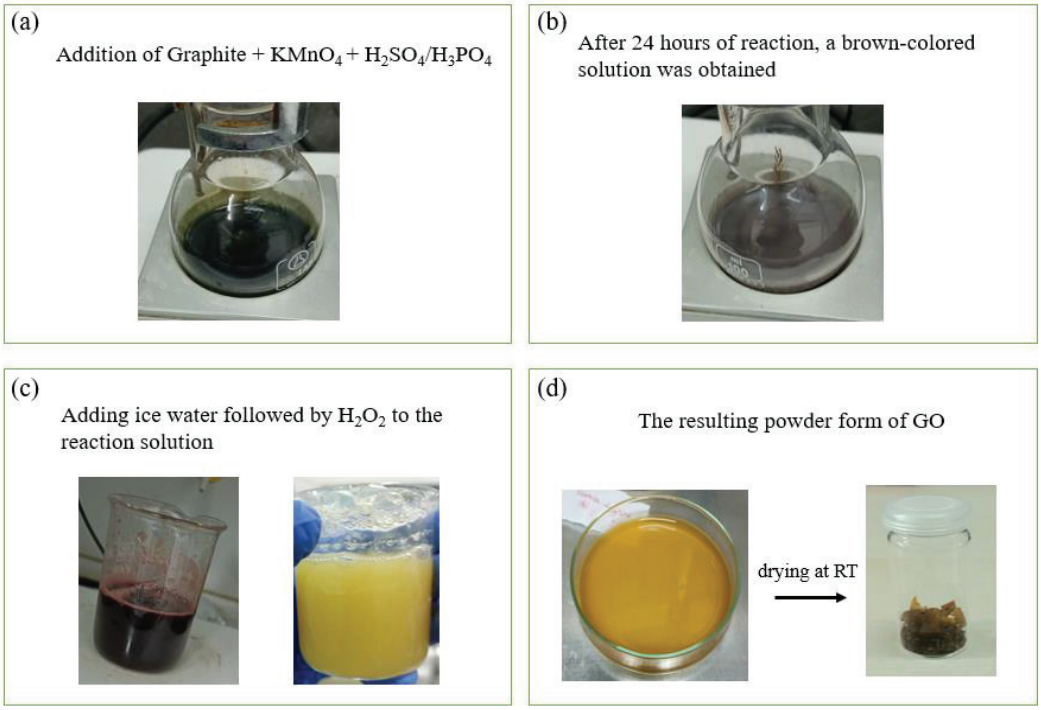

Figure 3.21. Reaction steps for GO synthesis.

Figure 3.22a shows the UV-Vis absorption spectrum of synthesized GO. A strong absorption peak is observed at about 228 nm, indicating the π–π* transition of the C=C bonds. The absorption shoulder is also found at nearly 306 nm, indicating the n–π*

transition of C=O bonds. The XRD patterns of pristine graphite and GO powders are shown in Figure 3.22b. Since pristine graphite is highly crystalline, it has a strong and sharp XRD peak at 2θ=26.5˚. With the oxidation of graphite, this strong peak disappears and a characteristic diffraction peak is observed at 2θ=9.3˚, denoting the formation of GO with hydrophilic functional groups.

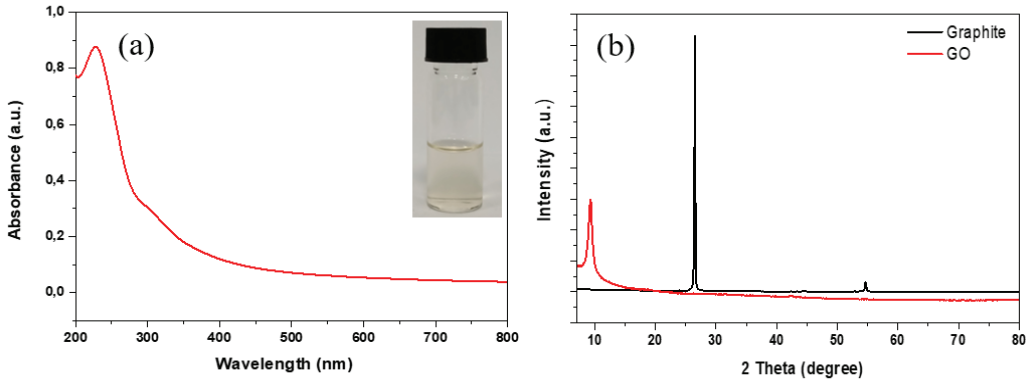

Figure 3.22. (a) UV-Vis spectrum of a 0.05 mg/ml GO aqueous solution. The inset photograph represents a 0.05 mg/ml GO solution in a vial. (b) XRD pattern of pristine graphite and GO powders.

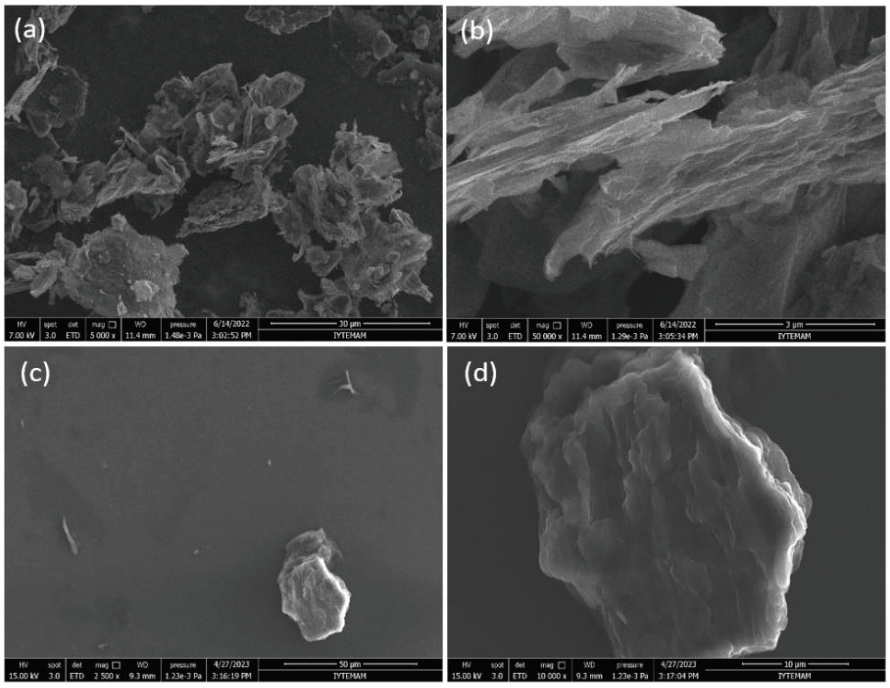

Figure 3.23. SEM images of graphite powder at (a) low and (b) high magnifications and spin-coated GO sample with a 1.0 mg/mL concentration at (c) low and (d) high magnifications.

The surface morphology of the graphite powder and the synthesized GO were obtained using SEM, as shown in Figure 3.23. Graphite flake has a layered structure formed by numerous thin sheets (see Figure 3.23(a,b)). On the other hand, GO has a morphology formed by the overlapping of numerous plate-like structures (see Figure 3.23(c,d)). Also, some thin and sheet-like structures are present in a folded form.

After the synthesis of GO was achieved, its aqueous solution was mixed with the LLC mesophase to produce the RGO thin films. The hexagonal mesophase of $SA/C_{12}EO_{10}$ was prepared at a 2.4 mole ratio. GO aqueous solution was prepared at five different concentrations, 2.5, 5, 10, 15, and 20 mg/mL. Each different concentration of GO was added to the LLC mesophase and allowed to stir overnight to obtain homogeneous clear solutions. Homogeneous LLC-GO solutions were then drop-casted onto the glass substrate and excess solvent was evaporated under atmospheric conditions. As seen from the POM images in Figure 3.24, the fan-like texture of the 2D hexagonal phase disappears as the GO concentration increases in the LLC mesophase. XRD analysis was also performed to identify the low-angle XRD pattern of these gel samples (see Figure 3.25). The 2.4 mole ratio of the fresh $SA/C_{12}E_{10}$ gel sample diffracts at a small angle of about 2˚, 2θ. However, the intensity of the XRD peak decreases with the addition of GO aqueous solution to the LLC mesophase. As evident from the POM images, the hexagonal phase of the gel samples is almost lost because the long-range order of the LC is distorted.

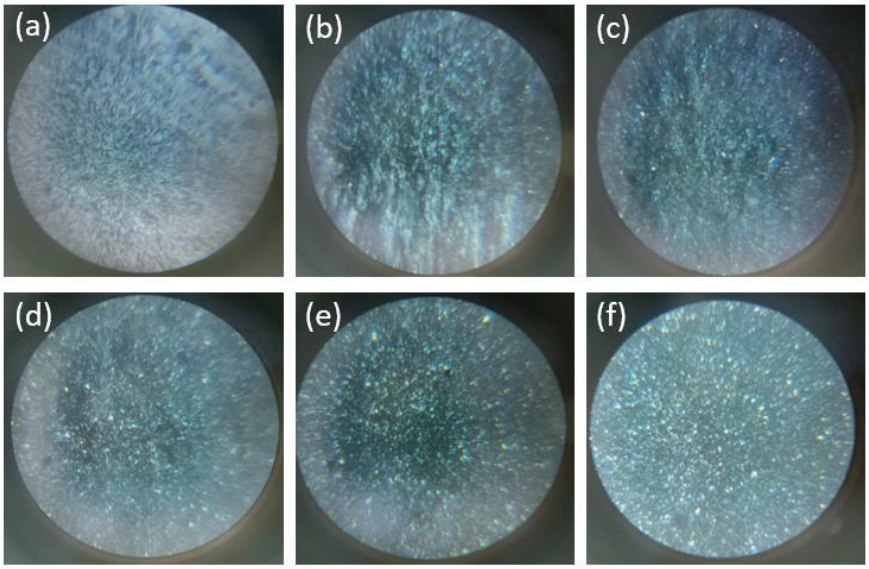

Figure 3.24. (a) POM textures of the SA/$C_{12}EO_{10}$ LLC mesophase. POM textures of the LLC mesophase containing GO solution with a concentration of (b) 2.5 mg/mL, (c) 5 mg/mL, (d) 10 mg/mL, (e) 15 mg/mL, and (f) 20 mg/mL. (These POM textures were obtained with a 10x optical lens.)

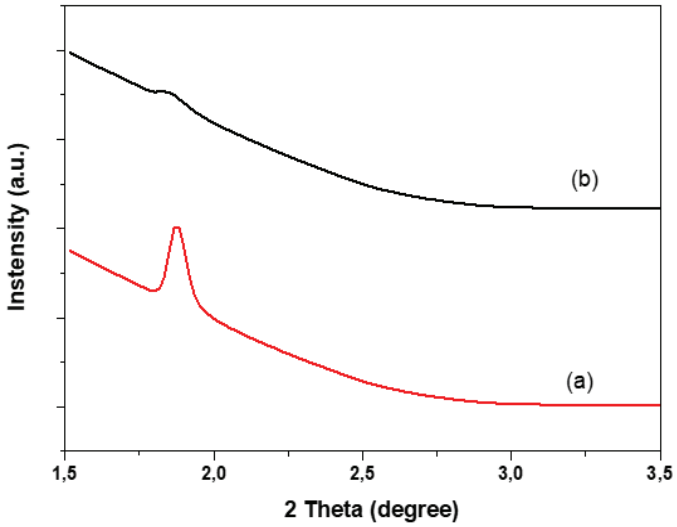

Figure 3.25. XRD pattern of (a) SA/$C_{12}EO_{10}$ and (b) SA/$C_{12}EO_{10}$/GO LLC mesophases.

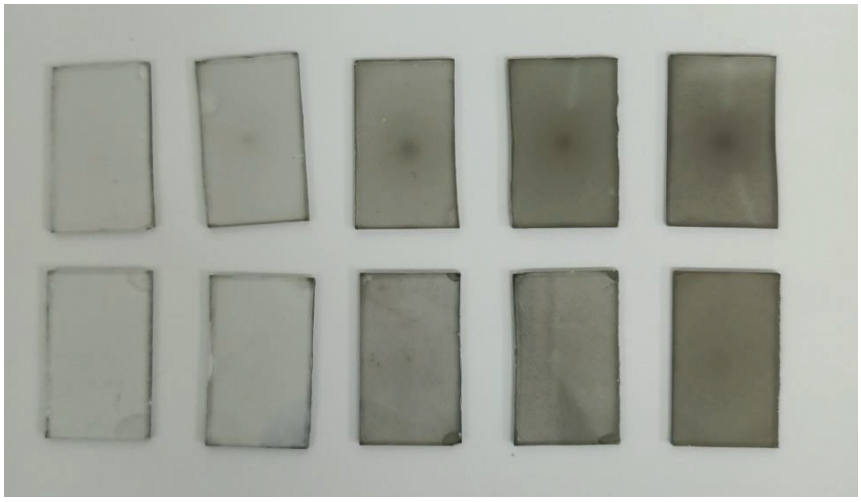

Figure 3.26. Photograph of RGO thin films obtained with the SA/$C_{12}EO_{10}$ LLC mesophase (top row) or without the LLC mesophase (bottom row). GO concentration increases from left to right. These thin films were obtained at 300 °C under atmospheric conditions.

The spin-coating method was applied at 2000 rpm for 1 min to produce thin films. Chemical reduction of L-ascorbic acid was then carried out at 80°C for 1 h. At the end of the reduction, the composition containing 2.5 mg/mL GO aqueous solution had a hexagonal fan-like texture under the POM. These films were subjected to thermal reduction at 300°C under an inert atmosphere (Ar) after being washed in ethanol overnight. This procedure was also applied to thin films produced without the LLC mesophase. Photograph of spin-coated RGO thin films on glass substrates are given in Figure 3.26. The GO solution is not uniformly distributed over the surface when the LLC mesophase is not used to produce the thin films.

Table 3.1. Sheet resistance and transmittance (at 550 nm) of RGO thin films prepared without the LLC mesophase.

GO (mg/mL)	Sheet Resistance (/sq)	Transmittance (%)
2.5	-	94
5	26 mΩ	89
10	0.34 mΩ	65
15	72 kΩ	55
20	25 kΩ	42

Table 3.2. Sheet resistance and transmittance (at 550 nm) of RGO thin films prepared with the LLC mesophase.

LLC + (mg/mL) GO	Sheet Resistance (/sq)	Transmittance (%)
2.5	2 mΩ	91
5	0.26 mΩ	81
10	50 kΩ	63
15	~20 kΩ	52
20	25 kΩ	30

RGO thin films with highly smooth surfaces obtained using the LLC mesophase are suitable for use as electrodes in electrochemical devices. Table 3.1 and Table 3.2 show the sheet resistance and transmittance values (at 550 nm) of RGO thin films. Optical transmittance spectra of spin-coated RGO films on glass substrates were recorded in the wavelength range from 300 to 1000 nm (see Figure 3.27). Generally, the sheet resistance of RGO thin films decreases when the GO solution is combined with the LLC mesophase.

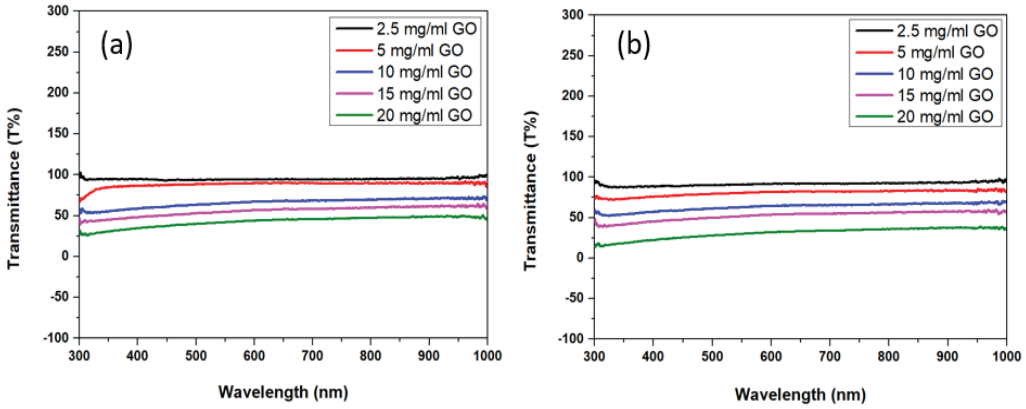

Figure 3.27. Optical transmittance spectra of spin-coated RGO films on glass substrate prepared (a) without and (b) with the LLC mesophase.

The sheet resistance reaches as low as 20 kΩ/sq at a transmittance of 52% (at 550 nm) with the composition containing LLC and 15 mg/mL GO concentration. For the same composition, the sheet resistance of the RGO thin films obtained without the LLC mesophase is almost four times this value (72 kΩ/sq). By further increasing the GO concentration, the same sheet resistance (25 kΩ/sq) is achieved in both conditions. The optical transparency of RGO thin films decreases in the presence of the LLC mesophase.

Surfactant molecules in the LLC composition undergo carbonization at high thermal annealing temperatures, thus reducing the transparency of the thin films. The relationship between the sheet resistance and optical transparency of RGO thin films containing LLC and different GO concentrations is given in Figure 3.28. RGO thin films of different compositions have a transmittance between 30% and 91% at 550 nm and a sheet resistivity between 2 mΩ/sq and 20 kΩ/sq.

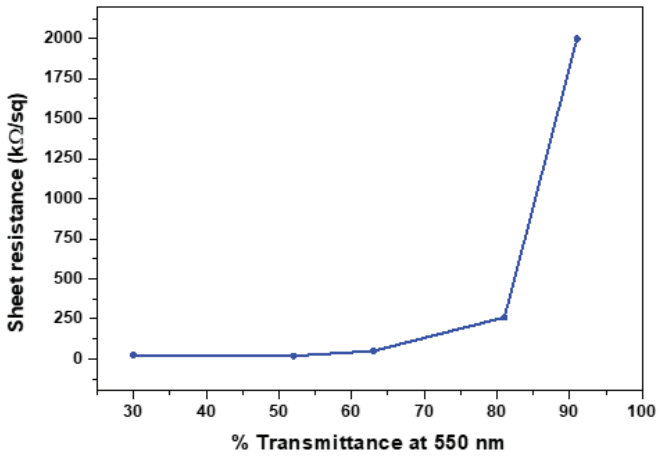

Figure 3.28. Sheet resistance as a function of transmittance for RGO thin films composed of LLC mesophase and GO solution.

The RGO thin film with a sheet resistance of 20 kΩ/sq and an optical transmittance of 52% was further characterized to prove the reduction of GO to RGO. RGO powder was obtained by scraping material from thin films for characterization. RGO formation was confirmed by the XRD peak detected at 25˚, as shown in Figure 3.29a. It has a broad and low-intensity XRD peak compared to graphite and GO, indicating that the crystal structure is disrupted due to the high annealing temperature. The ATR-FTIR spectra in Figure 3.29b show that the hydrophilic functional groups of GO are eliminated as a result of the thermal annealing process. O-H (3338 cm^{-1}), C=O (1733 cm^{-1}), C=C (1627 cm^{-1}), and C-O (1038 cm^{-1}) stretching vibrations characterize GO in the ATR-FTIR spectrum.[126,129]

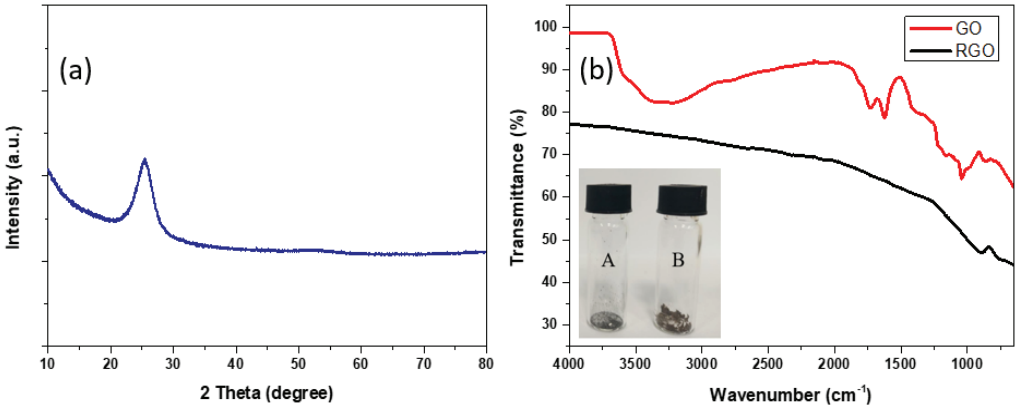

Figure 3.29. (a) XRD pattern of RGO powders. (b) ATR-FTIR spectra of GO (red) and RGO (black) powders. The inset shows the characterized RGO (marked A) and GO (marked B) powders.

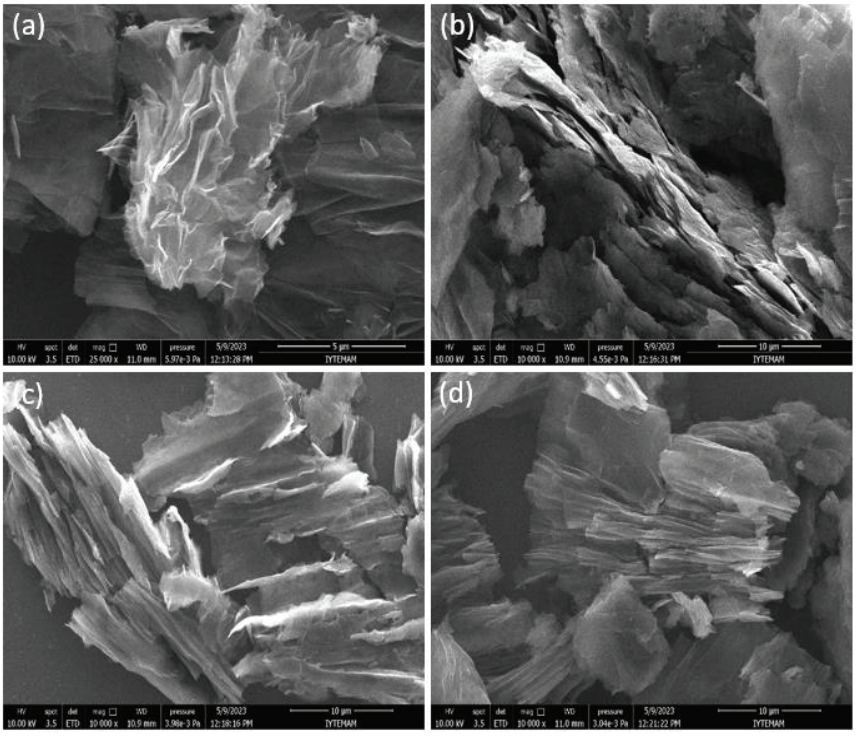

Figure 3.30. SEM images of RGO prepared from (a,b) SA/$C_{12}EO_{10}$/GO and (c,d) GO compositions.

The surface morphology of the synthesized RGO for both conditions (with or without LLC) was investigated through SEM, as shown in Figure 3.30. Wrinkle-like structures in SEM images indicate the formation of RGO sheets. SEM images of spin-coated RGO thin films on glass substrates are also given in Figure 3.31 and Figure 3.32. Crack formation is observed on the surface of RGO thin films that do not contain LLC

mesophase (see Figure 3.32). In both conditions, there are aggregated RGO sheets on the surface of the films. As the GO concentration increases, the films are more uniformly coated with the precursor, but the aggregations on the surface increases. As shown in Figure 3.33, these aggregates on the surface of the films consist of the wrinkled structures of the RGO sheets.

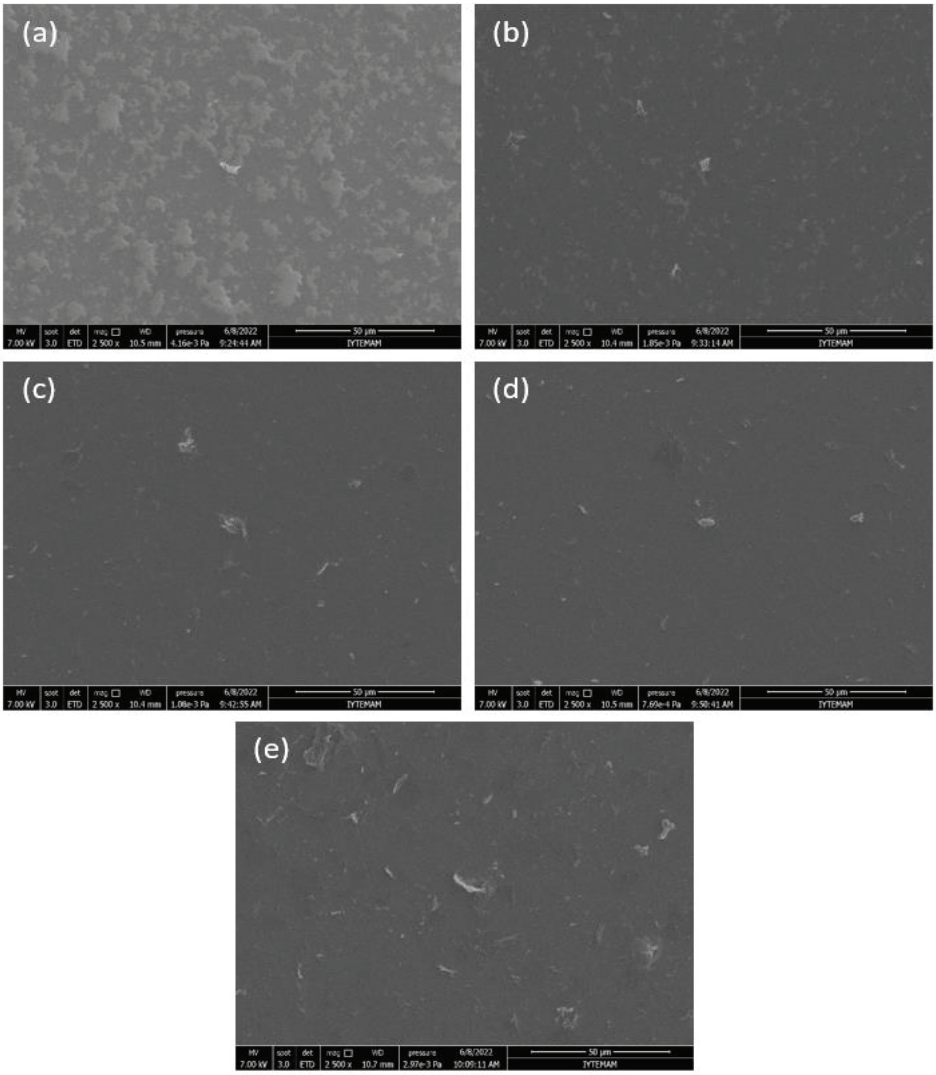

Figure 3.31. SEM images of the surfaces of spin-coated RGO thin films. RGO thin films containing LLC mesophase with different GO concentrations. (a) 2.5 mg/mL, (b) 5 mg/mL, (c) 10 mg/mL, (d) 15 mg/mL, and (e) 20 mg/mL.

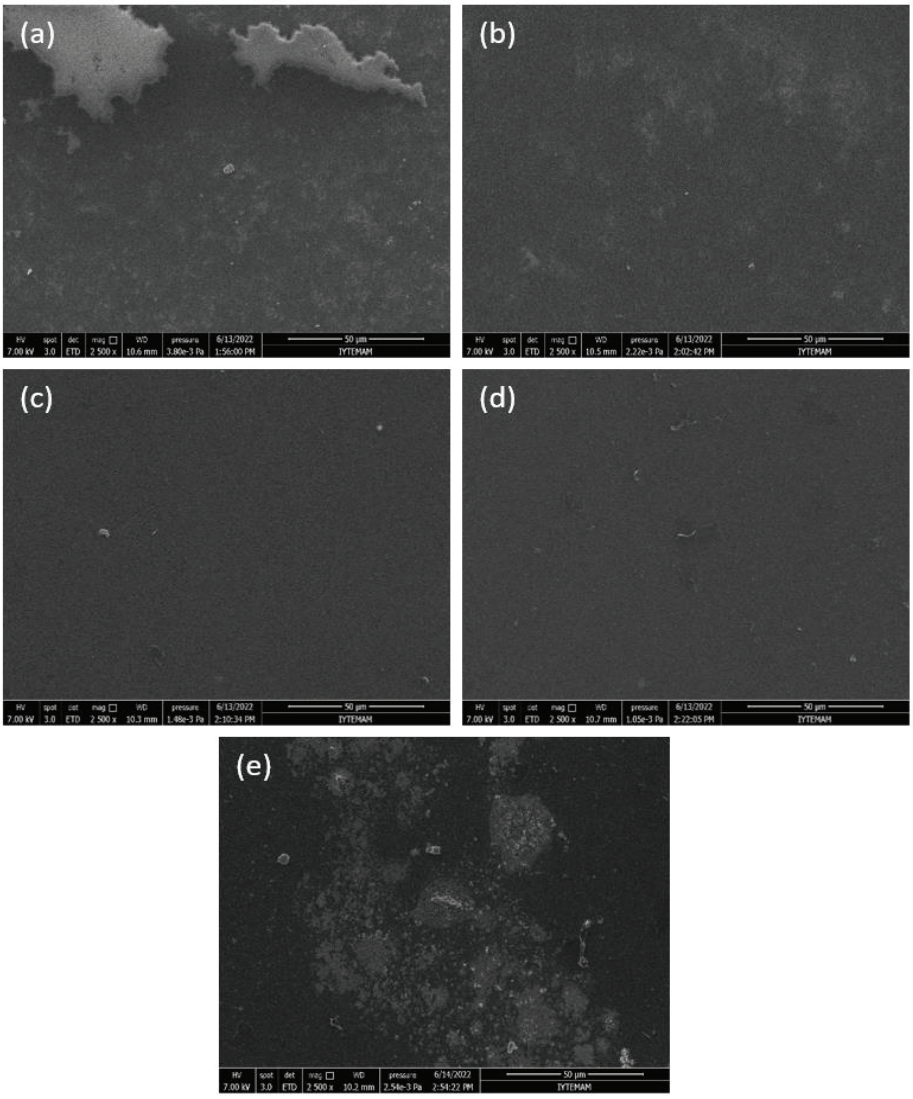

Figure 3.32. SEM images of the surfaces of spin-coated RGO thin films. RGO thin films obtained without the LLC mesophase and containing different concentrations of GO solutions. (a) 2.5 mg/mL, (b) 5 mg/mL, (c) 10 mg/mL, (d) 15 mg/mL, and (e) 20 mg/mL.

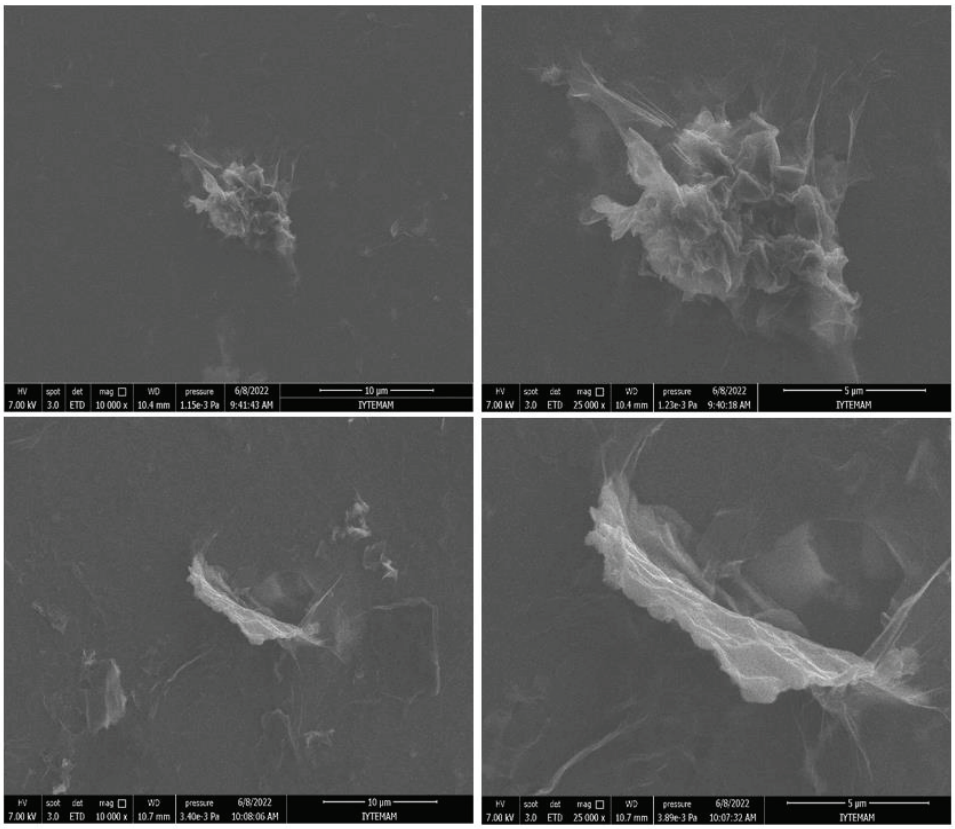

Figure 3.33. SEM images of the surfaces of spin-coated RGO thin films at low magnifications.

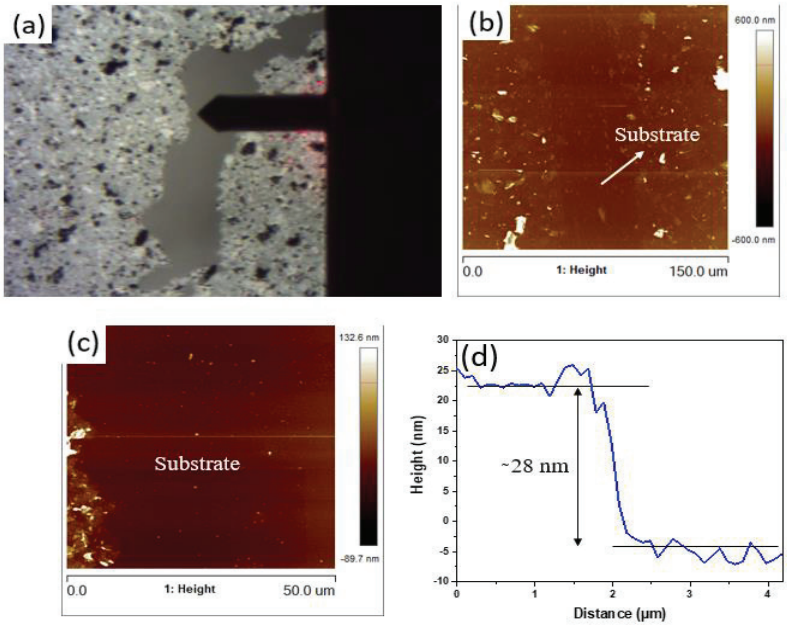

Figure 3.34. (a) Optical microscope image of spin-coated RGO thin film. (b,c) AFM images of RGO thin film at high and low magnifications. (d) AFM height profile of RGO thin film.

The thickness of the RGO thin film was investigated with the ScanAsyst mode of AFM (see Figure 3.34). As seen from the optical microscope image in Figure 3.34a, the film was scratched without damaging the substrate to determine the thickness of the thin film. The spin-coated RGO thin film has a thickness of approximately 28 nm, as seen from the AFM images and height profiles in Figure 3.34(b-d).

Table 3.3. Sheet resistance and transmittance values (at 550 nm) of RGO thin films obtained from a 15 mg/mL GO aqueous solution at different rpms.

Rpm	Sheet Resistance (/sq)	Transmittance (%)
1000	55 kΩ	48
1500	0.17 mΩ	57
2000	0.23 mΩ	56
2500	0.34 mΩ	59
3000	0.35 mΩ	56
3500	0.30 mΩ	57
4000	0.15 mΩ	56
4500	0.25 mΩ	56
5000	0.35 mΩ	58

Table 3.4. Sheet resistance and transmittance values (at 550 nm) of RGO thin films obtained from a solution containing 15 mg/mL GO and LLC at different rpms.

Rpm	Sheet Resistance (/sq)	Transmittance (%)
1000	13 kΩ	29
1500	22 kΩ	42
2000	20 kΩ	50
2500	25 kΩ	48
3000	26 kΩ	50
3500	26 kΩ	50
4000	27.5 kΩ	48
4500	29 kΩ	49
5000	27.5 kΩ	50

The sheet resistance and optical transmittance of RGO thin films produced with a high concentration of GO aqueous solution (15 mg/mL) at various rpms are shown in Table 3.3 and Table 3.4. Nine different rpm parameters, 1000, 1500, 2000, 2500, 3000, 3500, 4000, 4500, and 5000, were applied for 1 min with the spin-coating method. Optical

transmittance spectra of spin-coated RGO films on glass substrates were plotted in the wavelength range from 400 nm to 800 nm (see Figure 3.35). RGO films produced with 1000 rpm could not form a homogeneous surface due to excessive aggregation on the film surface. The sheet resistance of RGO thin films obtained without the LLC mesophase deviates more at different rpms because a homogeneous film surface cannot be obtained with this composition. As the rpm increases, the material on the substrate becomes thinner, and therefore the sheet resistance should increase.

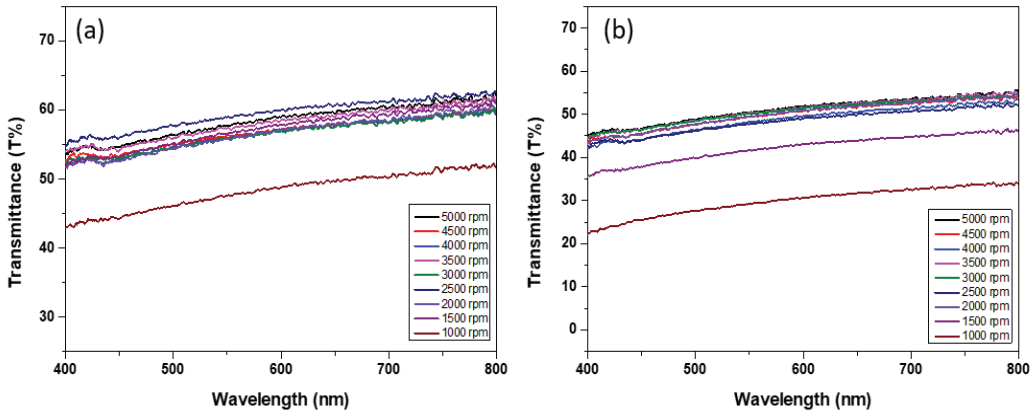

Figure 3.35. Optical transmittance spectra of spin-coated RGO thin films on glass substrate obtained from a solution containing (a) 15 mg/mL GO and (b) 15 mg/mL GO and LLC at different rpms.

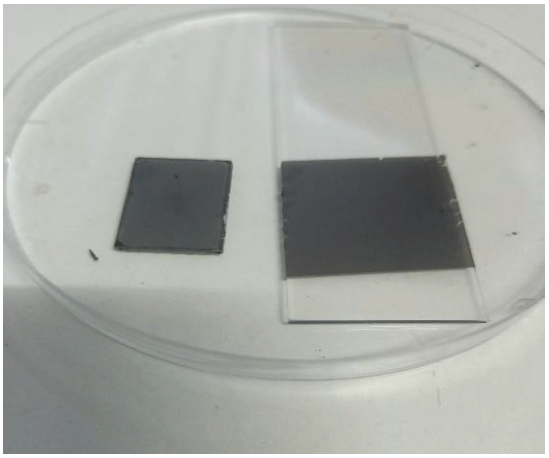

Figure 3.36. Photograph of thermally reduced spin-coated RGO (left) and CVD-based multilayer graphene (right).

Spin-coated RGO films were subjected to higher thermal annealing temperatures for 30 min under an inert atmosphere with Ar and H_2 to improve sheet resistance (see Figure 3.36). The annealing temperature was first applied to spin-coated thin films on quartz substrates at 850°C. Sheet resistance values for RGO thin films obtained with and without LLC mesophase were recorded as 23 kΩ/sq and 7 kΩ/sq, respectively. When the annealing time was extended to 1 h, there was not much change in the sheet resistance values. Moreover, the sheet resistance of the RGO thin films was further improved by increasing the annealing temperature to 1000°C. Then, the sheet resistance of the RGO thin film containing the LLC mesophase decreased to 17 kΩ/sq. On the other hand, the RGO thin film obtained without the LLC mesophase reached 5 kΩ/sq.

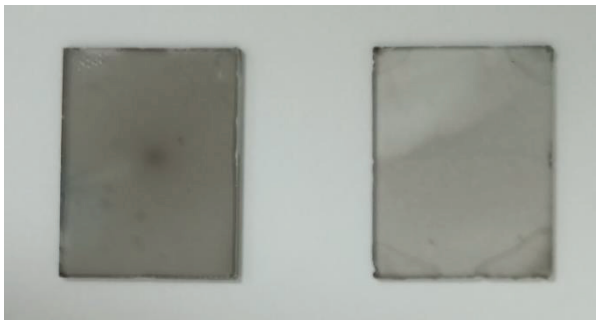

Figure 3.37. Photograph of spin-coated RGO thin films composed of a 2.5 mg/mL GO aqueous solution with (left) and without (right) the LLC mesophase. These thin films were obtained at 1000°C for 30 min under Ar and H_2.

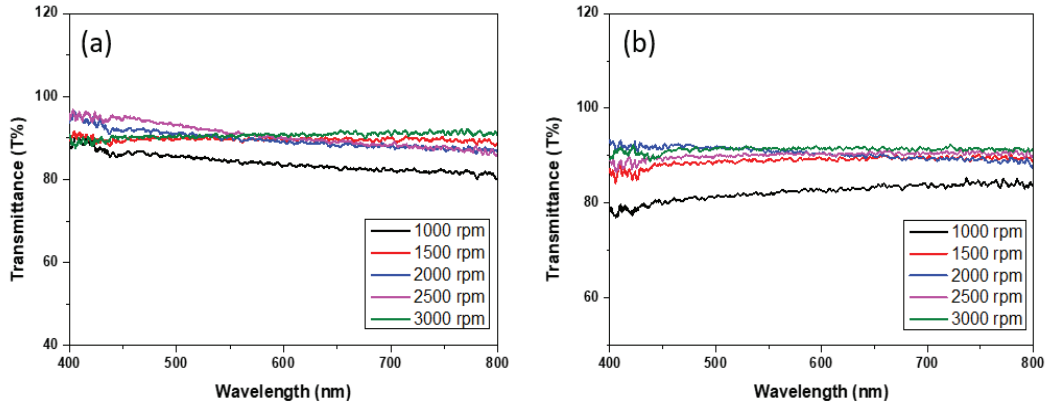

Figure 3.38. Optical transmittance spectra of spin-coated RGO thin films on quartz substrate obtained from a solution containing (a) 2.5 mg/mL GO and (b) 2.5 mg/mL GO and LLC at different rpms.

The sheet resistance of the RGO film produced with a low concentration of GO aqueous solution (2.5 mg/ml) was further improved for use as a transparent conductive electrode. Thermal annealing of the RGO thin film was carried out at 1000°C for 30 min under an inert atmosphere (Ar and H_2) (see Figure 3.37). Optical transmittance spectra of spin-coated RGO films on quartz substrates were plotted, as shown in Figure 3.38. When the thermal annealing temperature was increased to 1000°C, the RGO thin films obtained without the LLC mesophase became conductive (see Table 3.5). Furthermore, the sheet resistance values decreased to kΩ's in thin films containing LLC mesophase (see Table 3.6). As a result, RGO thin films with a sheet resistance of 31 kΩ/sq and a transmittance of 92% were prepared to be used as transparent and conductive electrodes.

Table 3.5. Sheet resistance and transmittance values (at 550 nm) of RGO thin films obtained from a 2.5 mg/mL GO aqueous solution at different rpms.

Rpm	Sheet Resistance (/sq)	Transmittance (%)
1000	55 kΩ	84
1500	54 kΩ	90
2000	67 mΩ	90
2500	2.1 mΩ	91
3000	0.23 mΩ	91

Table 3.6. Sheet resistance and transmittance values (at 550 nm) of RGO thin films obtained from a solution containing 2.5 mg/mL GO and LLC at different rpms.

Rpm	Sheet Resistance (/sq)	Transmittance (%)
1000	30 kΩ	82
1500	32 kΩ	90
2000	31 kΩ	92
2500	40 kΩ	88
3000	0.23 mΩ	93

CHAPTER 4

CONCLUSION

In this thesis, an LLC system consisting of 10-lauryl ether ($C_{12}EO_{10}$) and sulfuric acid (H_2SO_4, SA) was used to synthesize 2D single-crystalline gold (Au) nano- and microplates and reduced graphene oxide (RGO) thin films. As the SA/$C_{12}EO_{10}$ mole ratio increases in this system, a mesophase transition from bicontinuous cubic (V_1) to 2D-hexagonal (H_1) and micellar cubic (I_1) is observed. The 2D hexagonal (H_1) mesophase of the SA/$C_{12}EO_{10}$ system was characterized using POM and XRD.

For the first time, 2D single-crystalline Au plates have been synthesized using a photochemical approach in an LLC medium that is stable under atmospheric conditions. The stability of the LLC mesophase in atmospheric conditions facilitates the direct characterization of micrometer-sized Au plates under the optical microscope. The LLC medium provides an ordered confining space for the growth of micrometer-sized Au plate structures. The product contains a small amount of isotropic truncated icosahedron structures and various anisotropic shapes, such as triangular, truncated triangular, hexagonal, and gear-like. Irradiation of SA/$C_{12}EO_{10}$/$HAuCl_4$ LLC mesophase was achieved with different white light powers. The morphology and size of the Au products change according to the powers of the white light. Middle power light irradiation allows the synthesis of highly efficient plate-like structures with an average size of 12.5 ± 0.81 μm. The thickness of the Au plates ranges from 50 nm to 150 nm. Uniform spherical Au nanoparticles with a diameter of 142 ± 2.73 nm are synthesized by high power irradiation of white light. Plates with an average size of 4.65 ± 0.63 μm and truncated icosahedron structures are the main products in the low power light irradiation synthesis. At relatively low $HAuCl_4$ concentrations, the plates are embedded with spherical nanoparticles. At relatively high concentrations of $HAuCl_4$, the hexagonal phase of LLC disappears and plates are formed with highly efficient truncated icosahedron structures. As the $HAuCl_4$ concentration increases, the thickness of some Au plates in the products also increases, reaching about 420 nm. Adding PVP or CTAB to the reaction medium increases the average size of the Au plates from 10 μm to nearly 17 μm. Furthermore, the addition of inorganic salts can promote the formation of isotropic Au structures.

According to the reaction mechanism studied, isotropic and anisotropic Au nanoparticles grow into micrometer-sized Au plates as the reaction time increases. In the absence of white light irradiation, plate formation takes more than a week to occur with sufficient efficiency. However, without using white light, Au plates have smoother and sharper edges. Also, their average size becomes 19.8 ± 0.63 μm.

Transparent conductive RGO thin films have been prepared for the first time using the SA/$C_{12}EO_{10}$ LLC mesophase. GO was synthesized in 86% yield and characterized by XRD, UV-Vis spectroscopy, SEM, and ATR-FTIR spectroscopy. RGO thin films were prepared by a spin-coating method on a glass and/or quartz substrate at various spinning speeds. L-ascorbic acid, a weak and green reducing agent, was used for the chemical reduction of thin films. Thermal annealing was first performed at 300°C under an inert Argon (Ar) atmosphere and in a vacuum. RGO thin films with improved sheet resistance are achieved when the GO concentration is increased to 15 mg/mL. However, the optical transmittance of spin-coated RGO thin films decreases with increasing GO concentration. The sheet resistance of the RGO thin films has been further improved with the LLC mesophase. When the LLC system is used, the sheet resistance of the RGO thin film decreases from 72 kΩ/sq to 20 kΩ/sq. Moreover, the sheet resistance is reduced to 17 kΩ/sq at a higher annealing temperature (1000°C) under an inert atmosphere with Ar and H_2. More importantly, RGO thin films having low GO concentration have been improved to produce transparent conductive electrodes. Consequently, RGO thin films have been obtained with a sheet resistance of 31 kΩ/sq and an optical transmittance of 92% (at 550 nm) at 1000°C in an Ar + H_2 atmosphere.

REFERENCES

(1) Collings, P. J.; Hird, M. *Introduction to Liquid Crystals: Chemistry and Physics*; Taylor & Francis, **1997**.

(2) Reinitzer, F. Beiträge Zur Kenntniss Des Cholesterins. *Monatshefte für Chemie und verwandte Teile anderer Wissenschaften* **1888**, *9* (1), 421–441. https://doi.org/10.1007/BF01516710.

(3) Lehmann, O. Über Fliessende Krystalle. *Zeitschrift für Physikalische Chemie* **1889**, *4U* (1), 462–472. https://doi.org/doi:10.1515/zpch-1889-0434.

(4) Tsujii, K. *Surface Activity: Principles, Phenomena and Applications*; San Diego: Academic Press, **1998**; p 45.

(5) Tanford, C. Theory of Micelle Formation in Aqueous Solutions. *J Phys Chem* **1974**, *78* (24), 2469–2479.

(6) Tanford, C. Thermodynamics of Micelle Formation: Prediction of Micelle Size and Size Distribution. *Proceedings of the National Academy of Sciences* **1974**, *71* (5), 1811–1815.

(7) Tanford, C. *The Hydrophobic Effect: Formation of Micelles and Biological Membranes,* 2nd Edition; J. Wiley & Sons: New York, **1980**.

(8) Israelachvili, J. N.; Mitchell, D. J.; Ninham, B. W. Theory of Self-Assembly of Hydrocarbon Amphiphiles into Micelles and Bilayers. *Journal of the Chemical Society, Faraday Transactions 2: Molecular and Chemical Physics*. **1976**, pp 1525–1568. https://doi.org/10.1039/F29767201525.

(9) Israelachvili, J. N. *Intermolecular and Surface Forces*, 3rd Edition; Academic press, **2011**.

(10) Scholz, N.; Behnke, T.; Resch-Genger, U. Determination of the Critical Micelle Concentration of Neutral and Ionic Surfactants with Fluorometry, Conductometry, and Surface Tension—A Method Comparison. *J Fluoresc* **2018**, *28* (1), 465–476. https://doi.org/10.1007/s10895-018-2209-4.

(11) Myers, D. *Surfactant Science and Technology*, 3rd Edition; J. Wiley & Sons, Inc.: Hoboken, NJ, **2006**.

(12) Hamberger, A.; Landfester, K. Influence of Size and Functionality of Polymeric Nanoparticles on the Adsorption Behavior of Sodium Dodecyl Sulfate as Detected by Isothermal Titration Calorimetry. *Colloid Polym Sci* **2011**, *289* (1), 3–14. https://doi.org/10.1007/s00396-010-2318-3.

(13) An, J.-G.; Hina, S.; Yang, Y.; Xue, M.; Liu, Y. CHARACTERIZATION OF LIQUID CRYSTALS: A LITERATURE REVIEW. *Reviews on Advanced Materials Science* **2016**, *44* (4).

(14) Chavda, V. P.; Dawre, S.; Pandya, A.; Vora, L. K.; Modh, D. H.; Shah, V.; Dave, D. J.; Patravale, V. Lyotropic Liquid Crystals for Parenteral Drug Delivery. *Journal of Controlled Release*. Elsevier B.V. **2022**, pp 537–538. https://doi.org/10.1016/j.jconrel.2022.06.062.

(15) Hyde, S. T. Identification of Lyotropic Liquid Crystalline Mesophases. *Handbook of applied surface and colloid chemistry* **2001**, *2*, 299–332.

(16) Li, C.; He, J.; Liu, J.; Yu, Z.; Zhang, Q.; He, C.; Hong, W. Self-Assembly of Lyotropic Liquid Crystal Phases in Ternary Systems of 1,2-Dimethyl-3-Hexadecylimidazolium Bromide/1-Decanol/Water. *J Colloid Interface Sci* **2010**, *342* (2), 355–356. https://doi.org/10.1016/j.jcis.2009.10.067.

(17) Vallooran, J. J.; Bolisetty, S.; Mezzenga, R. Macroscopic Alignment of Lyotropic Liquid Crystals Using Magnetic Nanoparticles. *Advanced Materials* **2011**, *23* (34), 3932–3935. https://doi.org/10.1002/adma.201101760.

(18) Olutaş, E. B.; Balcı, F. M.; Dag, Ö. Strong Acid-Nonionic Surfactant Lyotropic Liquid-Crystalline Mesophases as Media for the Synthesis of Carbon Quantum Dots and Highly Proton Conducting Mesostructured Silica Thin Films and Monoliths. *Langmuir* **2015**, *31* (37), 10265–10271. https://doi.org/10.1021/acs.langmuir.5b02225.

(19) Feast, G. C.; Lepitre, T.; Tran, N.; Conn, C. E.; Hutt, O. E.; Mulet, X.; Drummond, C. J.; Savage, G. P. Inverse Hexagonal and Cubic Micellar Lyotropic Liquid Crystalline Phase Behaviour of Novel Double Chain Sugar-Based Amphiphiles. *Colloids Surf B Biointerfaces* **2017**, *151*, 35. https://doi.org/10.1016/j.colsurfb.2016.12.004.

(20) Hamley, I. W. *Introduction to Soft Matter: Synthetic and Biological Self-Assembling Materials*; John Wiley & Sons, **2007**.

(21) Van'T Hag, L.; Gras, S. L.; Conn, C. E.; Drummond, C. J. Lyotropic Liquid Crystal Engineering Moving beyond Binary Compositional Space-Ordered Nanostructured Amphiphile Self-Assembly Materials by Design. *Chemical Society Reviews*. Royal Society of Chemistry **2017**, pp 2708–2712. https://doi.org/10.1039/c6cs00663a.

(22) Mitchell, D. J.; Tiddy, G. J. T.; Waring, L.; Bostock, T.; McDonald, M. P. Phase Behaviour of Polyoxyethylene Surfactants with Water. Mesophase Structures and Partial Miscibility (Cloud Points). *Journal of the Chemical Society, Faraday Transactions 1: Physical Chemistry in Condensed Phases* **1983**, *79* (4), 975–1000.

(23) Huang, K. L.; Shigeta, K.; Kunieda, H. Phase Behavior of Polyoxyethylene Dodecyl Ether-Water Systems. *Trends in Colloid and Interface Science XII* **1998**, 171–174.

(24) Kunieda, H.; Shigeta, K.; Ozawa, K.; Suzuki, M. Self-Organizing Structures in Poly (Oxyethylene) Oleyl Ether− Water System. *J Phys Chem B* **1997**, *101* (40), 7952–7957.

(25) Seguin, C.; Eastoe, J.; Heenan, R. K.; Grillo, I. Controlling Aggregation of Nonionic Surfactants Using Mixed Glycol Media. *Langmuir* **2007**, *23* (8), 4199–4202. https://doi.org/10.1021/la063628h.

(26) Araos, M. U.; Warr, G. G. Self-Assembly of Nonionic Surfactants into Lyotropic Liquid Crystals in Ethylammonium Nitrate, a Room-Temperature Ionic Liquid. *Journal of Physical Chemistry B* **2005**, *109* (30), 14275–14277. https://doi.org/10.1021/jp052862y.

(27) Sandoval, T. E.; Gárate, M. P. Measurement of the Phase Behaviour of the Binary Systems {carbon Dioxide (CO_2) + Non-Ionic Surfactants (C_iEO_j)}. *Journal of Chemical Thermodynamics* **2012**, *45* (1), 109–113. https://doi.org/10.1016/j.jct.2011.09.018.

(28) Albayrak, C.; Ozkan, N.; Dag, O. Origin of Lyotropic Liquid Crystalline Mesophase Formation and Liquid Crystalline to Mesostructured Solid Transformation in the Metal Nitrate Salt− Surfactant Systems. *Langmuir* **2011**, *27* (3), 870–873.

(29) Çelik, Ö.; Dag, Ö. A New Lyotropic Liquid Crystalline System: Oligo (Ethylene Oxide) Surfactants with $[M(H_2O)_n]$ X_m Transition Metal Complexes. *Angewandte Chemie International Edition* **2001**, *40* (20), 3799–3803.

(30) Tunkara, E.; Albayrak, C.; Polat, E. O.; Kocabas, C.; Dag, O. Highly Proton Conductive Phosphoric Acid–Nonionic Surfactant Lyotropic Liquid Crystalline Mesophases and Application in Graphene Optical Modulators. *ACS Nano* **2014**, *8* (10), 11007–11012.

(31) Evans, H.; Tildesley, D. J.; Leng, C. A. Theories of Cloud-Curve Phase Separation in Non-Ionic Alkyl Polyoxyethylene Micellar Solutions. *Journal of the Chemical Society, Faraday Transactions 2: Molecular and Chemical Physics* **1987**, *83* (8), 1525–1526.

(32) Hofmeister, F. Zur Lehre von Der Wirkung Der Salze. *Archiv für experimentelle Pathologie und Pharmakologie* **1888**, *24* (4), 247–260. https://doi.org/10.1007/BF01918191.

(33) Kang, B.; Tang, H.; Zhao, Z.; Song, S. Hofmeister Series: Insights of Ion Specificity from Amphiphilic Assembly and Interface Property. *ACS Omega* **2020**, *5* (12), 6230.

(34) Inoue, T.; Yokoyama, Y.; Zheng, L.-Q. Hofmeister Anion Effect on Aqueous Phase Behavior of Heptaethylene Glycol Dodecyl Ether. *J Colloid Interface Sci* **2004**, *274* (1), 349–353.

(35) Zheng, L.; Minamikawa, H.; Harada, K.; Inoue, T.; Chernik, G. G. Effect of Inorganic Salts on the Phase Behavior of an Aqueous Mixture of Heptaethylene Glycol Dodecyl Ether. *Langmuir* **2003**, *19* (25), 10487–10494.

(36) Albayrak, C.; Soylu, A. M.; Dag, O. Lyotropic Liquid-Crystalline Mesophases of $[Zn(H_2O)_6](NO_3)_2$− $C_{12}EO_{10}$− CTAB− H_2O and $[Zn(H_2O)_6](NO_3)_2$− $C_{12}EO_{10}$− SDS− H_2O Systems. *Langmuir* **2008**, *24* (19), 10592–10595.

(37) Albayrak, C.; Cihaner, A.; Dag, Ö. A New, Highly Conductive, Lithium Salt/Nonionic Surfactant, Lyotropic Liquid-Crystalline Mesophase and Its Application. *Chemistry–A European Journal* **2012**, *18* (14), 4190–4194.

(38) Uzundal, C. B.; Mert Balci, F.; Ulgut, B.; Dag, O. Lyotropic Liquid Crystalline Mesophase of Sulfuric Acid–Nonionic Surfactant Stabilizes Lead (II) Oxide in Sulfuric Acid Concentrations Relevant to Lead Acid Batteries. *ACS Omega* **2017**, *2* (7), 3785–3791.

(39) Kresge, a C. T.; Leonowicz, M. E.; Roth, W. J.; Vartuli, J. C.; Beck, J. S. Ordered Mesoporous Molecular Sieves Synthesized by a Liquid-Crystal Template Mechanism. *Nature* **1992**, *359* (6397), 710–712.

(40) Beck, J. S.; Vartuli, J. C.; Roth, W. J.; Leonowicz, M. E.; Kresge, C. T.; Schmitt, K. D.; Chu, C. T. W.; Olson, D. H.; Sheppard, E. W.; McCullen, S. B. A New Family of Mesoporous Molecular Sieves Prepared with Liquid Crystal Templates. *J Am Chem Soc* **1992**, *114* (27), 10834–10843.

(41) Attard, G. S.; Glyde, J. C.; Göltner, C. G. Liquid-Crystalline Phases as Templates for the Synthesis of Mesoporous Silica. *Nature* **1995**, *378* (6555), 366–368.

(42) Soltani, S.; Khanian, N.; Rashid, U.; Choong, T. S. Y. Fundamentals and Recent Progress Relating to the Fabrication, Functionalization and Characterization of Mesostructured Materials Using Diverse Synthetic Methodologies. *RSC Adv* **2020**, *10* (28), 16433.

(43) Bruckner, J. R.; Bauhof, J.; Gebhardt, J.; Beurer, A.-K.; Traa, Y.; Giesselmann, F. Mechanisms and Intermediates in the True Liquid Crystal Templating Synthesis of Mesoporous Silica Materials. *J Phys Chem B* **2021**, *125* (12), 3197–3207.

(44) Attard, G. S.; Corker, J. M.; Göltner, C. G.; Henke, S.; Templer, R. H. Liquid-crystal Templates for Nanostructured Metals. *Angewandte Chemie International Edition in English* **1997**, *36* (12), 1315–1317.

(45) Yamauchi, Y.; Nair, S. S.; Momma, T.; Ohsuna, T.; Osaka, T.; Kuroda, K. Synthesis and Characterization of Mesoporous Pt–Ni (HI–Pt/Ni) Alloy Particles

Prepared from Lyotropic Liquid Crystalline Media. *J Mater Chem* **2006**, *16* (23), 2229–2234.

(46) Attard, G. S.; Leclerc, S. A. A.; Maniguet, S.; Russell, A. E.; Nandhakumar, I.; Bartlett, P. N. Mesoporous Pt/Ru Alloy from the Hexagonal Lyotropic Liquid Crystalline Phase of a Nonionic Surfactant. *Chemistry of materials* **2001**, *13* (5), 1444–1446.

(47) Attard, G. S.; Bartlett, P. N.; Coleman, N. R. B.; Elliott, J. M.; Owen, J. R.; Wang, J. H. Mesoporous Platinum Films from Lyotropic Liquid Crystalline Phases. *Science (1979)* **1997**, *278* (5339), 838–840.

(48) Bartlett, P. N.; Marwan, J. Preparation and Characterization of H1–e Rhodium Films. *Microporous and mesoporous materials* **2003**, *62* (1–2), 73–79.

(49) Zhao, D.-D.; Xu, M. W.; Zhou, W.-J.; Zhang, J.; Li, H. L. Preparation of Ordered Mesoporous Nickel Oxide Film Electrodes via Lyotropic Liquid Crystal Templated Electrodeposition Route. *Electrochim Acta* **2008**, *53* (6), 2699–2705.

(50) Nandhakumar, I.; Elliott, J. M.; Attard, G. S. Electrodeposition of Nanostructured Mesoporous Selenium Films (HI-ESe). *Chemistry of materials* **2001**, *13* (11), 3840–3842.

(51) Elliott, J. M.; Cabuché, L. M.; Bartlett, P. N. Electrochemical Characterization of a Templated Insulating Polymer-Modified Electrode. *Anal Chem* **2001**, *73* (13), 2855–2861.

(52) Shipway, A. N.; Katz, E.; Willner, I. Nanoparticle Arrays on Surfaces for Electronic, Optical, and Sensor Applications. *ChemPhysChem* **2000**, *1* (1), 18–52.

(53) Gong, S.; Cheng, W. One-dimensional Nanomaterials for Soft Electronics. *Adv Electron Mater* **2017**, *3* (3), 1600314.

(54) Hu, H.; Zhou, J.; Kong, Q.; Li, C. Two-Dimensional Au Nanocrystals: Shape/Size Controlling Synthesis, Morphologies, and Applications. *Particle & Particle Systems Characterization* **2015**, *32* (8), 802–805.

(55) Li, N.; Zhao, P.; Astruc, D. Anisotropic Gold Nanoparticles: Synthesis, Properties, Applications, and Toxicity. *Angewandte Chemie International Edition* **2014**, *53* (7), 1773–1780.

(56) Wang, C.; Chen, D.; Jiao, X. Lyotropic Liquid Crystal Directed Synthesis of Nanostructured Materials. *Sci Technol Adv Mater* **2009**, 9.

(57) Lee, M.-H.; Oh, S.-G.; Suh, K.-D.; Kim, D.-G.; Sohn, D. Preparation of Silver Nanoparticles in Hexagonal Phase Formed by Nonionic Triton X-100 Surfactant. *Colloids Surf A Physicochem Eng Asp* **2002**, *210* (1), 49–60.

(58) Qi, L.; Gao, Y.; Ma, J. Synthesis of Ribbons of Silver Nanoparticles in Lamellar Liquid Crystals. *Colloids Surf A Physicochem Eng Asp* **1999**, *157* (1–3), 285–294.

(59) Ding, J. H.; Gin, D. L. Catalytic Pd Nanoparticles Synthesized Using a Lyotropic Liquid Crystal Polymer Template. *Chemistry of materials* **2000**, *12* (1), 22–24.

(60) Dellinger, T. M.; Braun, P. V. Lyotropic Liquid Crystals as Nanoreactors for Nanoparticle Synthesis. *Chemistry of materials* **2004**, *16* (11), 2201–2207.

(61) Saliba, S.; Davidson, P.; Impéror-Clerc, M.; Mingotaud, C.; Kahn, M. L.; Marty, J.-D. Facile Direct Synthesis of ZnO Nanoparticles within Lyotropic Liquid Crystals: Towards Organized Hybrid Materials. *J Mater Chem* **2011**, *21* (45), 18191–18194.

(62) Zhang, X.; Shan, C.; Ma, S.; Zhao, S.; Yang, J. Synthesis of Nano-ZnS by Lyotropic Liquid Crystal Template Method for Enhanced Photodegradation of Methylene Blue. *Inorg Chem Commun* **2022**, *135*, 109089.

(63) Khiew, P. S.; Radiman, S.; Huang, N. M.; Ahamd, M. S. Synthesis and Characterization of Copper Sulfide Nanoparticles in Hexagonal Phase Lyotropic Liquid Crystal. *J Cryst Growth* **2004**, *268* (1–2), 227–237.

(64) Li, Y.; Wan, J.; Gu, Z. The Formation of Cadmium Sulfide Nanowires in Different Liquid Crystal Systems. *Materials Science and Engineering: A* **2000**, *286* (1), 106–109.

(65) Jiang, X.; Xie, Y.; Lu, J.; Zhu, L.; He, W.; Qian, Y. Simultaneous in Situ Formation of ZnS Nanowires in a Liquid Crystal Template by γ-Irradiation. *Chemistry of materials* **2001**, *13* (4), 1213–1218.

(66) Zhang, D.; Qi, L.; Cheng, H.; Ma, J. Preparation of ZnS Nanorods by a Liquid Crystal Template. *J Colloid Interface Sci* **2002**, *246* (2), 413–416.

(67) Kijima, T.; Yoshimura, T.; Uota, M.; Ikeda, T.; Fujikawa, D.; Mouri, S.; Uoyama, S. Noble-metal Nanotubes (Pt, Pd, Ag) from Lyotropic Mixed-surfactant Liquid-crystal Templates. *Angewandte Chemie International Edition* **2004**, *43* (2), 228–232.

(68) Wang, L.; Chen, X.; Zhan, J.; Sui, Z.; Zhao, J.; Sun, Z. Controllable Morphology Formation of Gold Nano-and Micro-Plates in Amphiphilic Block Copolymer-Based Liquid Crystalline Phase. *Chem Lett* **2004**, *33* (6), 720–721.

(69) Wang, L.; Chen, X.; Zhan, J.; Chai, Y.; Yang, C.; Xu, L.; Zhuang, W.; Jing, B. Synthesis of Gold Nano-and Microplates in Hexagonal Liquid Crystals. *J Phys Chem B* **2005**, *109* (8), 3189–3194.

(70) Kijima, T.; Nagatomo, Y.; Takemoto, H.; Uota, M.; Fujikawa, D.; Sekiya, Y.; Kishishita, T.; Shimoda, M.; Yoshimura, T.; Kawasaki, H. Synthesis of Nanohole-Structured Single-Crystalline Platinum Nanosheets Using Surfactant-Liquid-

Crystals and Their Electrochemical Characterization. *Adv Funct Mater* **2009**, *19* (4), 545–553.

(71) Sakai, G.; Yoshimura, T.; Isohata, S.; Uota, M.; Kawasaki, H.; Kuwahara, T.; Fujikawa, D.; Kijima, T. Synthesis of Nanogroove-Network-Structured Platinum Nanosheets and Their Carbon-Supported Forms Using a Mixed-Surfactant Templating Approach. *Advanced Materials* **2007**, *19* (2), 237–241.

(72) Ye, S.; Connell, S. D.; McLaughlan, J. R.; Roach, L.; Aslam, Z.; Chankhunthod, N.; Brown, A. P.; Brydson, R.; Bushby, R. J.; Critchley, K. One-Step Preparation of Biocompatible Gold Nanoplates with Controlled Thickness and Adjustable Optical Properties for Plasmon-Based Applications. *Adv Funct Mater* **2020**, *30* (40), 2003512.

(73) Morsin, M.; Nafisah, S.; Sanudin, R.; Razali, N. L.; Mahmud, F.; Soon, C. F. The Role of Positively Charge Poly-L-Lysine in the Formation of High Yield Gold Nanoplates on the Surface for Plasmonic Sensing Application. *PLoS One* **2021**, *16* (11), e0259730.

(74) Liu, Y.; Yang, L.; Shen, Y. Hydrothermal Synthesis of Gold Nanoplates and Their Structure-Dependent LSPR Properties. *J Mater Res* **2018**, *33* (18), 2671–2679.

(75) Chen, S.; Xu, P.; Li, Y.; Xue, J.; Han, S.; Ou, W.; Li, L.; Ni, W. Rapid Seedless Synthesis of Gold Nanoplates with Microscaled Edge Length in a High Yield and Their Application in SERS. *Nanomicro Lett* **2016**, *8*, 328–335.

(76) Kaur, P.; Chudasama, B. Single Step Synthesis of Pluronic Stabilized IR Responsive Gold Nanoplates. *RSC Adv* **2014**, *4* (68), 36006–36011.

(77) Tsuji, M.; Hashimoto, M.; Nishizawa, Y.; Tsuji, T. Preparation of Gold Nanoplates by a Microwave-Polyol Method. *Chem Lett* **2003**, *32* (12), 1114–1115.

(78) Sun, X.; Dong, S.; Wang, E. Large-scale Synthesis of Micrometer-scale Single-crystalline Au Plates of Nanometer Thickness by a Wet-chemical Route. *Angewandte Chemie International Edition* **2004**, *43* (46), 6360–6363.

(79) Sun, X.; Dong, S.; Wang, E. High-Yield Synthesis of Large Single-Crystalline Gold Nanoplates through a Polyamine Process. *Langmuir* **2005**, *21* (10), 4710–4712. https://doi.org/10.1021/la047267m.

(80) Porel, S.; Singh, S.; Radhakrishnan, T. P. Polygonal Gold Nanoplates in a Polymer Matrix. *Chem. Commun.* **2005**, No. 18, 2387–2389. https://doi.org/10.1039/B500536A.

(81) Lim, B.; Camargo, P. H. C.; Xia, Y. Mechanistic Study of the Synthesis of Au Nanotadpoles, Nanokites, and Microplates by Reducing Aqueous HAuCl4 with Poly(Vinyl Pyrrolidone). *Langmuir* **2008**, *24* (18), 10437–10442. https://doi.org/10.1021/la801803z.

(82) Yamamoto, M.; Kashiwagi, Y.; Sakata, T.; Mori, H.; Nakamoto, M. Synthesis and Morphology of Star-Shaped Gold Nanoplates Protected by Poly(N-Vinyl-2-Pyrrolidone). *Chemistry of Materials* **2005**, *17* (22), 5391–5393. https://doi.org/10.1021/cm0515000.

(83) Ah, C. S.; Yun, Y. J.; Park, H. J.; Kim, W.-J.; Ha, D. H.; Yun, W. S. Size-Controlled Synthesis of Machinable Single Crystalline Gold Nanoplates. *Chemistry of Materials* **2005**, *17* (22), 5558–5561. https://doi.org/10.1021/cm051225h.

(84) Chu, H.-C.; Kuo, C.-H.; Huang, M. H. Thermal Aqueous Solution Approach for the Synthesis of Triangular and Hexagonal Gold Nanoplates with Three Different Size Ranges. *Inorg Chem* **2006**, *45* (2), 808–813. https://doi.org/10.1021/ic051758s.

(85) Huang, W.-L.; Chen, C.-H.; Huang, M. H. Investigation of the Growth Process of Gold Nanoplates Formed by Thermal Aqueous Solution Approach and the Synthesis of Ultra-Small Gold Nanoplates. *The Journal of Physical Chemistry C* **2007**, *111* (6), 2533–2538.

(86) Lee, J.-H.; Kamada, K.; Enomoto, N.; Hojo, J. Polyhedral Gold Nanoplate: High Fraction Synthesis of Two-Dimensional Nanoparticles through Rapid Heating Process. *Cryst Growth Des* **2008**, *8* (8), 2638–2645. https://doi.org/10.1021/cg0702075.

(87) Luo, Y. Large-Scale Preparation of Single-Crystalline Gold Nanoplates. *Mater Lett* **2007**, *61* (6), 1346–1349. https://doi.org/https://doi.org/10.1016/j.matlet.2006.07.048.

(88) Bai, X.; Zheng, L.; Li, N.; Dong, B.; Liu, H. Synthesis and Characterization of Microscale Gold Nanoplates Using Langmuir Monolayers of Long-Chain Ionic Liquid. *Cryst Growth Des* **2008**, *8* (10), 3840–3846. https://doi.org/10.1021/cg800549e.

(89) Xie, J.; Lee, J. Y.; Wang, D. I. C. Synthesis of Single-Crystalline Gold Nanoplates in Aqueous Solutions through Biomineralization by Serum Albumin Protein. *The Journal of Physical Chemistry C* **2007**, *111* (28), 10226–10232. https://doi.org/10.1021/jp0719715.

(90) Zhang, Y.; Chang, G.; Liu, S.; Lu, W.; Tian, J.; Sun, X. A New Preparation of Au Nanoplates and Their Application for Glucose Sensing. *Biosens Bioelectron* **2011**, *28* (1), 344–348. https://doi.org/https://doi.org/10.1016/j.bios.2011.07.041.

(91) Ogi, T.; Saitoh, N.; Nomura, T.; Konishi, Y. Room-Temperature Synthesis of Gold Nanoparticles and Nanoplates Using Shewanella Algae Cell Extract. *Journal of Nanoparticle Research* **2010**, *12* (7), 2531–2539. https://doi.org/10.1007/s11051-009-9822-8.

(92) Yang, Z.; Li, Z.; Lu, X.; He, F.; Zhu, X.; Ma, Y.; He, R.; Gao, F.; Ni, W.; Yi, Y. Controllable Biosynthesis and Properties of Gold Nanoplates Using Yeast Extract. *Nanomicro Lett* **2017**, *9*, 1–13.

(93) Zhang, L.; Zhang, P.; Wu, R.; Han, A.; Cheng, K.; Wang, Z.; Yang, J.; Hou, S.; Tong, Y.; Dong, M. Amyloid Fibrils with Charge Transportation Facilitating the Green Synthesis of Single-Crystalline Gold Nanoplates for Catalytic Application. *Appl Surf Sci* **2023**, 156937.

(94) Huang, Y.; Ferhan, A. R.; Gao, Y.; Dandapat, A.; Kim, D.-H. High-Yield Synthesis of Triangular Gold Nanoplates with Improved Shape Uniformity, Tunable Edge Length and Thickness. *Nanoscale* **2014**, *6* (12), 6496–6500.

(95) Qiao, Z.; Wei, X.; Liu, H.; Liu, K.; Gao, C. Seed-Mediated Synthesis of Thin Gold Nanoplates with Tunable Edge Lengths and Optical Properties. *Nanomaterials* **2023**, *13* (4). https://doi.org/10.3390/nano13040711.

(96) Zhu, J.; Jin, X. Electrochemical Synthesis of Gold Triangular Nanoplates and Self-Organized into Rhombic Nanostructures. *Superlattices Microstruct* **2007**, *41* (4), 271–276.

(97) Cha, S.-H.; Kim, J.-U.; Kim, K.-H.; Lee, J.-C. Preparation of Gold Nanosheets Using Poly (Ethylene Oxide)–Poly (Propylene Oxide)–Poly (Ethylene Oxide) Block Copolymers via Photoreduction. *Materials Science and Engineering: B* **2007**, *140* (3), 182–186.

(98) Pienpinijtham, P.; Han, X. X.; Suzuki, T.; Thammacharoen, C.; Ekgasit, S.; Ozaki, Y. Micrometer-Sized Gold Nanoplates: Starch-Mediated Photochemical Reduction Synthesis and Possibility of Application to Tip-Enhanced Raman Scattering (TERS). *Physical Chemistry Chemical Physics* **2012**, *14* (27), 9636–9641.

(99) Miranda, A.; Malheiro, E.; Skiba, E.; Quaresma, P.; Carvalho, P. A.; Eaton, P.; de Castro, B.; Shelnutt, J. A.; Pereira, E. One-Pot Synthesis of Triangular Gold Nanoplates Allowing Broad and Fine Tuning of Edge Length. *Nanoscale* **2010**, *2* (10), 2209–2216.

(100) Takezaki, M.; Kida, R.; Kato, Y.; Tominaga, T. Preparations of Triangular Gold Nanoplates by Chemical and Photoreduction Methods. *Chem Lett* **2009**, *38* (11), 1022–1023.

(101) Demille, T. B.; Neal, R. D.; Preston, A. S.; Liang, Z.; Oliver, A. G.; Hughes, R. A.; Neretina, S. Epitaxially Aligned Single-Crystal Gold Nanoplates Formed in Large-Area Arrays at High Yield. *Nano Res* **2022**, *15* (1), 296–303. https://doi.org/10.1007/s12274-021-3473-1.

(102) Sun, Z.; Chen, X.; Wang, L.; Zhang, G.; Jing, B. Synthesis of Gold Nanoplates in Lamellar Liquid Crystal. *Colloids Surf A Physicochem Eng Asp* **2008**, *326* (1–2), 23–28.

(103) Pei, M. S.; Li, J.; Wang, L. Y.; Wu, Z. Y.; Wu, X. Z.; Tao, X. T. Synthesis of Gold Nanogears, Nanobelts and Nanoplates in Hexagonal Phase of Lyotropic Liquid Crystal. *Materials Research Innovations* **2010**, *14* (2), 127–132.

(104) Wang, L.; Wu, X.; Li, X.; Wang, L.; Pei, M.; Tao, X. Facile Synthesis of Concave Gold Nanoplates in Hexagonal Liquid Crystal Made of SDS/Water System. *Chemical communications* **2010**, *46* (44), 8422–8423.

(105) Wang, L. Y.; Chen, X.; Chai, Y. C.; Hao, J. C. Controlled Formation of Gold Nanoplates and Nanobelts in Lyotropic Liquid Crystal Phases with Imidazolium Cations. *Colloids Surf A Physicochem Eng Asp* **2007**, *293* (1–3), 95–100.

(106) Zhang, N.; Xu, A.; Liu, B.; Godbert, N.; Li, H. Lyotropic Liquid Crystals of Tetradecyldimethylaminoxide in Water and the in Situ Formation of Gold Nanomaterials. *ChemPhysMater* **2023**, *2* (2), 134–140.

(107) Zhou, M.; Lin, M.; Chen, L.; Wang, Y.; Guo, X.; Peng, L.; Guo, X.; Ding, W. Thickness-Dependent SERS Activities of Gold Nanosheets Controllably Synthesized via Photochemical Reduction in Lamellar Liquid Crystals. *Chemical Communications* **2015**, *51* (24), 5116–5119.

(108) Francis, S.; Nuwad, J.; Gupta, A.; Sainis, J. K.; Tewari, R.; Mitra, D.; Varshney, L. Sunlight Mediated Synthesis of PDDA Protected Concave Gold Nanoplates. *Journal of Nanoparticle Research* **2013**, *15* (3), 1482. https://doi.org/10.1007/s11051-013-1482-z.

(109) Tong, W.; Yang, S.; Ding, B. UV Irradiation Induced Formation of Single-Crystal Gold Nanonetworks with Controllable Pore Distribution. *Colloids Surf A Physicochem Eng Asp* **2009**, *340* (1), 131–134. https://doi.org/https://doi.org/10.1016/j.colsurfa.2009.03.012.

(110) Yang, S.; Zhang, T.; Zhang, L.; Wang, Q.; Zhang, R.; Ding, B. Morphological Transition of Gold Nanostructures Induced by Continuous Ultraviolet Irradiation. *Nanotechnology* **2006**, *17* (22), 5639.

(111) Lee, W.-K.; Cha, S.-H.; Kim, K.-H.; Kim, B.-W.; Lee, J.-C. Shape-Controlled Synthesis of Gold Icosahedra and Nanoplates Using Pluronic P123 Block Copolymer and Sodium Chloride. *J Solid State Chem* **2009**, *182* (12), 3243–3248.

(112) Li, X.; Zhi, L. Graphene Hybridization for Energy Storage Applications. *Chem Soc Rev* **2018**, *47* (9), 3189–3216.

(113) Chen, X.; Shehzad, K.; Gao, L.; Long, M.; Guo, H.; Qin, S.; Wang, X.; Wang, F.; Shi, Y.; Hu, W. Graphene Hybrid Structures for Integrated and Flexible Optoelectronics. *Advanced Materials* **2020**, *32* (27), 1902039.

(114) Reina, G.; González-Domínguez, J. M.; Criado, A.; Vázquez, E.; Bianco, A.; Prato, M. Promises, Facts and Challenges for Graphene in Biomedical Applications. *Chem Soc Rev* **2017**, *46* (15), 4400–4416.

(115) Novoselov, K. S.; Geim, A. K.; Morozov, S. V; Jiang, D.; Zhang, Y.; Dubonos, S. V; Grigorieva, I. V; Firsov, A. A. Electric Field Effect in Atomically Thin Carbon Films. *Science (1979)* **2004**, *306* (5696), 666–669.

(116) Kumar, N.; Salehiyan, R.; Chauke, V.; Joseph Botlhoko, O.; Setshedi, K.; Scriba, M.; Masukume, M.; Sinha Ray, S. Top-down Synthesis of Graphene: A Comprehensive Review. *FlatChem* **2021**, *27*, 100224. https://doi.org/https://doi.org/10.1016/j.flatc.2021.100224.

(117) Gutiérrez-Portocarrero, S.; Roquero, P.; Becerril-González, M.; Zúñiga-Franco, D. Study of Structural Defects on Reduced Graphite Oxide Generated by Different Reductants. *Diam Relat Mater* **2019**, *92*, 219–227. https://doi.org/https://doi.org/10.1016/j.diamond.2019.01.001.

(118) Bai, H.; Li, C.; Shi, G. Functional Composite Materials Based on Chemically Converted Graphene. *Advanced Materials* **2011**, *23* (9), 1089–1115.

(119) Bielawski, C.; Dreyer, D. R.; Park, S.; Ruoff, R. S. The Chemistry of Graphene Oxide. *Chem. Soc. Rev* **2010**, *39* (1), 233–236.

(120) Brodie, B. C. XIII. On the Atomic Weight of Graphite. *Philos Trans R Soc Lond* **1859**, No. 149, 249–259.

(121) Staudenmaier, L. Verfahren Zur Darstellung Der Graphitsäure. *Berichte der deutschen chemischen Gesellschaft* **1898**, *31* (2), 1481–1487.

(122) Hummers, W. S. Jr.; Offeman, R. E. Preparation of Graphitic Oxide. *J Am Chem Soc* **1958**, *80* (6), 1339. https://doi.org/10.1021/ja01539a017.

(123) Chen, J.; Yao, B.; Li, C.; Shi, G. An Improved Hummers Method for Eco-Friendly Synthesis of Graphene Oxide. *Carbon N Y* **2013**, *64*, 225–229. https://doi.org/https://doi.org/10.1016/j.carbon.2013.07.055.

(124) Yu, H.; Zhang, B.; Bulin, C.; Li, R.; Xing, R. High-Efficient Synthesis of Graphene Oxide Based on Improved Hummers Method. *Sci Rep* **2016**, *6* (1), 36143. https://doi.org/10.1038/srep36143.

(125) Zhang, Q.; Yang, Y.; Fan, H.; Feng, L.; Wen, G.; Qin, L.-C. Synthesis of Graphene Oxide Using Boric Acid in Hummers Method. *Colloids Surf A Physicochem Eng Asp* **2022**, *652*, 129802. https://doi.org/https://doi.org/10.1016/j.colsurfa.2022.129802.

(126) Marcano, D. C.; Kosynkin, D. V; Berlin, J. M.; Sinitskii, A.; Sun, Z.; Slesarev, A.; Alemany, L. B.; Lu, W.; Tour, J. M. Improved Synthesis of Graphene Oxide. *ACS Nano* **2010**, *4* (8), 4806–4814.

(127) Méndez-Lozano, N.; Pérez-Reynoso, F.; González-Gutiérrez, C. Eco-Friendly Approach for Graphene Oxide Synthesis by Modified Hummers Method. *Materials* **2022**, *15* (20). https://doi.org/10.3390/ma15207228.

(128) Chen, J.; Li, Y.; Huang, L.; Li, C.; Shi, G. High-Yield Preparation of Graphene Oxide from Small Graphite Flakes via an Improved Hummers Method with a Simple Purification Process. *Carbon N Y* **2015**, *81*, 826–834. https://doi.org/https://doi.org/10.1016/j.carbon.2014.10.033.

(129) Ranjan, P.; Agrawal, S.; Sinha, A.; Rao, T. R.; Balakrishnan, J.; Thakur, A. D. A Low-Cost Non-Explosive Synthesis of Graphene Oxide for Scalable Applications. *Sci Rep* **2018**, *8* (1), 12007.

(130) Benzait, Z.; Chen, P.; Trabzon, L. Enhanced Synthesis Method of Graphene Oxide. *Nanoscale Adv.* **2021**, *3* (1), 223–230. https://doi.org/10.1039/D0NA00706D.

(131) Panwar, V.; Chattree, A.; Pal, K. A New Facile Route for Synthesizing of Graphene Oxide Using Mixture of Sulfuric–Nitric–Phosphoric Acids as Intercalating Agent. *Physica E Low Dimens Syst Nanostruct* **2015**, *73*, 235–241. https://doi.org/https://doi.org/10.1016/j.physe.2015.06.006.

(132) Dimiev, A. M.; Tour, J. M. Mechanism of Graphene Oxide Formation. *ACS Nano* **2014**, *8* (3), 3060–3068.

(133) Kang, J. H.; Kim, T.; Choi, J.; Park, J.; Kim, Y. S.; Chang, M. S.; Jung, H.; Park, K. T.; Yang, S. J.; Park, C. R. Hidden Second Oxidation Step of Hummers Method. *Chemistry of Materials* **2016**, *28* (3), 756–764. https://doi.org/10.1021/acs.chemmater.5b03700.

(134) De Silva, K. K. H.; Huang, H.-H.; Joshi, R. K.; Yoshimura, M. Chemical Reduction of Graphene Oxide Using Green Reductants. *Carbon N Y* **2017**, *119*, 190–199. https://doi.org/https://doi.org/10.1016/j.carbon.2017.04.025.

(135) Agarwal, V.; Zetterlund, P. B. Strategies for Reduction of Graphene Oxide – A Comprehensive Review. *Chemical Engineering Journal* **2021**, *405*, 127018. https://doi.org/https://doi.org/10.1016/j.cej.2020.127018.

(136) Pei, S.; Cheng, H.-M. The Reduction of Graphene Oxide. *Carbon N Y* **2012**, *50* (9), 3214–3216.

(137) Zhang, P.; Li, Z.; Zhang, S.; Shao, G. Recent Advances in Effective Reduction of Graphene Oxide for Highly Improved Performance toward Electrochemical Energy Storage. *Energy & Environmental Materials* **2018**, *1* (1), 5–12.

(138) Zhou, A.; Bai, J.; Hong, W.; Bai, H. Electrochemically Reduced Graphene Oxide: Preparation, Composites, and Applications. *Carbon N Y* **2022**, *191*, 301–332. https://doi.org/https://doi.org/10.1016/j.carbon.2022.01.056.

(139) Tas, M.; Altin, Y.; Celik Bedeloglu, A. Reduction of Graphene Oxide Thin Films Using a Stepwise Thermal Annealing Assisted by L-Ascorbic Acid. *Diam Relat Mater* **2019**, *92*, 242–247. https://doi.org/https://doi.org/10.1016/j.diamond.2019.01.009.

(140) Eda, G.; Chhowalla, M. Chemically Derived Graphene Oxide: Towards Large-area Thin-film Electronics and Optoelectronics. *Advanced materials* **2010**, *22* (22), 2392–2415.

(141) Wang, X.; Shi, G. Flexible Graphene Devices Related to Energy Conversion and Storage. *Energy Environ Sci* **2015**, *8* (3), 790–823.

(142) Zhao, C.; Xing, L.; Xiang, J.; Cui, L.; Jiao, J.; Sai, H.; Li, Z.; Li, F. Formation of Uniform Reduced Graphene Oxide Films on Modified PET Substrates Using Drop-Casting Method. *Particuology* **2014**, *17*, 66–73.

(143) Sa, K.; Mahanandia, P. Conducting Reduced Graphene Oxide Film as Transparent Electrode. *Thin Solid Films* **2019**, *692*, 137594. https://doi.org/https://doi.org/10.1016/j.tsf.2019.137594.

(144) Bargaoui, I.; Bitri, N.; Ménard, J.-M. A Comparative Investigation of Chemically Reduced Graphene Oxide Thin Films Deposited via Spray Pyrolysis. *ACS Omega* **2022**, *7* (14), 11973–11979. https://doi.org/10.1021/acsomega.2c00108.

(145) Wang, X.; Zhi, L.; Müllen, K. Transparent, Conductive Graphene Electrodes for Dye-Sensitized Solar Cells. *Nano Lett* **2008**, *8* (1), 323–327. https://doi.org/10.1021/nl072838r.

(146) Eda, G.; Fanchini, G.; Chhowalla, M. Large-Area Ultrathin Films of Reduced Graphene Oxide as a Transparent and Flexible Electronic Material. *Nat Nanotechnol* **2008**, *3* (5), 270–274. https://doi.org/10.1038/nnano.2008.83.

(147) Iasha, V.; Wahyudiana, E.; Sumantri, M. S.; Marini, A.; Setiawan, B.; Rahmawati, D. Reduced Graphene Oxide-Based Transparent Conductive Films: The Preliminary Review of Reductant Materials Agent. In *IOP Conference Series: Materials Science and Engineering*; IOP Publishing, **2021**; Vol. 1098, p 062065.

(148) Becerril, H. A.; Mao, J.; Liu, Z.; Stoltenberg, R. M.; Bao, Z.; Chen, Y. Evaluation of Solution-Processed Reduced Graphene Oxide Films as Transparent Conductors. *ACS Nano* **2008**, *2* (3), 463–470. https://doi.org/10.1021/nn700375n.

(149) Lee, D. W.; Hong, T.-K.; Kang, D.; Lee, J.; Heo, M.; Kim, J. Y.; Kim, B.-S.; Shin, H. S. Highly Controllable Transparent and Conducting Thin Films Using Layer-by-Layer Assembly of Oppositely Charged Reduced Graphene Oxides. *J Mater Chem* **2011**, *21* (10), 3438–3442.

(150) He, Q.; Wu, S.; Gao, S.; Cao, X.; Yin, Z.; Li, H.; Chen, P.; Zhang, H. Transparent, Flexible, All-Reduced Graphene Oxide Thin Film Transistors. *ACS Nano* **2011**, *5* (6), 5038–5044. https://doi.org/10.1021/nn201118c.

(151) Chang, C.-W.; Hon, M.-H.; Leu, I.-C. The Transmittance and Sheet Resistance of Chemically and Heat Reduced Graphene Oxide Film. *Opt Quantum Electron* **2018**, *51* (1), 4. https://doi.org/10.1007/s11082-018-1698-3.